

**Silica Nanoparticle Reinforced Composite Elastomers
as Functional Soft Materials**

Fumio Asai

Department of Molecular and Macromolecular Chemistry
Nagoya University

2022

Contents

Chapter I

General Introduction

| | |
|--|----|
| 1-1. Introduction | 1 |
| 1-2. Elastomers | 4 |
| 1-2-1. Basics of Rubber Elasticity Theory | 4 |
| 1-2-2. Mechanical Behavior of Elastomers under Large Deformation | 8 |
| 1-2-3. Reinforced Elastomer Based on Inorganic Filler | 11 |
| 1-3. Biological Soft Tissue..... | 15 |
| 1-3-1. Extracellular Matrix..... | 15 |
| 1-3-2. Cornea..... | 17 |
| 1-4. Composite Elastomer Inspired by a Cornea | 20 |
| 1-5. Scope of This Thesis..... | 22 |
| 1-5-1. Objectives | 22 |
| 1-5-2. Outline of This Thesis..... | 23 |
| References..... | 24 |

Chapter II

Nanostructure and Mechanical Performance of a Transparent Polymethacrylate Elastomer Composite Filled with Spherical Silica Particles

| | |
|--|----|
| 2-1. Introduction | 29 |
| 2-2. Experimental Section..... | 30 |
| 2-2-1. Materials | 30 |
| 2-2-2. Analytical Techniques..... | 31 |
| 2-2-3. Cross-Sectional Observations | 31 |
| 2-2-4. Small-angle X-ray scattering. | 31 |
| 2-2-5. Mechanical Properties. | 32 |
| 2-2-6. Atomic Force Microscope Analysis..... | 32 |
| 2-2-7. Differential Scanning Calorimetry..... | 33 |
| 2-2-8. Hansen Solubility Parameter (HSP) | 33 |
| 2-2-9. Vibration Damping Loss Factor Measurement. | 34 |
| 2-2-10. Dynamic Mechanical Analysis. | 34 |

| | |
|---|----|
| 2-3. Results and Discussion | 34 |
| 2-3-1. Preparation of the Composite Elastomer..... | 34 |
| 2-3-2. Arrangement of Silica Particles in the Composite Elastomers..... | 39 |
| 2-3-3. Toughening of the Composite Elastomers. | 41 |
| 2-3-4. Nanoscale Mapping of the Composite Elastomers. | 46 |
| 2-3-5. Vibration-Damping Property of the Composite Elastomer, | 59 |
| 2-4. Conclusions | 63 |
| References..... | 64 |

Chapter III

Functional Polymethacrylate Composite Elastomer Filled with Multilayer Graphene and Silica Particles

| | |
|---|----|
| 3-1. Introduction | 68 |
| 3-2. Experimental Section..... | 70 |
| 3-2-1. Materials | 70 |
| 3-2-2. Analytical Techniques..... | 70 |
| 3-2-3. Cross-Sectional Observations | 71 |
| 3-2-4. Mechanical Properties..... | 71 |
| 3-2-5. Electrical Conductivity | 71 |
| 3-2-6. Thermal Conductivity | 72 |
| 3-2-7. Dynamic Mechanical Analysis | 72 |
| 3-2-8. Vibration Dumping Loss Factor Measurement..... | 72 |
| 3-3. Results and Discussion | 73 |
| 3-3-1. Dispersibility of MLG into MEO ₂ MA..... | 73 |
| 3-3-2. Preparation of the Composite Elastomer..... | 75 |
| 3-3-3. Mechanical Property of the Composite Elastomers. | 79 |
| 3-3-4. Electrical Properties of the Composite Elastomer | 85 |
| 3-3-5. Thermal Conductivity of the Composite Elastomer..... | 89 |
| 3-3-6. Dynamic mechanical properties of the Composite Elastomer | 91 |
| 3-4. Conclusions | 95 |
| References..... | 96 |

Chapter IV

Tough and 3D-Printable Poly(2-methoxyethyl Acrylate)-Silica Composite Elastomer with Anti-Platelet Adhesion Property

| | |
|--|-----|
| 4-1. Introduction | 100 |
| 4-2. Experimental Section..... | 102 |
| 4-2-1. Materials | 102 |
| 4-2-2. Analytical Techniques..... | 103 |
| 4-2-3. 3D printing..... | 103 |
| 4-2-4. Cross-section observations. | 104 |
| 4-2-5. Mechanical properties..... | 104 |
| 4-2-6. Human Platelet Adhesion Test. | 104 |
| 4-3. Results and Discussion | 105 |
| 4-3-1. Preparation of the Composite Elastomer | 105 |
| 4-3-2. 3D Printing of the Composite Elastomer..... | 107 |
| 4-3-3. Array of the Silica Particle in Composite Elastomers..... | 109 |
| 4-3-4. Toughening of the Composite Elastomers | 113 |
| 4-3-5. Platelet Adhesion Test with Human Blood | 119 |
| 4-4. Conclusions | 121 |
| References..... | 123 |

Chapter V

| | |
|--|------------|
| Summary and Outlook..... | 126 |
| <i>Publications</i> | <i>129</i> |
| <i>Presentations at International Conferences.....</i> | <i>130</i> |
| <i>Patents</i> | <i>130</i> |
| <i>Acknowledgements.....</i> | <i>131</i> |

Chapter I

General Introduction

1-1. Introduction

Soft materials that are flexible, such as gel or rubber, are a type of polymer material with various properties and are generally referred to elastomers, which is a portmanteau of *elastic polymers*. In our daily lives, elastomers are useful due to their physical properties and have many applications, such as in automobiles and airplanes, precise machinery, damping materials for buildings, and sports equipment. In recent years, the realization of next-generation communication technologies such as 5G and beyond will require flexible materials for wearable devices^[1,2] and small antennas^[3–5]. In addition, the realization of autonomous robots is becoming a reality. In the real world, which is formed according to human behavior, it is important for humans and robots to coexist with materials that are similar to the human body, and research on soft robots is being actively conducted.^[6–8] Elastomers are expected to be used in such cutting-edge applications.

Functional elastomers are indispensable for these important products that will support our lives in the future, and the development of new materials that composite various substances is in progress.^[9–14] Elastomers undergo significant deformation at low tension and return to their original shape when the tension is released. For elastomers to exhibit such responses, there must be sufficient molecular mobility of the polymer chains and cross-linking between the partial chains to prevent flow and provide recovery (**Figure 1-1a**).^[15] The elongation to break of a cross-linked elastomer is proportional to one-half of the molecular weight between the cross-linked points of the polymer chains

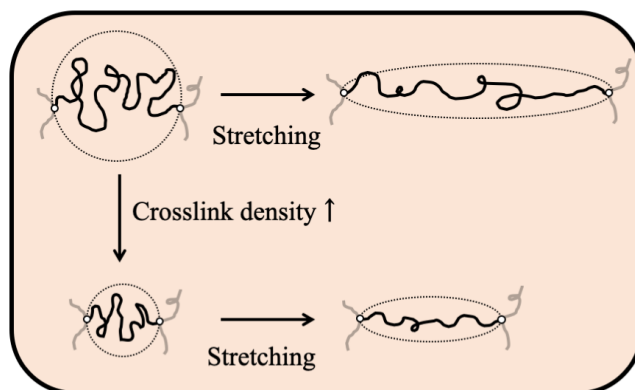
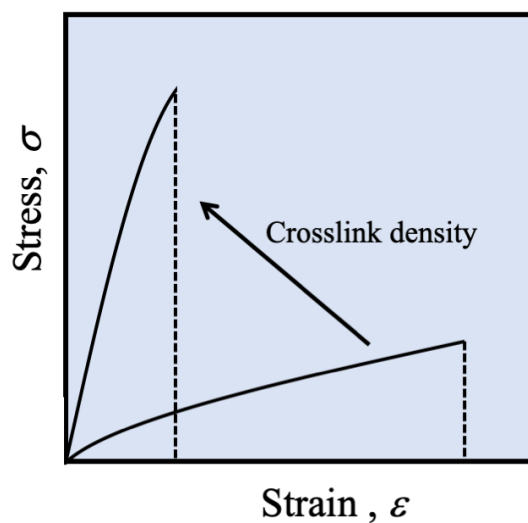
a**b**

Figure 1-1. (a) Conceptual diagram of the extension of partial chains when uniaxially extending networks with different molecular weights of partial chains with different crosslink densities. (b) Stress–strain curves of elastomers with different crosslink densities. Reproduced with permission from Ref 15.

constituting the elastomer. Therefore, the mechanical properties of the elastomer can be controlled by simply changing the cross-link density of the same material. However, if the cross-link density is increased to raise the elastic modulus, the extensibility is drastically reduced (**Figure 1-1b**). Generally, increasing the elongation and modulus of elastomers with conventional crosslinked structures is a trade-off, and it is not easy to improve the toughness of elastomers. To enrich and make human life more convenient in the future, it is necessary to develop new elastomers with mechanical properties and functionality appropriate for their applications. While the relationship between the molecular structure of existing elastomers and their mechanical properties has been clarified through years of research, it is important to incorporate new ideas and technologies to realize novel materials.

From these perspectives, this study first focused on investigating the relation between an interface layer corresponding to a bound rubber near fillers and the physical properties of a novel composite elastomer composed of an acrylic polymer and inorganic fillers. Second, functions derived from the nanostructures of the composite elastomer, which provide clues to the creation of new functional elastomers, are investigated by various methods.

In this introduction chapter, the characteristics of the mechanical properties of elastomers and the reinforcement effect of composite elastomers with fillers are discussed. Then, the extracellular matrix, which is a widely understood soft material, and a novel composite elastomer that mimics the structure of a cornea are explained. Finally, the objective and outline for this thesis are described.

1-2. Elastomers

1-2-1. Basics of Rubber Elasticity Theory

When an elastomer is stretched by an external force, it exhibits a high elongation of several times and a high recovery property, returning to its original state when the external force is released. Even when such large elongation and shrinkage are applied repeatedly, the physical properties of the elastomer do not undergo obvious degradation which is a mechanical property characteristic of elastomers called rubber elasticity. The elasticity that occurs when a metal spring is stretched comes from the energy elasticity that results from the distance between the atoms constituting the spring. On the other hand, the elongation and contraction of gels and elastomers such as rubbers composed of crosslinked polymer chains is mainly due to entropic elasticity.

Considering the stretching motion of a single polymer chain, such as polyethylene, which consists of a carbon main chain connected by covalent bonds, there are three possible deformations of the C-C bond: 1) stretching between atoms, 2) bending of the bond angle, and 3) rotation of the atoms. When considering the energy change for each deformation, 1) and 2) are those that expand the distance between atoms, causing a sharp increase in the internal energy. In contrast, since the rotational motion of the atoms in 3) does not change the distances between them, the rotation of the C-C bond, which does not vastly increase the energy, always occurs preferentially. The free energy G of the system can be expressed from the internal energy E , absolute temperature T , and entropy S by the following eq 1:

$$G = E - TS \quad (1)$$

If the rotation of the C-C bond occurs preferentially in the elongation of a single polymer chain, E does not change. Therefore, for G to change, S must change, and this change

creates elasticity.

The partial chain with Brownian motion under the glass transition temperature exists as a random coil state, similar to a coiled string, to reduce the potential energy associated with the rotation of the C-C bond. If the distance x between the two ends of the polymer chain follows a Gaussian distribution, the polymer chain with such a characteristic is called a Gaussian chain (**Figure 1-2a**). When both ends of the polymer chain in this Gaussian state are pulled, the polymer chain can be easily extended with weak force, accompanied by various conformational changes due to thermal motion. A random coil in a Gaussian state before elongation can take on various molecular conformations and has high entropy, whereas a polymer chain stretched by elongation is restricted in the conformation it can take, resulting in a decrease in entropy. This causes a recovery force due to the elongated polymer chains trying to return to their original state, which is called entropy elasticity. It is known that the tension f generated by the entropic elasticity of a single chain, based on statistical mechanics, is given by eq 2:

$$f = \frac{3k_B T}{na^2} x \quad (2)$$

where, k_B is Boltzmann's constant, T is the absolute temperature, n is the number of monomers constituting the polymer, a is the size of the monomers, and x is the elongation. In other words, entropy elasticity also follows Hooke's law. However, eq 2 is only applicable up to approximately one-third of the length of the polymer chain until it is fully stretched, but the change in tension at higher elongation cannot be explained by eq 2 because if the chain is stretched until such an affect appears, it will be outside the Gaussian distribution.

Thus, considering the stretching of a cross-linked body formed by gathering several Gaussian chains with no entanglement in the polymer chains, the relationship

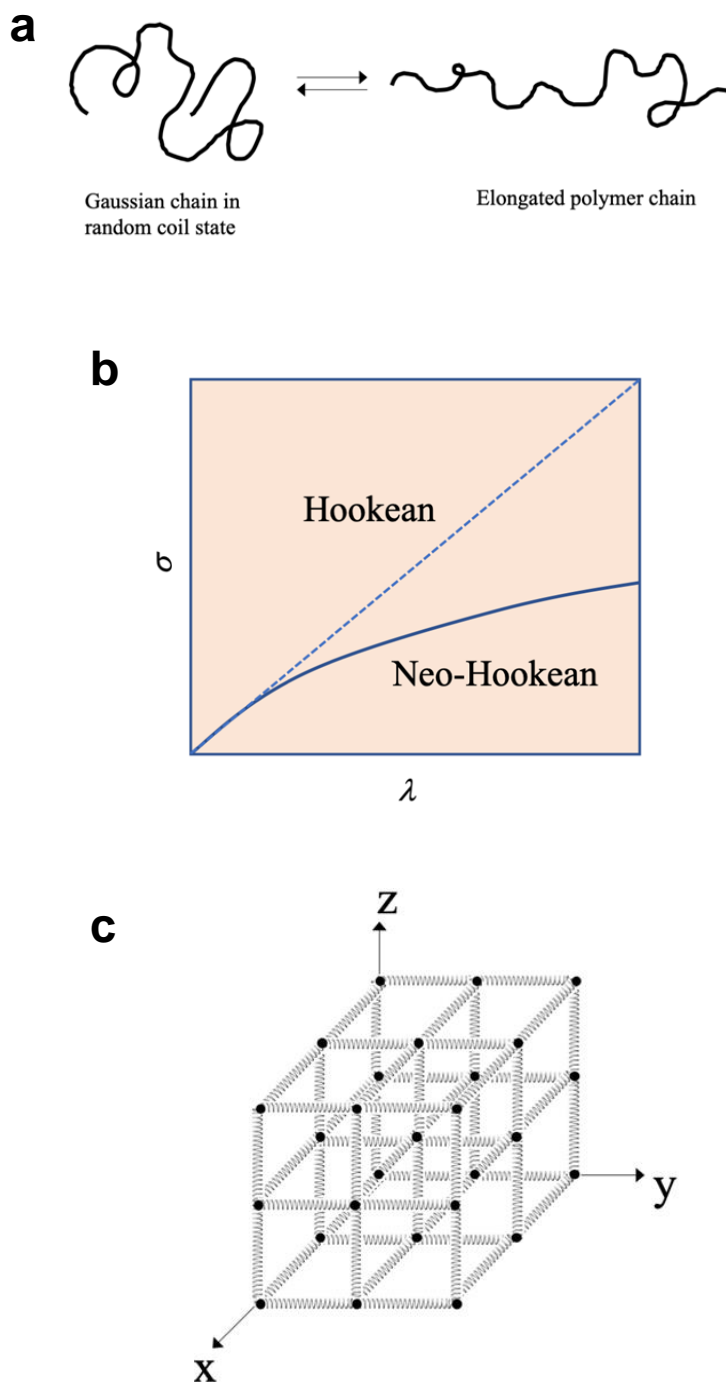


Figure 1-2. (a) Conformational changes between a Gaussian state and an extended state of an isolated polymer chain. (b) Diagram of the relationship between the stress σ and stretch ratio λ of the elastomer according to Hooke's law (dotted line) and of Neo-Hooke's law (solid line). (c) Conceptual diagram of a network structure in which polymer chains exhibiting Hookean elasticity are connected to form a polymer network in the x , y , and z directions. Reproduced with permission from Ref 15.

between its elongation ratio λ and stress σ (f per unit area A_0) of the cross-linked body is expressed in eq 3:

$$\sigma = \nu k_B T \left(\lambda - \frac{1}{\lambda^2} \right) \quad (3)$$

where, ν is the number of partial chains (N) per unit volume (V) and λ is the ratio (L/L_0) of the initial length L_0 before the cross-linked body is stretched to length L during deformation. In other words, since $\sigma = f/A_0$, f and λ for a cross-linked structure composed of multiple Gaussian chains do not have a simple proportional relationship. As a result, plotting against λ , a curve showing a convex shape is obtained (solid line in **Figure 1-2b**).^[16–18] An elastic body that exhibits this relationship is called a Neo-Hookean elastic body. When this value is 1, such as for a metal spring, the material is called a Hookean elastic body and shows changes such as those illustrated by the dotted line in **Figure 1-2b**.

If N independent polymer chains exhibiting hook elasticity ($f = kx$) in the x -axis direction are arranged in parallel, the total stress generated when stretched λ times in the x -direction will be $Nk\lambda$. Then, a network structure consisting of polymer chains connected in the y and z directions, that exhibit this spring-like Hookean elasticity, is considered (**Figure 1-2c**). When this network structure is stretched in the x direction, contraction occurs in the y - and z -axis directions, and expansion pressure is also generated to resist the internal pressure generated in this structure. The neo-Hookean elasticity exhibited by cross-linked bodies is a property resulting from the action of the expansion pressure generated by stretching, which partially cancels out the stress. This is called classical rubber elasticity theory, and is based on the assumption of affine deformation, in which the polymer chain is treated as a Gaussian chain, the volume of the structure does not change with stretching, and the local deformation is analogous to the deformation of the

whole body.^[18,19] This theory also fails to describe the mechanical behavior of elastomers at large deformations, since they deviate from the Gaussian distribution at large elongations as in the case of single polymer chains.

1-2-2. Mechanical Behavior of Elastomers under Large Deformation

The relationship between the elongation and tension of a polymer chain under large elongation is described by eq 4, which applies the Langevin function L , and is referred to as the "non-Gaussian chain theory"^[16,20]:

$$f = \left(\frac{k_B T}{a} \right) L^{-1} \left(\frac{x}{na} \right) \quad (4)$$

Expanding this equation gives the following eq 5:

$$f = \left(3k_B T \frac{x}{na^2} \right) \left[1 + \left(\frac{3}{5} \right) \left(\frac{x}{na} \right)^2 + \left(\frac{99}{175} \right) \left(\frac{x}{na} \right)^4 + \left(\frac{513}{875} \right) \left(\frac{x}{na} \right)^6 + \dots \right] \quad (5)$$

Hence, eq 1 is an approximation of eq 5 in $x/na \ll 1$. The difference between the relationship between tension and elongation expressed in eq 2 is shown in **Figure 1-3a**. The solid line obtained from eq 5 indicates the change in tension due to the polymer chain becoming fully extended as it is stretched. This solid line is consistent with the Gaussian chain approximation in the low stretch ratio region, but the relationship between elongation and tension rises significantly as the stretch ratio increases. In other words, as the approximation shows, it can be said that the Gaussian chain is the case only when the elongation is less than that of the non-Gaussian chain.

Next, we consider a cross-linked body made of N molecular chains. The relationship between the stress and the elongation ratio λ of such a cross-linked body is given by eq 6.^[21]

$$\sigma = \frac{vk_B T}{3} \sqrt{n} \left[L^{-1} \left(\frac{\lambda}{\sqrt{n}} \right) - \lambda^{-\frac{3}{2}} L^{-1} \left(\frac{1}{\sqrt{\lambda} \sqrt{n}} \right) \right] \quad (6)$$

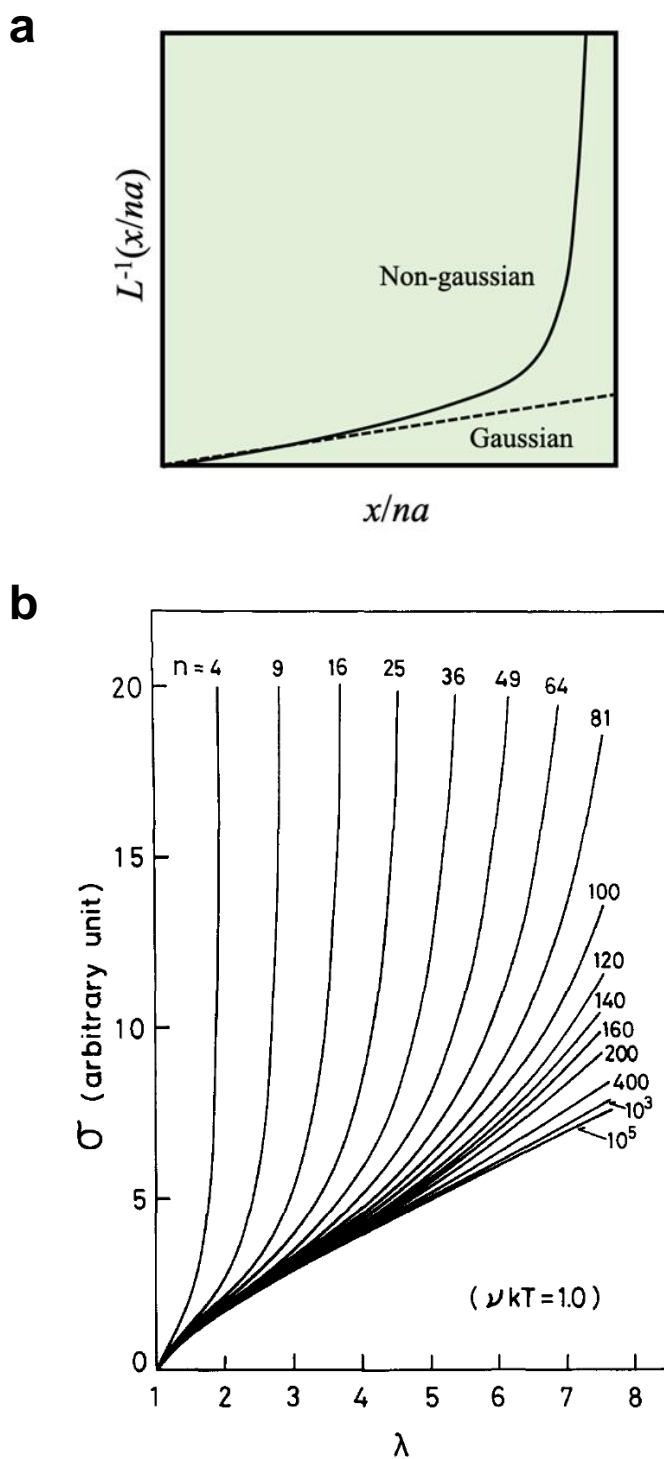


Figure 1-3. (a) Change in the conformation of a single polymer chain according to Gaussian chain theory (dotted line) and change by the non-Gaussian chain theory. (b) The stress-extension ratio curves theoretically predicted with equation (6) as a function of n . Reproduced with permission from Refs 15 and 21.

According to eq 6, σ is plotted against λ with the number of segments in partial chain n as a variable in **Figure 1-3b**. The smaller the n value is that makes up the polymer chain, the more quickly these curves rise. This phenomenon occurs because the smaller n (the shorter the segment length between the cross-linked points) is, the earlier the extending effect of the molecular chain appears. The reason why this value rises and increases rapidly is because the bond angle between segments must be widened to further deform the fully stretched molecular chain. In other words, under large deformation, the mechanism of elastic force shifts from entropy elasticity to energy elasticity. However, in many cases, the actual system does not show such a change in the stress–strain relationship that causes the polymer chain to be in a fully extended state. One of the reasons for this phenomenon is that the distribution of the length of the polymer chains between the cross-linked points in the actual network structure is large; thus, the stress is concentrated on the shortest chains when they are largely stretched.

As explained here, the stress–strain relationship of elastomers is mainly influenced by the molecular weight at the cross-linking point, and there is a trade-off between their elasticity and extensibility. To obtain an elastomer with sufficient toughness, increasing the number of cross-linked points to increase the elastic modulus impairs the extensibility, while decreasing the number of cross-linked points to improve the extensibility decreases the elastic modulus. This limitation of mechanical properties in the design of elastomers is a major stumbling block to the practical use of the material, but there are significant reasons for the wide use of elastomers in a variety of applications. The reason for this is that the mechanical properties of the elastomer can be greatly improved by filling with inorganic filler.

1-2-3. Reinforced Elastomer Based on Inorganic Filler

Today, elastomers play a leading role as rubber-based soft materials, and are especially essential as tire materials for cars, trucks, and aircraft. The discovery of vulcanization of rubber by C. Goodyear in 1839 and the reinforcement of rubber by filling with carbon black (CB) by S. C. Mote in 1904 led to the subsequent development of reinforcing rubber for tires and the widespread use of automobiles. The reinforcing effect of CBs in rubber significantly improves the strength, durability, and wear resistance required for many soft materials, as well as other functional and related properties.^[22,23] Not only CBs, but also nanoparticles such as silica particles have been found to reinforce rubber and improve its functionality, and many results have been reported.^[24]

Numerous ideas have been proposed for the reinforcing effect of fillers on rubber, and it is widely accepted that particle size and aggregates have a significant effect on mechanical properties. Currently, there is much discussion about the reinforcing effect of rubber, mainly focusing on the interaction between the filler and rubber matrix and between fillers. There are two main interactions: 1) the formation of bound rubber at the interface of nanofillers in the rubber matrix and 2) the formation of nanofiller aggregates and the interaction of the network structure of agglomerates.^[25–31] The concept of bound rubber is said to have been first proposed by Fielding,^[32] and later became widely recognized by Kraus.^[33] Thereafter, Fujimoto et al. proposed a heterogeneous model of bound rubber in CB-filled rubber in 1964, and many studies on bound rubber have been carried out, but the basic model is still considered to be useful (**Figure 1-4a**).^[34,35] In the heterogeneous model shown in **Figure 1-4a**, A is the rubber matrix under micro-Brownian motion, B is the hard rubber region formed by the nonuniform distribution of cross-linking points, and C is the bound rubber or immobile rubber layer formed on the surface

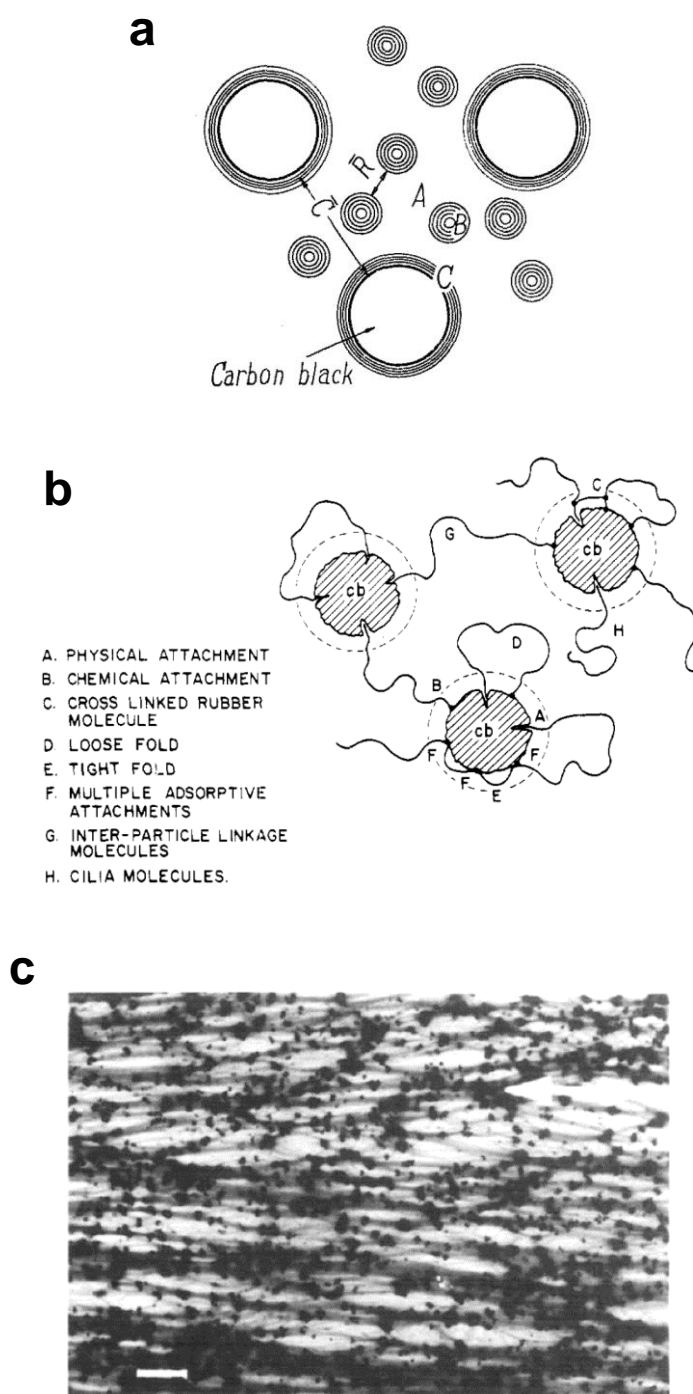


Figure 1-4. (a) Conceptual diagram of a heterogeneous model of vulcanized rubber containing carbon black. (b) Diagram of the model for the filled rubber system. (c) TEM photograph of the network structure in a stretched CB-filled rubber. Reproduced with permission from Refs 34, 36 and 37.

of CB particles. O'Brien et al. used NMR to analyze the interaction between CB and cis-polybutadiene and proposed a model of polymer chains attached to the filler surface between the bound rubber and the CB (**Figure 1-4b**).^[36] Reichert et al. revealed the presence of bands connecting CB particles and aggregates by transmission electron microscopy (TEM) observation of CB-filled rubber under elongation (**Figure 1-4c**).^[37]

Filler networks in rubber reinforcement have also been discussed from various perspectives as the origin of properties such as the Mullins effect and the Payne effect, which are phenomena characteristic of filler-filled elastomers.^[23,38–41] In recent years, the interaction between filler and rubber has been clarified from various aspects by analysis of the network structure formed by nanoparticles using 3D-TEM^[42], mechanical evaluation of the nanointerface near the filler using atomic force microscopy (AFM)^[43,44] and molecular dynamics simulations^[45–54] (**Figure 1-5**).

Thus, although many researchers have been trying to understand the reinforcement mechanism of filler-filled rubbers, the role of the bound rubber derived from the complex morphology of polymer and nanoparticles is still not understood precisely. The presence of filler aggregate structures and several additives (e.g., dispersants, plasticizers and vulcanizers) in rubber materials complicates the various analyses of these structures. To address these difficulties, it is effective for understanding the phenomena to use simpler systems with relatively few components for analysis. Fukahori et al. proposed a modified Guth-Gold equation that considers the effect of filler networks on mechanical properties in filler-filled rubber based on experiments using rubber samples with anisotropically fixed rod-shaped fillers.^[55]

Based on the theory that has been proposed thus far, elucidation of the role of the bound layer by a simple experimental system is effective in understanding the essence

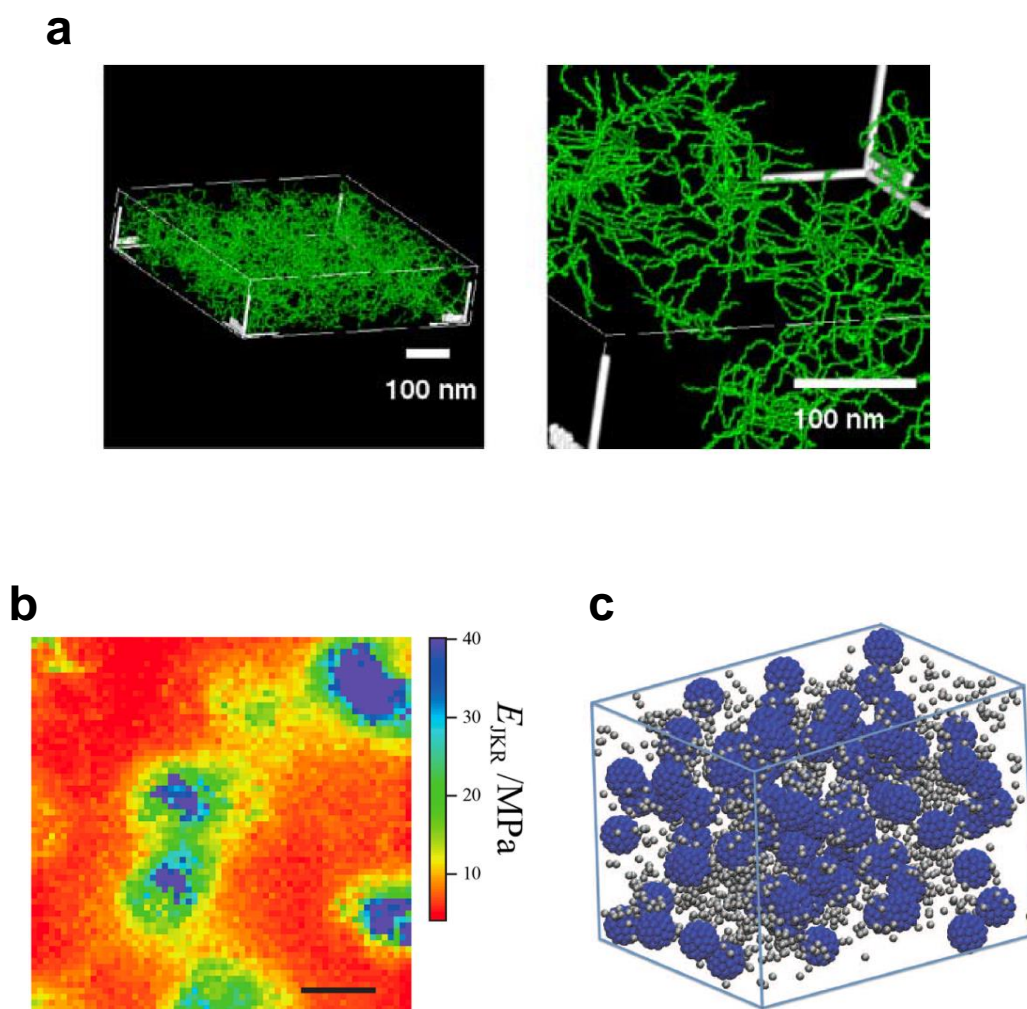


Figure 1-5. (a) Visualization of the network structures of carbon black in natural rubber matrix by skeletonizing the 3D-TEM images. (b) Young's modulus mapping image of a silica-filled styrene–butadiene rubber by AFM. (c) Computational study of the polymer entanglement network by molecular dynamics simulations. Reproduced with permission from Refs 42, 44 and 46.

of the phenomenon, but the reports of such studies are limited due to the complexity of the components of the filler-filled rubber.

1-3. Biological Soft Tissue

1-3-1. Extracellular Matrix

Biological tissues are composed of cells and noncells, and the constituent substance that fills the spaces between the cells is called the extracellular matrix (ECM). The most abundant component of the ECM, excluding water, is collagen fibers, and the next most abundant component is elastin, which is the main component of elastic fibers. These fibrils exist in a gel-like substrate composed of carbohydrates and water, including other glycoproteins and proteoglycans. In other words, the ECM is the most familiar composite soft material reinforced by stiff components such as collagen fibrils.

The mechanical properties of biological tissues formed by the ECM cover a wide range, with Young's modulus E_0 ranging from 10 Pa for adipose tissue to 10^7 Pa for tendons and skin (**Figure 1-6a**).^[13,56] This wide range of variation in mechanical properties is similar to the variation in artificial materials ranging from rubber to carbon materials, and affects properties such as elongation, strength, toughness, and hardness. **Figure 1-6b** shows three different stress–strain curves typically observed in thermoplastics, synthetic rubbers and gels, and biological tissue networks. Thermoplastics exhibit a high modulus of elasticity of approximately 1 GPa at small deformations, and then yield at nearly constant stress. Synthetic rubbers and gels exhibit an elastic response with a relatively low modulus that changes weakly with deformation. Biological networks exhibit nonlinear elasticity with a low Young's modulus ($E_0 = 10^2 \sim 10^6$ Pa) at low strain, which is very soft, but rapidly becomes stiff with deformation.^[57]

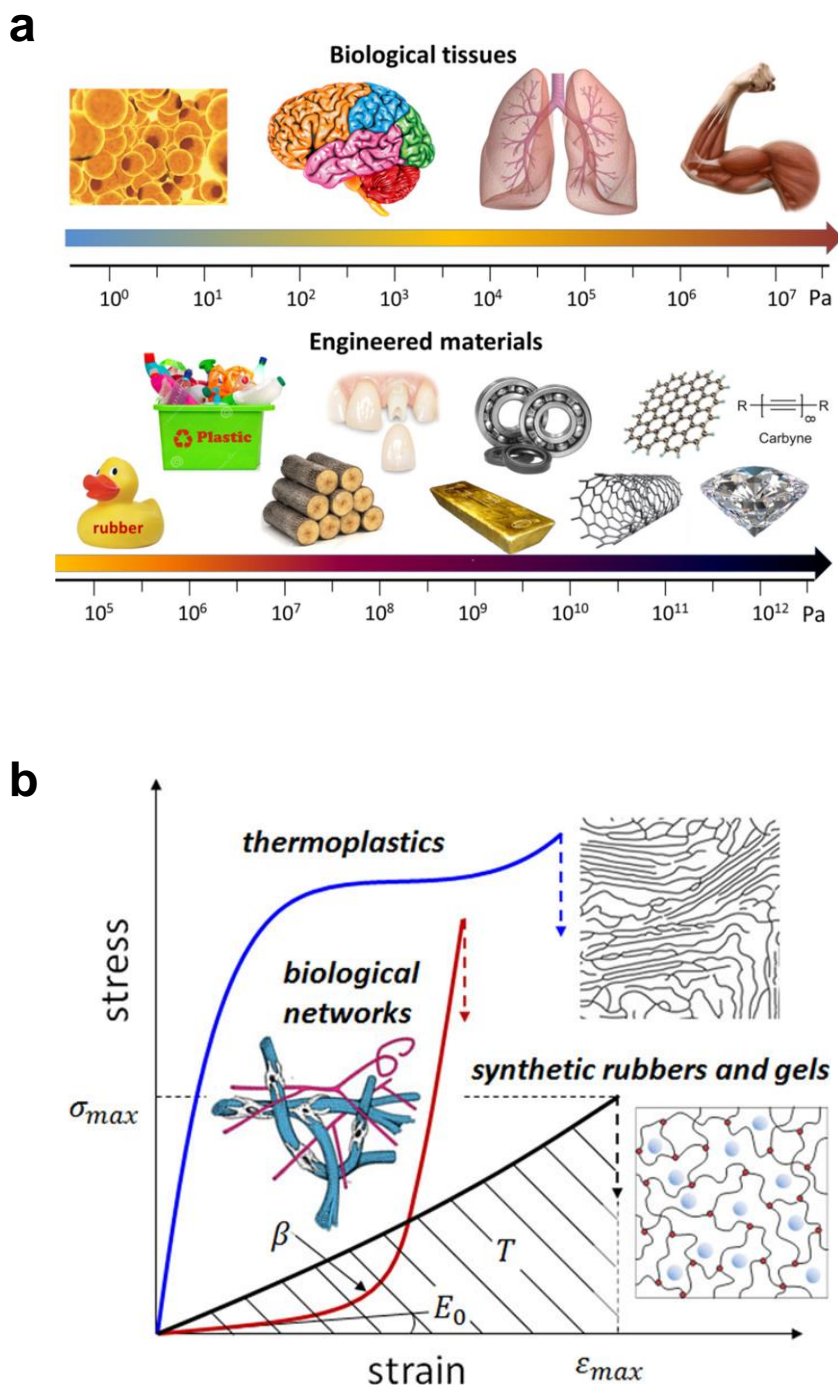


Figure 1-6. (a) Elastic moduli of currently available materials and soft biological tissues. (b) Conceptual diagram representing the stress–strain curves of three different materials. Reproduced with permission from Ref 13.

It is not easy to replicate such a J-shaped curve due to nonlinear elasticity in artificial soft materials such as elastomers and gels, and it is one of nature's defense mechanisms to prevent accidental organ rupture.

The structural changes in these tissues, such as the collagen fiber content ratio, its diameter, and fibril array, have a significant influence on mechanical properties such as stiffness and elasticity. The complex structure formed by the ECM provides not only good mechanical properties but also a variety of functions to biological tissues.

1-3-2. Cornea

Among ECMs, the cornea of the eye is a characteristic biological soft tissue with transparency and toughness (**Figure 1-7a**).^[58] The cornea consists of a gel-like matrix of mucopolysaccharides and water combined with collagen fibrils, and has excellent transmission of wavelengths in the visible light region (**Figure 1-7b**).^[59] This transparency of the cornea is due to the construction of an ordered structure of uniformly aligned collagen fibers with nanosized diameters (**Figure 1-8a and b**).^[60,61] Each collagen fibril is connected by proteoglycans with glycosaminoglycan (GAG) chains, which exert an attracting force on each fibril (**Figure 1-8c**).^[62] On the other hand, in the matrix between collagen fibrils, repulsive forces are generated between the fibers due to the osmotic pressure derived from the ion concentration (Donnan effect) (**Figure 1-8d**). The antagonism of these two forces forms a nano-order array structure.

When light is incident on an ordered structure such as a colloidal crystal composed of materials with different refractive indices such as collagen fibers and substrate, the light scattered and diffracted inside the structure will be interfered with and show an enhanced structural color. The wavelength of light emphasized by the

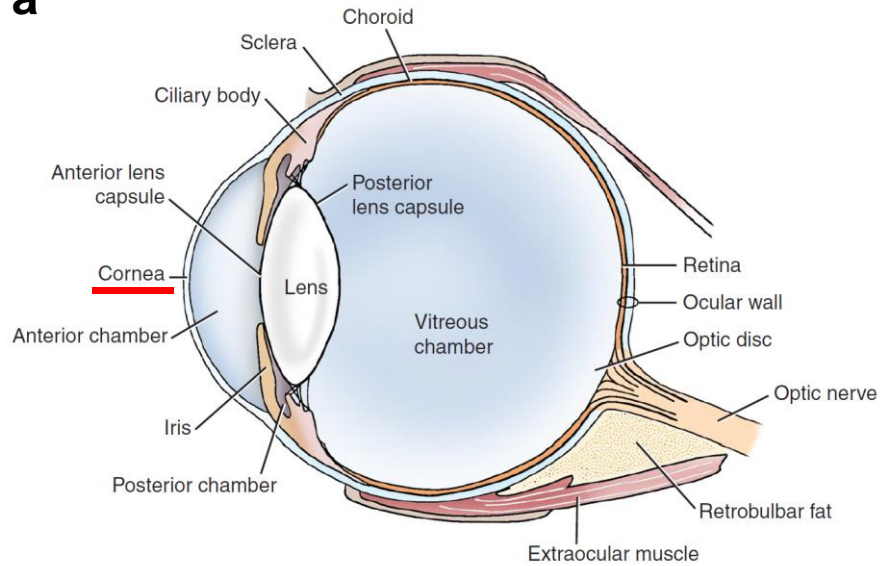
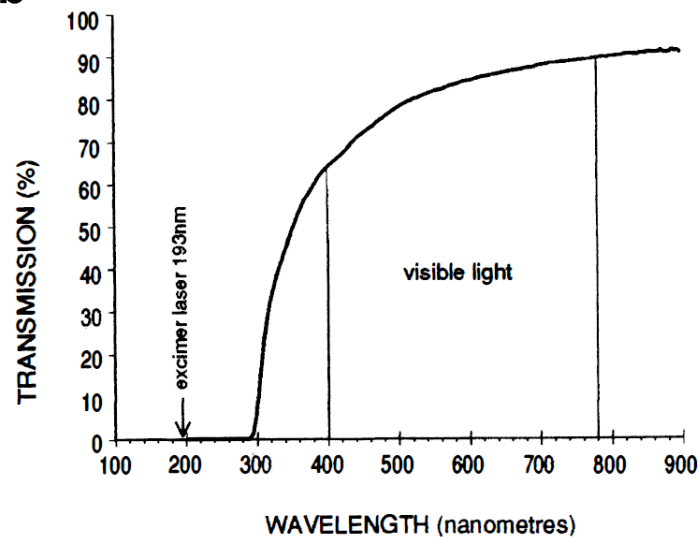
a**b**

Figure 1-7. (a) Anatomy of the eye. (b) Transmission spectrum across a human cornea as measured by spectrophotometry. Reproduced with permission from Refs 58 and 59.

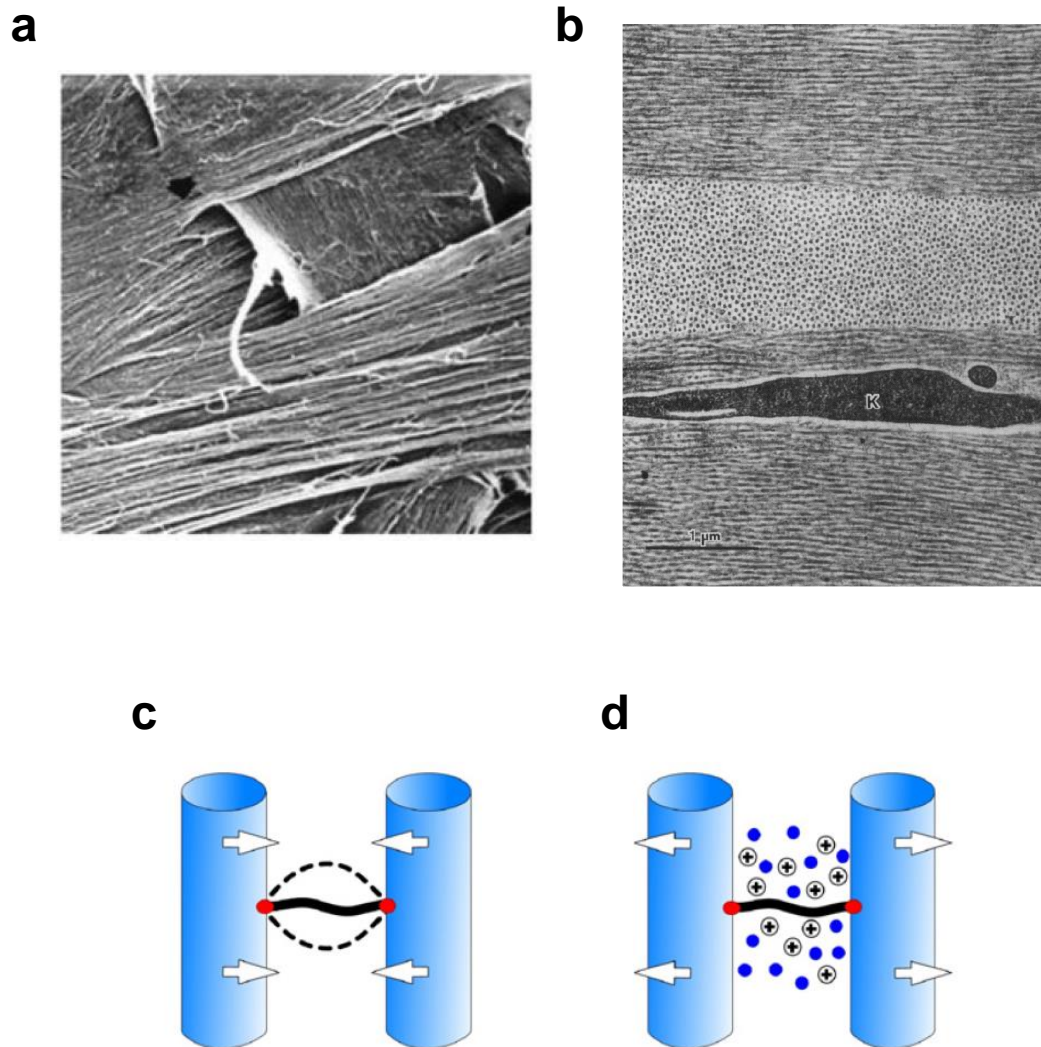


Figure 1-8. (a) Collagen fibrils in the cornea have a region where a lamella splits into two separate lamellae. (b) Cross sectional image of collagen fibrils in the cornea. Collagen fibrils have a uniform diameter and are arranged in the same direction within the lamellae. (c) Attractive forces between collagen fibrils arise from GAG chain vibrations. (d) Repulsive forces between collagen fibrils are due to the Donnan effect. Reproduced with permission from Refs 60, 61 and 62.

interference follows the Bragg-Snell equation as given below^[63]:

$$\lambda = 2d \sqrt{n_{eff}^2 - \sin^2 \theta} \quad (7)$$

where λ is the wavelength of the maximum reflected intensity, d is the interplanar spacing between order structures, n_{eff} is the effective refractive index, and θ is the incident angle with respect to normal incidence. Here, n_{eff} is associated with filling factor by the following equation:

$$n_{eff}^2 = n_1^2 \phi + n_2^2 (1 - \phi) \quad (8)$$

where n_1 and n_2 are the refractive index for substances forming ordered structures and their matrix, respectively. As seen from eq 7, the wavelength of the light to be emphasized is affected by the angle of incidence and the interplanar spacing.

Both the diameter and the interspacing of the collagen fibrils in the cornea are much smaller than the wavelengths in the visible light region, and the wavelengths of light emphasized by interference exist in the ultraviolet region. Therefore, the cornea achieves colorless transparency in the visible light region due to its finely controlled structure. Such a highly functional biological tissue structure will be an important milestone for the creation of novel soft materials.

1-4. Composite Elastomer Inspired by a Cornea

Recently, Watanabe et al. demonstrated composite elastomers consisting of spherical silica particles and poly[di(ethylene glycol)methyl ether methacrylate] (PMEO₂MA) that mimic the structure and function of a cornea, with the aim of creating new functional soft materials.^[64] The silica particles form a colloidal crystal-like ordered structure in this elastomer, similar to collagen fibers in the cornea, and a colorless and transparent composite elastomer is obtained when filled with 34 vol% spherical silica

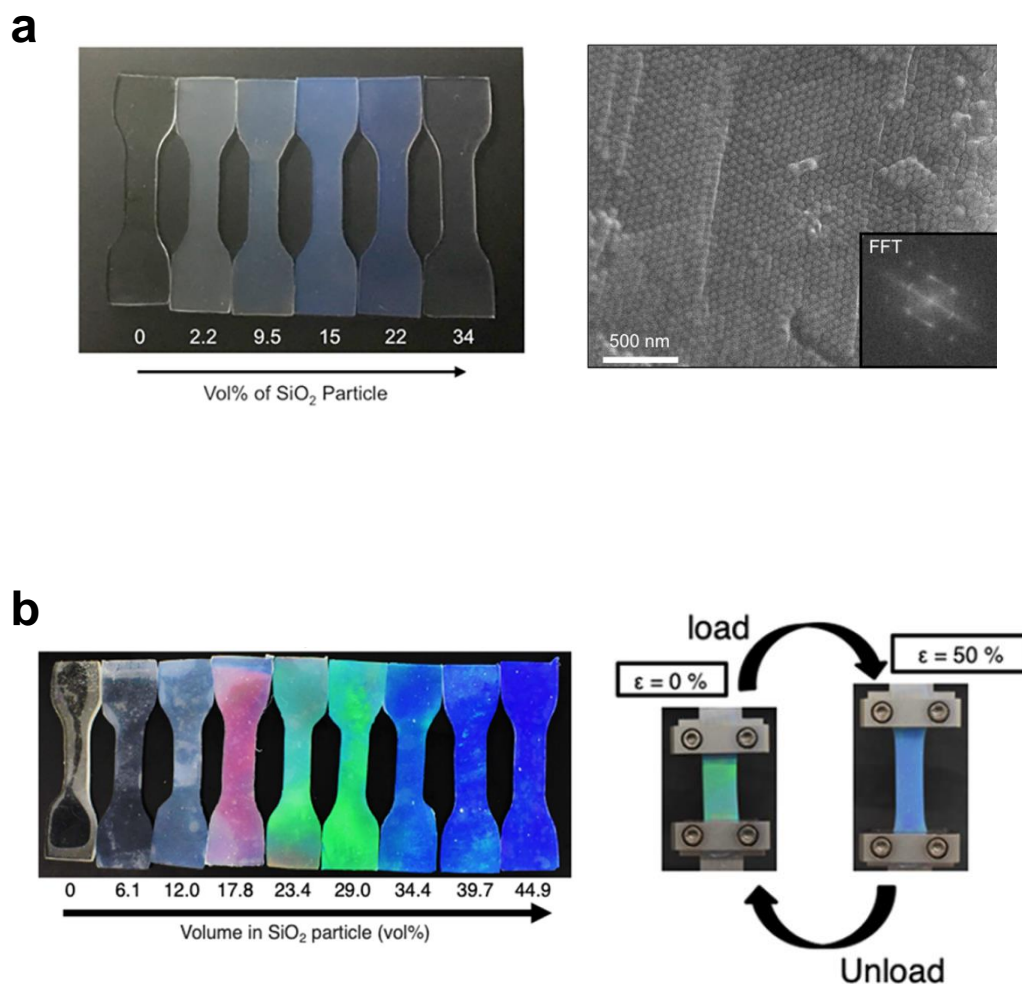


Figure 1-9. (a) Photograph of composite elastomers inspired by cornea with different amounts of 110 nm silica particles and the SEM image of the composite elastomer with 34 vol% SiO₂. (b) Structurally colored composite elastomers containing 180 nm silica particles and their stimuli responsiveness for deformation. Reproduced with permission from Refs 64 and 65.

particles 110 nm in diameter (**Figure 1-9a**). Using spherical silica particles with a 180 nm diameter, composite elastomers that exhibit red, green, and blue structural colors can be obtained depending on the amount of silica particles. These composite elastomers exhibit stimuli-responsive properties that change their coloration with elongation (**Figure 1-9b**).^[65]

Another feature of these silica composite elastomers is that increasing the amount of silica particles improves both the stress at break and strain at break in uniaxial tensile tests, increasing the toughness of the material. In typical filler-filled rubbers, as the amount of filler is increased, the strain at break decreased with an increase in Young's modulus and stress at break. This means that these become hard and brittle.^[25] Therefore, the relationship between the increase in fillers and the improvement in toughness in these composite elastomers might be different from that of conventional filler-filled rubbers, and understanding the relation between the existence of the interface layer and the reinforcement phenomenon has been an important issue. In addition, previous studies have focused on the mechanical properties and structural color of these composite elastomers, but other functions have not been clarified, so proposing several practical applications has been a subject.

1-5. Scope of This Thesis

1-5-1. Objectives

If the relation between the existence of the interface layer and the reinforcement phenomenon of silica composite elastomers, which are inspired by the structure of biological soft tissues, can be clarified from their characteristic morphology and mechanical properties, a new perspective regarding the reinforcement of elastomers with

fillers may be obtained and may be one of the cornerstones for the synthesis of novel soft materials.

While typical reinforced rubbers have multiple additives that make various analyses complex and difficult, this composite elastomer is a simple material consisting of only two components: spherical silica particles and acrylate polymer. Understanding the relationship between the mechanical properties and the structure obtained from this very simple component should reveal the role of the bound layer in filler-filled elastomers. In addition, clarifying the potential functions of this silica composite elastomer due to its unique structure will lead to the creation of new materials that will enrich our lives. In this theme, the relationship between the mechanical properties and the nanostructure of the silica particle-polymer interface in the composite elastomer is first evaluated. Then, these composite elastomers with characteristic morphology were investigated from various viewpoints to reveal their functions and to propose new composite elastomers for practical use.

1-5-2. Outline of This Thesis

This thesis consists of five chapters, Chapter I to V.

In Chapter II, the nanostructure of the silica-polymer interface in the composite elastomer is evaluated, and the relationship between the characteristic morphology and physical properties is revealed. Nanoscale mapping of the elastic modulus using AFM and thermal analysis shows that the high modulus interfacial layer near the silica particles is effective in improving the toughness of the composite elastomer. As a function of the characteristic morphology of the silica particles in the composite elastomer, the vibration damping property is evaluated. This analysis shows the possibility of the composite

elastomer for practical use as a new transparent damping material.

In Chapter III, composite elastomers filled with multilayer graphene as the second filler are fabricated, and their structure and function are evaluated. The silica particles improve the dispersibility of the multilayer graphene in the acrylic monomer solution, thus more multilayer graphene can be embedded in the composite elastomer, which improves its thermal conductivity. In this composite elastomer, the dielectric constant increases with the increase in multilayer graphene, but the increase in dielectric loss tangent is suppressed. Such a material with a high dielectric constant and low dielectric loss tangent can be expected to be an antenna substrate that enables miniaturization of these materials.

In Chapter IV, poly(2-methoxyethyl acrylate) (PMEA) which is a hydrophobic biocompatible polymer is used as a matrix material and a PMEA-silica composite elastomer is fabricated. PMEA is a viscous liquid polymer, but PMEA filled with silica particles becomes a tough composite elastomer. The anti-platelet adhesion property of the PMEA-silica composite elastomer is comparable to that of a neat PMEA, indicating that a self-supporting blood-compatible material can be obtained. Furthermore, the silica-PMEA composite elastomer can be made into complex shapes by a stereolithography (SLA) 3D printing and has the potential to be applied as a material for new medical devices.

Finally, this thesis is summarized and provides the outlook in Chapter V.

References

- [1] M. Ha, S. Lim, H. Ko, *J. Mater. Chem. B* **2018**, 6, 4043.
- [2] J. Park, J. Kim, K. Kim, S. Y. Kim, W. H. Cheong, K. Park, J. H. Song, G.

- Namgoong, J. J. Kim, J. Heo, F. Bien, J. U. Park, *Nanoscale* **2016**, 8, 10591.
- [3] Y. Goliya, A. Rivadeneyra, J. F. Salmeron, A. Albrecht, J. Mock, M. Haider, J. Russer, B. Cruz, P. Eschlwech, E. Biebl, M. Becherer, M. R. Bobinger, *Adv. Opt. Mater.* **2019**, 7, 1900995.
- [4] A. History, *ESTEEM Acad. J.* **2020**, 16, 75.
- [5] W. Li, E. Yarali, A. Bakytbekov, T. D. Anthopoulos, A. Shamim, *Nanotechnology* **2020**, 31, 9.
- [6] G. M. Whitesides, *Angew. Chemie Int. Ed.* **2018**, 57, 4258.
- [7] D. Rus, M. T. Tolley, *Nature* **2015**, 521, 467.
- [8] D. Zhalmuratova, H.-J. Chung, *ACS Appl. Polym. Mater.* **2020**, 2, 1073.
- [9] H. Gotoh, C. Liu, A. Bin Imran, M. Hara, T. Seki, K. Mayumi, K. Ito, Y. Takeoka, *Sci. Adv.* **2018**, 4, eaat7629.
- [10] S. Bauer, S. Bauer-Gogonea, I. Graz, M. Kaltenbrunner, C. Keplinger, R. Schwödiauer, *Adv. Mater.* **2014**, 26, 149.
- [11] M. L. Hammock, A. Chortos, B. C. K. Tee, J. B. H. Tok, Z. Bao, *Adv. Mater.* **2013**, 25, 5997.
- [12] T. Kajita, A. Noro, Y. Matsushita, *Polymer (Guildf)*. **2017**, 128, 297.
- [13] S. S. Sheiko, A. V. Dobrynin, *Macromolecules* **2019**, 52, 7531.
- [14] Z. Wang, C. Xiang, X. Yao, P. Le Floch, J. Mendez, Z. Suo, *Proc. Natl. Acad. Sci. U. S. A.* **2019**, 116, 5967.
- [15] Y. Takeoka, S. Liu, F. Asai, *Sci. Technol. Adv. Mater.* **2020**, 14686996.2020.1849931.
- [16] L. R. G. Treloar, *The Physics of Rubber Elasticity (Third Edition)*, **1975**.
- [17] A. N. Gent, *Sci. Technol. Rubber* **2013**, 1.

- [18] *Philos. Trans. R. Soc. London. Ser. A, Math. Phys. Sci.* **1948**, 241, 379.
- [19] P. J. Flory, *Polym. J.* **1985**, 17, 1.
- [20] v W. Kuhn, F. Grun, *Kolloid-Zeitschrift* **1942**, 101, 248.
- [21] Y. Fukahori, W. Seki, *Polymer (Guildf)*. **1992**, 33, 1058.
- [22] E. Guth, *J. Appl. Phys.* **1945**, 16, 20.
- [23] J.-B. Donnet, E. Custodero, in *Sci. Technol. Rubber*, Elsevier, **2013**, pp. 383–416.
- [24] S. K. Kumar, B. C. Benicewicz, R. A. Vaia, K. I. Winey, *Macromolecules* **2017**, 50, 714.
- [25] Y. Fukahori, *J. Appl. Polym. Sci.* **2005**, 95, 60.
- [26] S. Y. Kim, K. S. Schweizer, C. F. Zukoski, *Phys. Rev. Lett.* **2011**, 107, 225504.
- [27] R. Lach, G.-M. Kim, G. H. Michler, W. Grellmann, K. Albrecht, *Macromol. Mater. Eng.* **2006**, 291, 263.
- [28] J. Moll, S. K. Kumar, *Macromolecules* **2012**, 45, 1131.
- [29] P. Vondráček, M. Schätz, *J. Appl. Polym. Sci.* **1977**, 21, 3211.
- [30] S. Cheng, V. Bocharova, A. Belianinov, S. Xiong, A. Kisliuk, S. Somnath, A. P. Holt, O. S. Ovchinnikova, S. Jesse, H. Martin, T. Etampawala, M. Dadmun, A. P. Sokolov, *Nano Lett.* **2016**, 16, 3630.
- [31] S. Cheng, B. Carroll, V. Bocharova, J.-M. Carrillo, B. G. Sumpter, A. P. Sokolov, *J. Chem. Phys.* **2017**, 146, 203201.
- [32] J. H. Fielding, *Ind. Eng. Chem.* **1937**, 29, 880.
- [33] G. Kraus, *Fortschritte der Hochpolym.* **1971**, 155.
- [34] K. Fujimoto, *Nippon GOMU KYOKAISHI* **1964**, 37, 602.
- [35] FUJIWARA S, FUJIMOTO K, *Rubber Chem. Technol.* **1971**, 44, 1273.
- [36] J. O'Brien, E. Cashell, G. E. Wardell, V. J. McBrierty, *Macromolecules* **1976**, 9,

653.

- [37] W. F. Reichert, D. Göritz, E. J. Duschl, *Polymer (Guildf)*. **1993**, *34*, 1216.
- [38] A. N. Gent, *J. Appl. Polym. Sci.* **1974**, *18*, 1397.
- [39] R. Dargazany, V. N. Khiêm, M. Itskov, *Int. J. Plast.* **2014**, *63*, 94.
- [40] V. N. Khiêm, M. Itskov, *Int. J. Plast.* **2017**, *90*, 96.
- [41] S. Araby, Q. Meng, L. Zhang, H. Kang, P. Majewski, Y. Tang, J. Ma, *Polymer (Guildf)*. **2014**, *55*, 201.
- [42] S. Kohjiya, A. Katoh, T. Suda, J. Shimanuki, Y. Ikeda, *Polymer (Guildf)*. **2006**, *47*, 3298.
- [43] K. Nakajima, M. Ito, H. K. Nguyen, X. Liang, *Rubber Chem. Technol.* **2017**, *90*, 272.
- [44] E. Ueda, X. Liang, M. Ito, K. Nakajima, *Macromolecules* **2019**, *52*, 311.
- [45] M. A. Sharaf, J. E. Mark, *Polymer (Guildf)*. **2004**, *45*, 3943.
- [46] R. A. Riggleman, G. N. Toepperwein, G. J. Papakonstantopoulos, J. J. de Pablo, *Macromolecules* **2009**, *42*, 3632.
- [47] R. A. Riggleman, G. Toepperwein, G. J. Papakonstantopoulos, J.-L. Barrat, J. J. de Pablo, *J. Chem. Phys.* **2009**, *130*, 244903.
- [48] G. J. Schneider, K. Nusser, L. Willner, P. Falus, D. Richter, *Macromolecules* **2011**, *44*, 5857.
- [49] Y. Li, M. Kröger, W. K. Liu, *Phys. Rev. Lett.* **2012**, *109*, 118001.
- [50] E. Masnada, S. Merabia, M. Couty, J.-L. Barrat, *Soft Matter* **2013**, *9*, 10532.
- [51] A. A. Gavrilov, A. V. Chertovich, P. G. Khalatur, A. R. Khokhlov, *Macromolecules* **2014**, *47*, 5400.
- [52] A. Karatrantos, N. Clarke, R. J. Composto, K. I. Winey, *Soft Matter* **2016**, *12*,

2567.

- [53] S. K. Kumar, V. Ganesan, R. A. Riggleman, *J. Chem. Phys.* **2017**, *147*, 020901.
- [54] H. Liang, Z. Wang, A. V. Dobrynin, *Macromolecules* **2019**, *52*, 8617.
- [55] Y. Fukahori, A. A. Hon, V. Jha, J. J. C. Busfield, *Rubber Chem. Technol.* **2013**, *86*, 218.
- [56] M. Vatankhah-Varnosfaderani, A. N. Keith, Y. Cong, H. Liang, M. Rosenthal, M. Sztucki, C. Clair, S. Magonov, D. A. Ivanov, A. V. Dobrynin, S. S. Sheiko, *Science (80-.)*. **2018**, *359*, 1509.
- [57] C. Storm, J. J. Pastore, F. C. MacKintosh, T. C. Lubensky, P. A. Janmey, *Nature* **2005**, *435*, 191.
- [58] A. Clode, J. S. Mattoon, in *Small Anim. Diagnostic Ultrasound*, Elsevier, **2021**, pp. 138–164.
- [59] T. J. Freegard, *Eye* **1997**, *11*, 465.
- [60] K. M. Meek, C. Knupp, *Prog. Retin. Eye Res.* **2015**, *49*, 1.
- [61] T. U. Yoshiko Komai, *Invest. Ophthalmol. Vis. Sci.* **1991**, *32*, 2244.
- [62] P. N. Lewis, C. Pinali, R. D. Young, K. M. Meek, A. J. Quantock, C. Knupp, *Structure* **2010**, *18*, 239.
- [63] I. V. Nemtsev, I. A. Tambasov, A. A. Ivanenko, V. Y. Zyryanov, *Photonics Nanostructures - Fundam. Appl.* **2018**, *28*, 37.
- [64] K. Watanabe, E. Miwa, F. Asai, T. Seki, K. Urayama, T. Nakatani, S. Fujinami, T. Hoshino, M. Takata, C. Liu, K. Mayumi, K. Ito, Y. Takeoka, *ACS Mater. Lett.* **2020**, *2*, 325.
- [65] E. Miwa, K. Watanabe, F. Asai, T. Seki, K. Urayama, J. Odent, J.-M. Raquez, Y. Takeoka, *ACS Appl. Polym. Mater.* **2020**, *2*, 4078.

Chapter II

Nanostructure and Mechanical Performance of a Transparent Polymethacrylate Elastomer Composite Filled with Spherical Silica Particles

2-1. Introduction

In a society where various products are becoming more sophisticated and diversified, new functional elastomers that combine various substances to achieve the required performance metrics are constantly being developed.^[1–6] In the development of artificial materials that enrich our lives, mimicking the structure of biological tissues with various functions represents a new solution.

The composite elastomer, inspired by a cornea, composed of only weakly cross-linked poly(di(ethylene glycol)methyl ether methacrylate) (PMEO₂MA) and 110 nm spherical silica particles indicated a remarkable reinforcing effect of filler addition, and its fracture energy in the uniaxial tensile test increased significantly with increasing silica particle content.^[7]

The significant toughening of MEO₂MA by silica particles is thought to be due to the strong interaction between silica and polymer interface. The interaction at these interfaces might act as pseudo-cross-linking points, and understanding the relationship between the nanostructure of these interfaces and the mechanical of the composite elastomer will lead to a new understanding of the mechanism of the reinforcement phenomenon that have not been revealed in studies of filler-filled rubbers with a complex material composition

In this chapter, the dispersion state of silica particles by observing the cross

section of the composite elastomer consisting of PMEO₂MA and 110 nm spherical silica particles containing no organic cross-linking agent and analysis of the mechanical properties by a uniaxial tensile test is first reported. Subsequently, the existence of a bound layer near the particles was confirmed by nanostructure analysis using atomic force microscopy (AFM), and the relationship with bulk mechanical properties is verified. These cross-sectional observations and AFM analysis revealed that silica particles surrounded by a bound layer are fixed in the composite elastomer at intervals on the order of nm with almost no aggregation. The simple morphology of the composite elastomer consisting of PMEO₂MA and spherical silica particles, with almost no filler aggregates, could help to better clarify the role of the bound layer on the reinforcement effect.

It is predicted that deformation of the composite elastomer with its characteristic nanostructure would induce shear strain between the silica particles, effectively dissipating thermal energy due to friction. Since energy dissipation due to local friction in a polymer material plays an important role in vibration damping, the damping loss factor of an unconstrained composite beam of the composite elastomer is evaluated.

2-2. Experimental Section

2-2-1. Materials

Di(ethylene glycol)methyl ether methacrylate (MEO₂MA) (95%, 1.02 g cm⁻³, 188.22 g mol⁻¹, Sigma-Aldrich) was used as a monomer without purification. The initiator *N,N*-azobis(isobutyronitrile) (AIBN) (Kanto Kagaku, density 1.1 g cm⁻³, 164.21 g mol⁻¹) was used without purification. A monodispersed fine silica powder with a particle size of 110 nm (2.221 g cm⁻³, Silibol110, Fuji Chemical) was used as the filler to prepare the composite elastomers.

2-2-2. Analytical Techniques

The surface charge density of the silica particles dispersed in MEO₂MA was measured by using a Dispersion Technology DT-1202. The suspensions were subjected to sonication using an ultrasonic homogenizer (Hierascher, UP200 St) to completely disperse the silica particles before measurement. Thermogravimetric analysis (TGA) was performed using a Shimadzu DTG-60 with an aluminum pan under nitrogen gas conditions. A TGA sample with a mass of 10–15 mg was placed in the pan, and an aluminum lid was placed on the pan. An empty pan with a lid was used as the reference. The temperature of the sample was increased to 500 °C from 20 °C (20 °C min⁻¹) and then held for 1 h. Density measurements were performed with a Micromeritics Instrument Corp. AccuPyc 1330 pycnometer (helium gas, 25 °C).

2-2-3. Cross-Sectional Observations

Scanning electron microscopy (SEM) images were obtained with a Hitachi High-Technologies FE-SEM SU8020. To prepare cross-section samples for SEM observation, the composite elastomers underwent ion polishing treatment using a Gatan Model 693 Precision Ion Polishing System (−160 °C, 4 keV, 6 h), and the cross-section samples were sputter-coated with platinum. Transmission electron microscopy (TEM) images were captured on a JEOL JEM-1230 TEM instrument.

2-2-4. Small-angle X-ray scattering.

Small-angle X-ray scattering (SAXS) measurements were performed on beamline BL05XU at SPring-8 (Hyogo, Japan). The undulator light source and Si(111)

monochromator were adjusted to 7 keV X-ray energy, and harmonic X-rays were removed with Rh-coated mirrors. A photon-counting two-dimensional detector (PILATUS 1 M, DECTRIS Ltd.) was placed at a distance of 4,4 m from the sample. The beam size at the sample was approximately $200\text{ }\mu\text{m} \times 100\text{ }\mu\text{m}$ (horizontal \times vertical).

2-2-5. Mechanical Properties.

Uniaxial tensile tests were carried out using a Shimadzu EZ-Test (50 mm min^{-1}). The ISO37-4 dumbbell-type test pieces used for the test were prepared by punching a 1 mm thick composite elastomer sheet using a Super Dumbbell Cutter (SDMP-1000-D, DUMBELL).

2-2-6. Atomic Force Microscope Analysis.

The samples were ultramicrotomed using a Leica EM FC6 (Leica Microsystems GmbH Wetzlar, Germany) at $-120\text{ }^{\circ}\text{C}$ to obtain a smooth surface for AFM investigation. The AFM measurements were carried out using a Nanoscope V MultiMode 8 system (Bruker AXS, USA) and cantilevers having a nominal spring constant of 0.58 N/m (OMCL-TR800PSA, Olympus, Japan). The actual spring constant was measured by the thermal tune method. The measurements were operated in QNM[®] mode, in which force-distance curves were collected over selected surface areas at a resolution of 256×256 pixels. The obtained force curves were analyzed using JKR contact mechanics.^[8] According to this model, the Young's modulus E and adhesive energy w are expressed by the following two equations:

$$E = \frac{3(1 - \nu^2)}{4} \frac{1.27P}{\sqrt{R(\delta_0 - \delta_1)^3}} \quad (1)$$

$$w = -\frac{2P}{3\pi R} \quad (2)$$

where ν is the Poisson's ratio, R is the radius of curvature of the probe tip, δ is the sample deformation, and P is the maximum adhesive force.

2-2-7. Differential Scanning Calorimetry

The samples were dried at 150 °C for 15 h under vacuum. The differential scanning calorimetry (DSC) measurements were performed on a DSC 8500 (Perkin Elmer) with a standard aluminum pan under nitrogen gas conditions. A DSC sample from 15–30 mg was placed on the pan and sealed. An air pan was used as the reference. Step-scan (temperature-modulated) DSC study was carried out to obtain precise specific heat capacity (C_p) curves. Step-scan procedure involved heating steps of 3 °C at a heating rate 6 °C/min, and isothermal steps of 1 min. Then, C_p (reversing signal) and non-reversing signals were obtained using the Pyris software of Parkin-Elmer. The T_g and the heat capacity increment at the glass transition (ΔC_p) were determined from C_p curves.

2-2-8. Hansen Solubility Parameter (HSP)

To obtain the HSP of silica particles, the Hansen sphere was calculated using HSPiP software (ver. 5.3.02, developed by Dr. Hansen, Dr. Abbott and Dr. Yamamoto). Silica particles (10 mg) were added to 4 mL of the HSP-known solvents listed in Table S2, and the suspensions were sonicated at 1000 J cm⁻³ using an ultrasonic homogenizer (UP200St, Hielscher Ultrasonics). The particle size distribution of the silica particles in the suspensions was measured by a dynamic light scattering measuring device (Malvern, Zetasizer nano ZS), and solvents with a polydispersity index (PDI) ≤ 0.07 were classified as good and the others as poor.

2-2-9. Vibration Damping Loss Factor Measurement.

The loss factor of the unconstrained composite beam with the composite elastomer was measured according to the central excitation method of JIS K7391 (−20, −10, 0, 10, 20, 30, and 40 °C, ~6.4 kHz) and analyzed by using Brüel & Kjær PULS LabShop. The unconstrained composite beam specimens were prepared by bonding the SPCC steel beam ($250 \times 10 \times 1$ mm) and the elastomer sheets (1 mm thick) using adhesive.

2-2-10. Dynamic Mechanical Analysis.

Dynamic mechanical analysis (DMA) was conducted on an RSA-G2 solid analyzer (TA instruments) in the rectangular tension geometry. Rectangular samples of 1 mm \times 5 mm cross section and approximately 35 mm length were tested at 0.5% strain. Frequency sweep tests (0.01-100 Hz) were conducted from −20 to 60 °C. The master curve was created by shifting the result of frequency sweep tests obtained from different temperatures based on the time–temperature superposition principle.

2-3. Results and Discussion

2-3-1. Preparation of the Composite Elastomer.

In this study, monomer suspensions were prepared by adding 9~54 vol% spherical silica powder with an average particle size of 110 nm to MEO₂MA, which is in a liquid state at room temperature. After dispersing the silica particles in suspension using an ultrasonic homogenizer (1500 J cm^{-3}), the surface charge density of the silica particles in MEO₂MA was measured (**Figure 2-1**).^[9] The surface charge density showed a negative

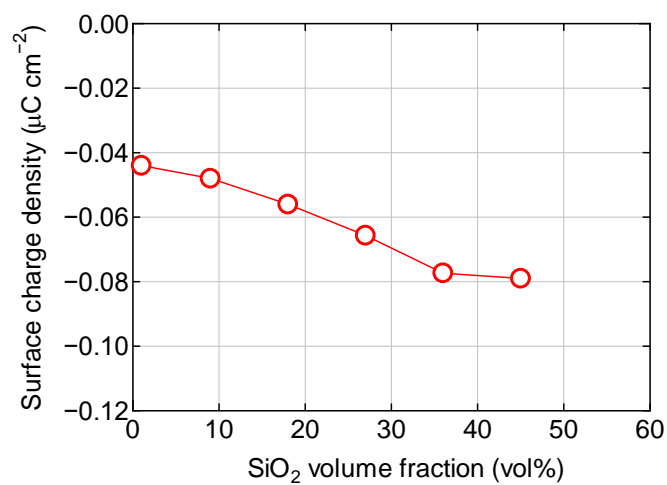


Figure 2-1. Surface charge density of silica particles in MEO₂MA.

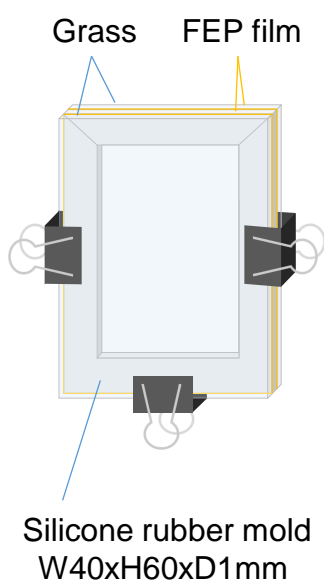
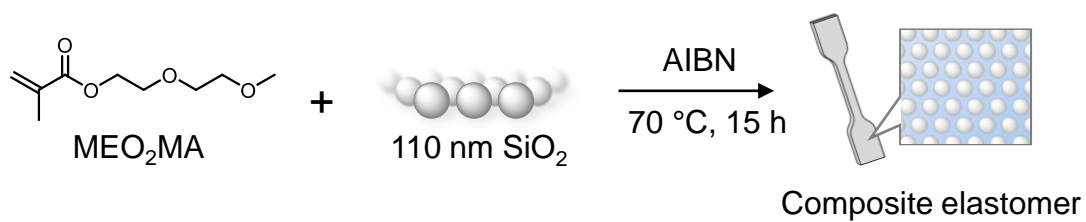


Figure 2-2. Schematic illustration of the mold.



Scheme 2-1. Conceptual Schematic Representing the Fabrication of the Composite Elastomer

value at all concentrations, and it was considered that the silica particles were dispersed in MEO₂MA due to the electrostatic repulsive force even at a high concentration. This result suggests that the hydrogen atoms of the silanol groups on the silica surface in MEO₂MA were dissociated and the particle surface was charged. Then, AIBN (0.15 mol%) was added to the suspensions, which were then poured into a mold (**Figure 2-2**) and polymerized at 70 °C for 15 hours to obtain PMEO₂MA-silica composite elastomers (**Scheme 2-1**). These elastomers were named S0, S10, S20, S30, S40, S50, and S60 on basis of the silica particle content. **Table 2-1** shows the TGA and density measurement results of the composite elastomers. In the TGA measurements, the onset temperature of weight loss for the unfilled elastomer and each silica composite elastomer was approximately 250 °C, and no effect of silica filling on pyrolysis was observed (**Figure 2-3**). The volume fraction (ϕ) of silica particles in the composite elastomer was calculated by eq. 3.

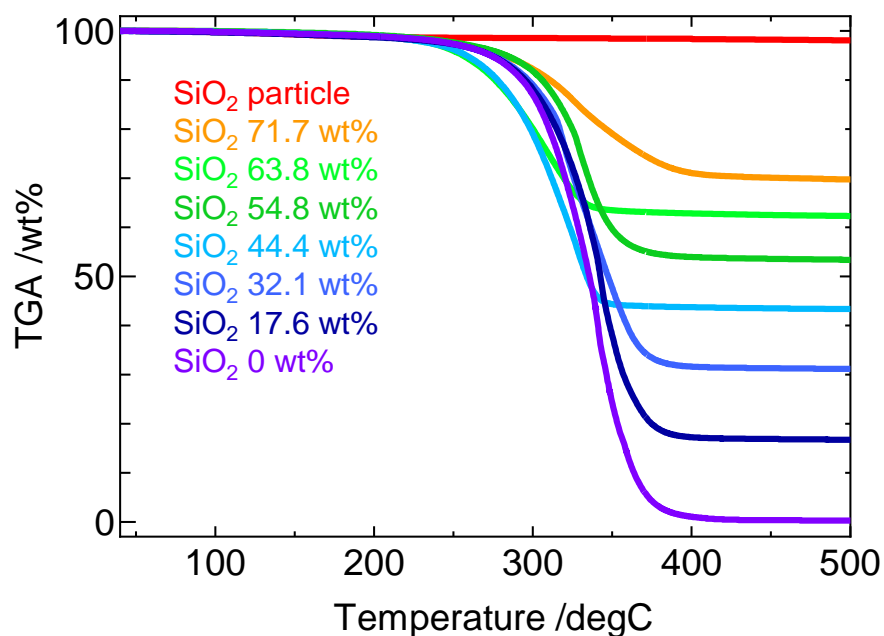
$$\phi = \frac{(TG - 0.4) \times ED}{97.7 \times 2.221} \times 100 \quad (3)$$

The residue of the composite elastomer (TG), the residue of PMEO₂MA (0.4 wt%), the residue of the silica particles (97.7 wt%), the density of the silica particles (2.221 g cm⁻³) and the density of the composite elastomers (ED) were used. The volume shrinkage of PMEO₂MA and the matrix polymer in the composite elastomer determined from these results was approximately 14%. The obtained composite elastomers showed structural colors due to scattering of wavelengths in the visible light region at up to 29.6 vol% silica particles, while samples with higher silica concentrations exhibited high transparency (**Figure 2-4a**). The visible light transmittance of S40, S50 and S60 was more than 80%, and their specular reflection spectra showed reflection peaks in the ultraviolet region (**Figure 2-5**). These results indicate that the composite elastomer became colorless and

Table 2-1. Summary of the silica volume fraction of the composite elastomers.

| Composite Elastomer | $\phi^{(a)}$ [vol%] / [wt%] | TG ^(b) [wt%] | ED ^(c) g/cm ³ | $\phi^{(d)}$ vol% |
|---------------------|--------------------------------|----------------------------|--|----------------------|
| S0 | 0.0 / 0.0 | 0.0 | 1.184 | 0.0 |
| S10 | 9.0 / 17.6 | 16.9 | 1.288 | 9.8 |
| S20 | 18.0 / 32.1 | 31.6 | 1.386 | 19.7 |
| S30 | 27.0 / 44.4 | 44.3 | 1.485 | 29.6 |
| S40 | 36.0 / 54.8 | 54.2 | 1.580 | 38.6 |
| S50 | 45.0 / 63.8 | 63.8 | 1.686 | 48.6 |
| S60 | 54.0 / 71.7 | 71.0 | 1.772 | 58.4 |

^{a)}SiO₂ fraction in the monomer suspension; ^{b)}TGA residue; ^{c)}Density of the composite elastomer; ^{d)}SiO₂ fraction in the composite elastomer

**Figure 2-3.** TGA chart of silica particles and each composite elastomer.

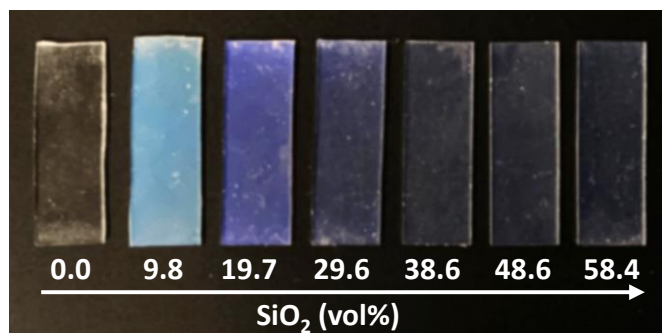


Figure 2-4. Photograph of composite elastomers containing 0, 9.8, 19.7, 29.6, 38.6, 48.6, and 58.4vol% silica particles.

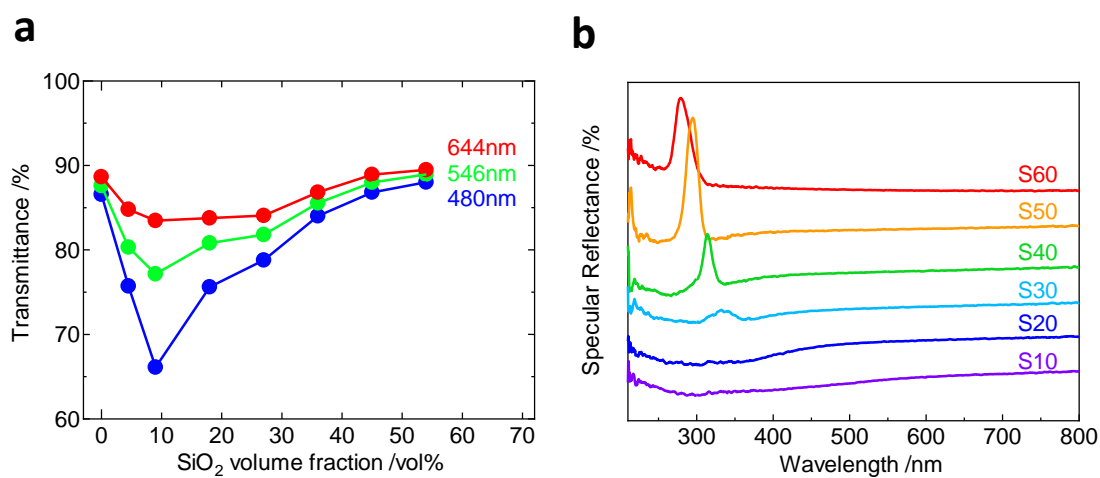


Figure 2-5. Optical properties of the elastomers consisting of the MEO2MA polymer and various amounts of monodispersed silica particles with an average particle size of 110 nm. (a) Transmission spectra of the composite elastomers. (b) Specular reflectance spectra of the composite elastomers.

transparent because the scattering wavelength of structural color shifted from visible light to the ultraviolet region due to the increase in the amount of silica particles.^[7]

2-3-2. Arrangement of Silica Particles in the Composite Elastomers.

To confirm the arrangement of the silica particles fixed in the composite elastomer, cross sections of each composite elastomer were prepared by ion polishing and observed by SEM. In S10, S20, and S30, a halo pattern can be seen in the fast Fourier transform (FFT) of the SEM image; hence, the silica particles were in an isotropic arrangement with short-range order (**Figure 2-6a, b and c**). In the cross sections of S40, S50, and S60, in which the silica particles are aligned in an orderly fashion, multiple peaks can be observed in the FFT images. This result indicated that the silica particles were embedded as colloidal crystals (**Figure 2-6d, e and f**). Pussey and Van Megen observed a colloidal suspension using polymethylmethacrylate (PMMA) particles (305 nm) with long-chain fatty acids modified on the surface and found that crystallization of particles by local freezing started from an effective volume fraction of 49.4 vol% of hard spheres and the crystal state became thermodynamically stable above 54.5 vol%.^[10] Furthermore, it has been shown that crystallization becomes difficult above 57 vol% due to the suppression of particle diffusion, and a metastable amorphous phase is formed. Kegel and van Blaaderen, by direct observation of the Brownian motion of colloidal suspensions containing PMMA-silica core-shell particles (450 nm), showed that particle diffusion did not proceed above 57 vol%, and the presence of a crystalline array was confirmed from the pair correlation function at 60 vol%.^[11] Previously, it was reported that in a composite elastomer of poly(2-methoxyethyl acrylate) (PMEA) with a chemical structure similar to PMEO₂MA and silica particles, the arrangement of particles changes

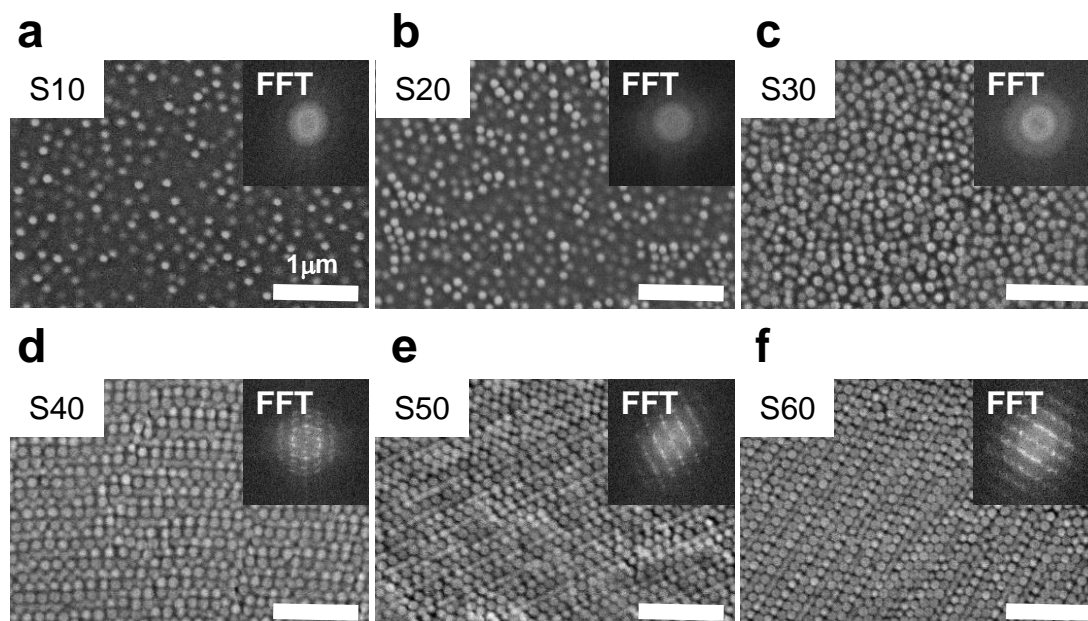


Figure 2-6. (a-f) Cross-sectional SEM images of the composite elastomers with different amounts of silica particles. The insets show a FFT image of the SEM image.

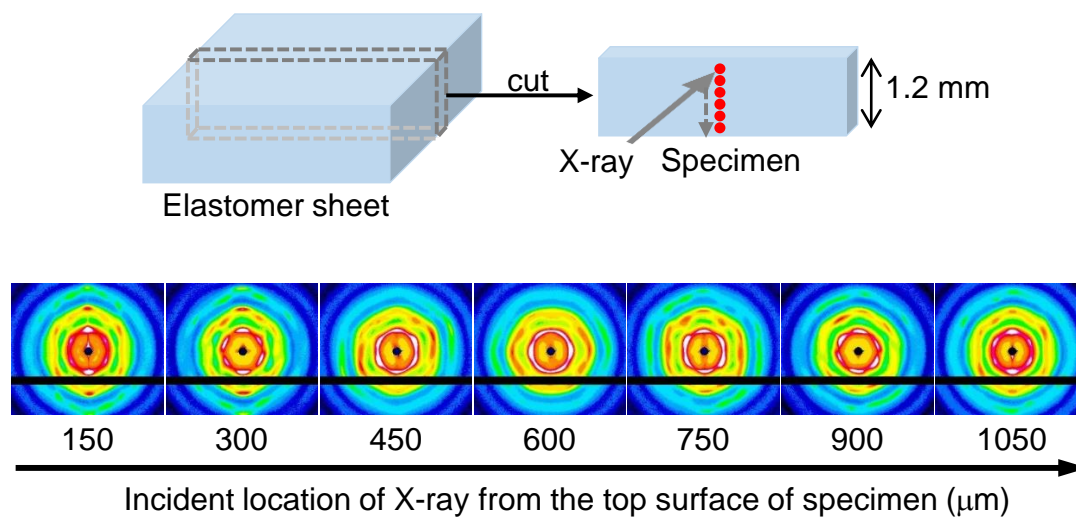


Figure 2-7. Schematic of the SAXS measurement procedure and 2D SAXS profile of the composite elastomer S40.

from short-range order to colloidal crystals, and a colloidal amorphous structure as the filling amount increases.^[12] It should be noted that, in contrast to previous results, the particles of PMEO₂MA-silica composite elastomers with more than 38.6 vol% silica particles formed a crystalline arrangement. Although the contributing factor is not clear, the surface charge density suggested that there was sufficient electrostatic repulsion between particles even at high filler amounts and that the transition to a crystalline arrangement due to particle diffusion proceeded.

SAXS measurements were then conducted from the surface of the S40 sheet to the opposite side to confirm the crystalline arrangement of the particles at various locations in the composite elastomer (**Figure 2-7**). Peaks showing the hexagonal structure of the particle array can be observed at all positions, which indicates that the colloidal crystalline arrangement was fixed throughout the bulk.^[13] The orderly array of particles was also confirmed in SEM images at different observation positions (**Figure 2-8**). These results suggest that the formation of the crystalline array of silica particles is due to spontaneous particle diffusion, not epitaxial growth induced by interaction with the surface of the mold.

2-3-3. Toughening of the Composite Elastomers.

A uniaxial tensile test was conducted to verify the reinforcing effect of the composite elastomer. In the uniaxial tensile testing of composite elastomers, the dispersion state of the particles has a significant effect on the mechanical properties, and differences in the dispersion state will lead to variations in mechanical property values. Therefore, composite elastomers were prepared by changing the sonication processing energy, and their mechanical properties were compared. From this test, it was confirmed

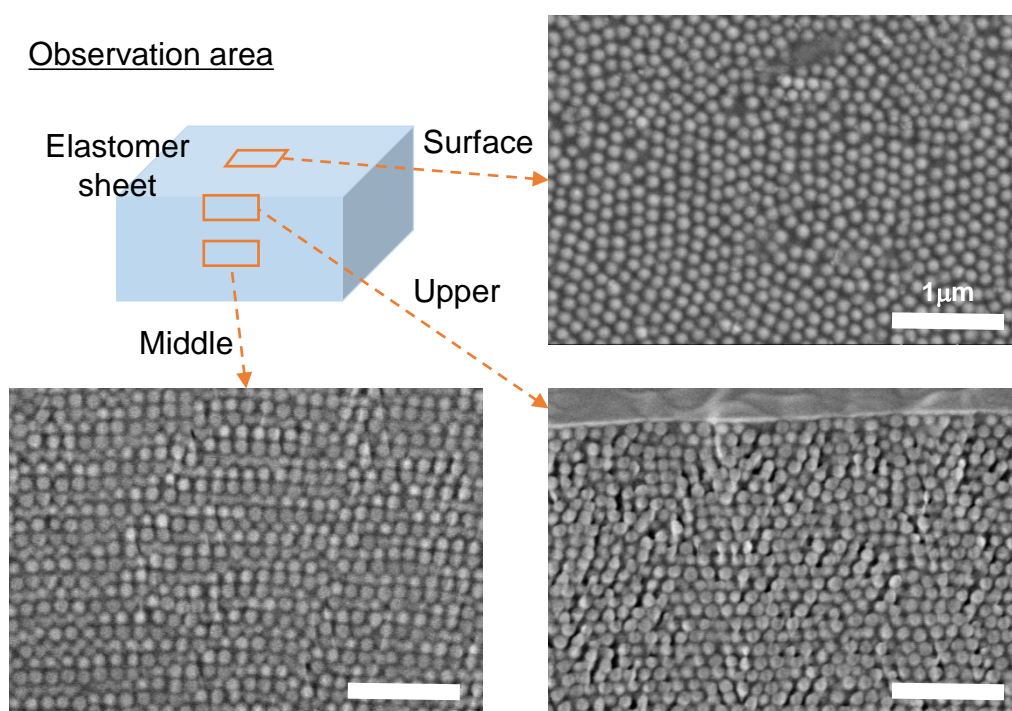


Figure 2-8. SEM images of the surface and cross section of S40

that the mechanical properties of the composite elastomers, to which a processing energy above 1500 J cm^{-3} was applied, were constant (**Figure 2-9**). In S10, S20, S30, and S40, both the stress and the strain at break increased as the amount of silica particles increased. This result indicated that the silica particles toughened the specimens (**Figure 2-10** and **Table 2-2**). On the other hand, the stress and the strain at break tended to decrease in S50 and S60. The Young's modulus of elastomers with different amounts of filler can be quantitatively expressed by the Guth-Gold relation^[14] based on Einstein's viscosity equation. Assuming that the Young's modulus of filler-filled elastomer is E , the Young's modulus of unfilled elastomer is E_0 , and the volume fraction of filler is ϕ , the Guth-Gold relation is expressed by eq. 4.

$$E = (1 + 2.5\phi + 14.1\phi^2)E_0 \quad (4)$$

The Young's modulus of the composite elastomers increased with silica particle filling, and these plots correlated very well with the Guth-Gold relation up to 48.6 vol% (**Figure 2-11**). Einstein's viscosity equation assumes monodisperse particle behavior in a dispersion, and the correlation between the Young's modulus and the Guth-Gold relation suggests that silica particles were dispersed in the elastomer without aggregation. On the other hand, the Young's modulus at 58.4 vol% is much higher than the Guth-Gold relation, suggesting the existence of a network structure within the composite elastomer. Moreover, composite elastomers filled with smaller silica particles (51 and 22 nm), which seem to be more likely to aggregate, showed higher Young's modulus from smaller filler amounts.

Fukahori et al. explained that the Young's modulus of reinforced rubber becomes higher than the Guth-Gold relation when there is a filler network parallel to the elongation direction and proposed a modified Guth-Gold equation that takes into account the effect of this filler network.^[15] TEM images of S40 showed that the silica particles were aligned

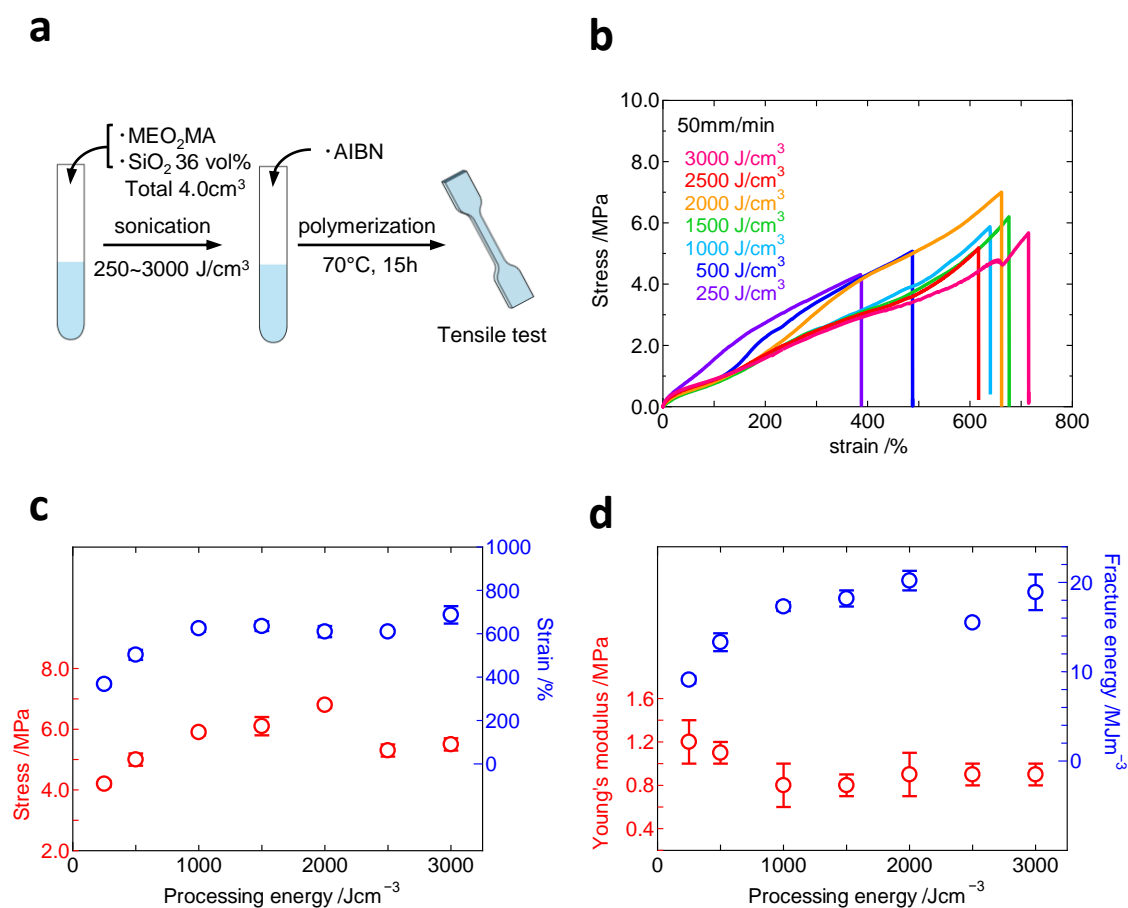


Figure 2-9. Examination of sonication processing energy for dispersing silica particles (a) Schematic illustration of the examination procedure. (b) Strain-stress curves of the composite elastomers to which different values of processing energy were applied. (c) Stress and strain at break at different values of processing energy. (d) Young's modulus and fracture energy at different values of processing energy.

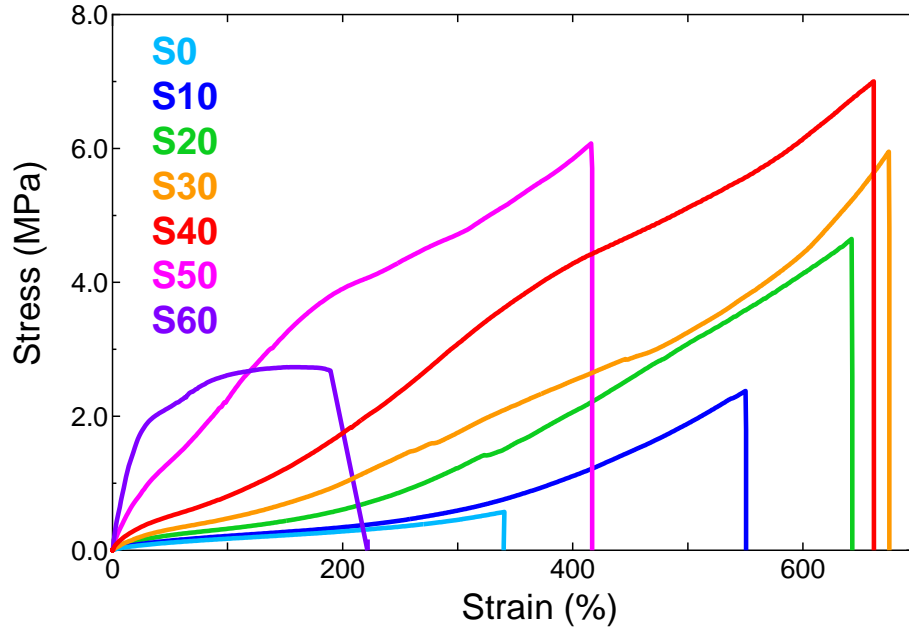


Figure 2-10. Stress-strain curves of composite elastomers in which various amounts of 110 nm silica particles are dispersed.

Table 2-2. Stress-strain curves of composite elastomers in which various amounts of 110 nm silica particles are dispersed.

| Composite Elastomer | ϕ [vol%] | E [MPa] | σ_f [MPa] | ε_f [%] | Γ [MJ m ⁻³] |
|---------------------|------------------|-----------------|---------------------|------------------------|-----------------------------------|
| S0 | 0 | 0.23 ± 0.02 | 0.5 ± 0.0 | 321 ± 12 | 0.8 ± 0.1 |
| S10 | 9.8 | 0.25 ± 0.03 | 2.3 ± 0.2 | 555 ± 21 | 4.2 ± 0.4 |
| S20 | 19.7 | 0.38 ± 0.03 | 5.0 ± 0.4 | 654 ± 20 | 12.1 ± 1.0 |
| S30 | 29.6 | 0.58 ± 0.10 | 6.4 ± 0.3 | 725 ± 20 | 18.9 ± 1.5 |
| S40 | 38.6 | 0.85 ± 0.15 | 6.8 ± 0.1 | 610 ± 26 | 20.2 ± 1.1 |
| S50 | 48.6 | 1.31 ± 0.10 | 6.0 ± 0.2 | 385 ± 13 | 13.7 ± 0.8 |
| S60 | 58.4 | 3.58 ± 0.76 | 2.5 ± 0.1 | 118 ± 36 | 2.9 ± 1.0 |

ϕ : SiO₂ fraction in the composite elastomer, E : Young's modulus, σ_f : Stress at break, ε_f : Strain at break, Γ : Fracture energy

with small intervals and without any contact. (**Figure 2-12**) From this result, it was also found that the silica particles formed almost no agglomeration and were fixed in the composite elastomer. The fracture energy of S40 (20.2 MJ m^{-3}), which was the toughest among the composite elastomers, was 25 times higher than that of S0 (0.8 MJ m^{-3}). The Poisson's ratio of S40 was 0.48 (**Figure 2-13**), and the composite elastomer showed incompressibility similar to that of general rubbers.

Figure 2-14 shows the relation between the fracture energy of S10–S60 and the particle surface distance calculated from the particle size and the amount of filler. These plots were well fitted to a log-normal distribution type curve, and the particle surface distance was approximately 30 nm at the maximum point of the curve. This result reveals that there is an important relationship between the fracture energy of composite elastomers and the particle surface distance, which is due to their structure. The increase in the fracture energy of the composite elastomer, where few aggregation networks are expected to be present, implies the presence of a strong interaction between the polymer matrix and the silica particles. Therefore, it was believed that clarifying the nature of the polymer matrix-particle interaction by direct observation techniques would provide important insights into the reinforcement of the composite elastomer.

2-3-4. Nanoscale Mapping of the Composite Elastomers.

To clarify the nanostructure of the composite elastomer, the morphology was observed by using AFM. The elastic modulus mapping image of the composite elastomer revealed the presence of an interface layer (IL) with a higher Young's modulus than the matrix near the silica particles (**Figure 2-15a**). This high modulus IL, which is generally called bound rubber, should play an important role in the reinforcement of composite

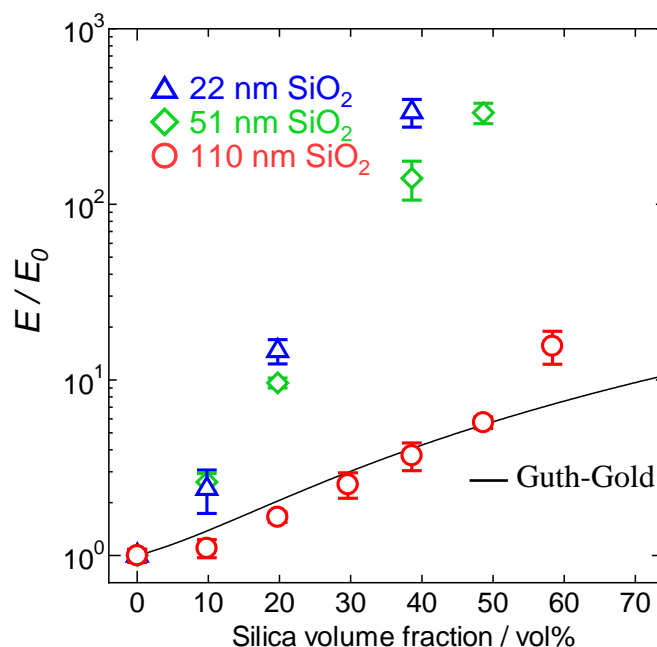


Figure 2-11. Young's moduli of composite elastomers containing different silica particle sizes. Symbols: \circ – 110 nm silica particles (Silibol®110, Fuji Chemical); \diamond – 51 nm silica particles (Silibol®ME50, Fuji Chemical) \triangle – 22 nm silica particles (ME-ST-M, Nissan Chemical). The line shows the correlation between Young's moduli and filler amounts expected from the Guth-Gold relation.

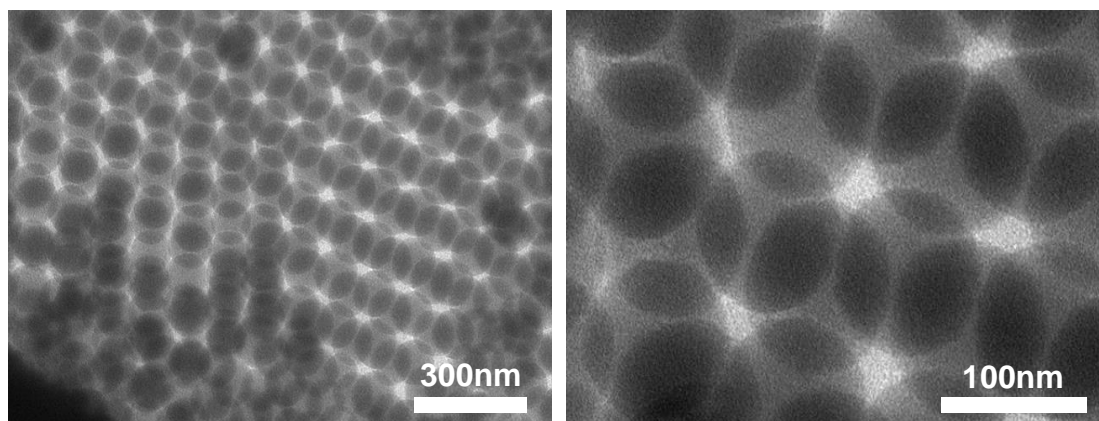


Figure 2-12. Cross-sectional TEM image of the composite elastomer S40.

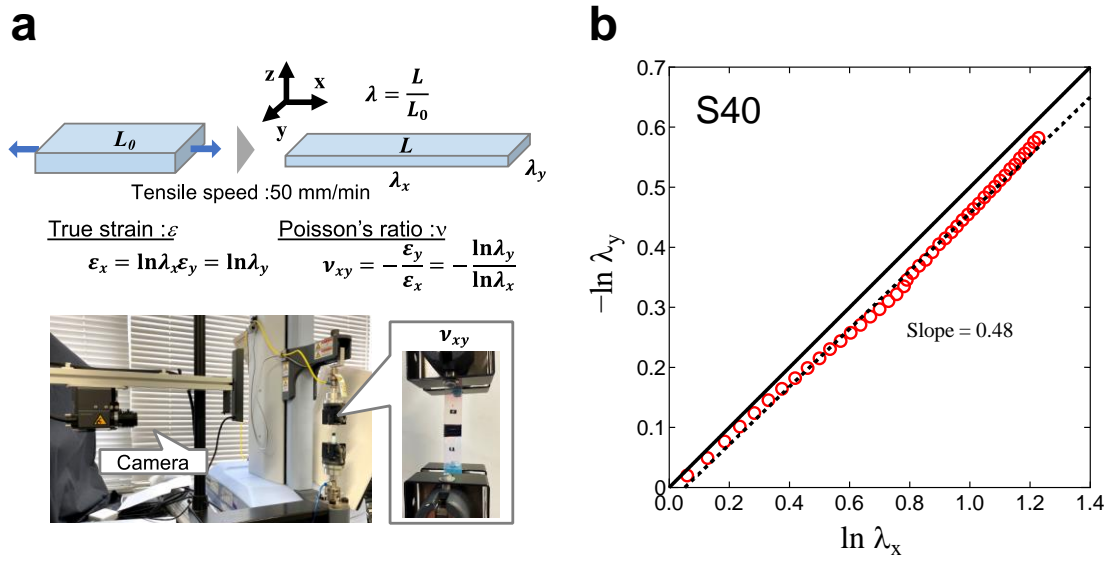


Figure 2-13. Poisson's ratio measurement of the composite elastomer. (a) Method for measuring Poisson's ratio for the stretching direction and the width direction (ν_{xy}). (b) Poisson's ratio of S40.

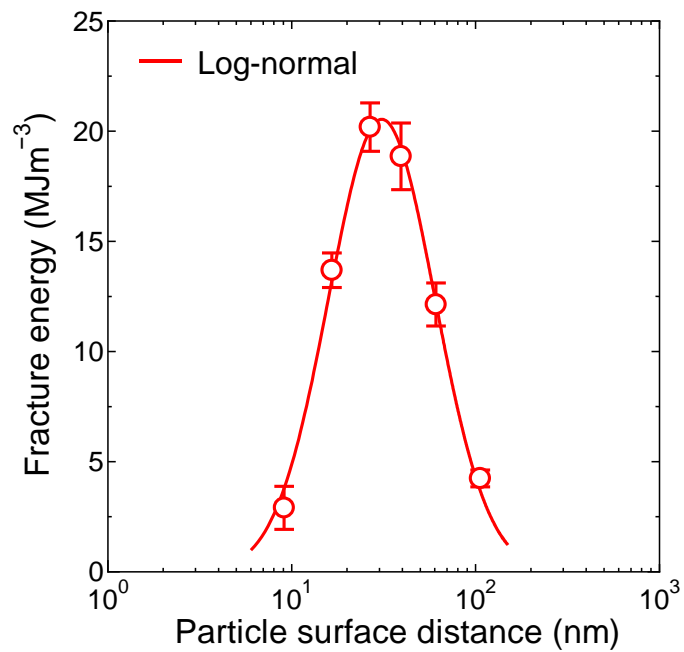


Figure 2-14. Fracture energies at different particle surface distances of silica particles.

elastomers.^[16] The cross-sectional profile (red line) through the center of the silica particles in the mapping image is shown in **Figure 2-15b**. In this cross-section profile, the width of the region where the Young's modulus is rising is the diameter of the IL. Then, the cross-sectional profile of the work of adhesion mapping image was obtained at the same region (**Figure 2-15c** and **2-15d**). On the cross-sectional profile, the part with a low adhesive force is considered to match the diameter of the silica particles and is measured at 119.4 nm. The thickness of the interface layer was determined from the difference between the IL size and the diameter of the silica particle, and the values were 12.7 and 18.3 nm. In this composite elastomer, an IL of approximately 15 nm was formed from the surface of the silica particles. In other words, the distance between the surfaces of the silica particles is approximately 30 nm when the interface layers just contact each other. This value corresponds to the particle surface distance when the fracture energy is maximized in the uniaxial tensile test.

In order to obtain more quantitative information on ILs, we performed Step-scan DSC measurements, a special variant of temperature modulated DSC, to confirm the T_g and the change in specific heat capacity ΔC_p at the glass transition (**Figure 2-16a**). The correlation of the volume fraction of silica particles and $\Delta C_{p \text{ composite}} / \Delta C_{p \text{ polymer}}$ is plotted in **Figure 2-16b**. $\Delta C_{p \text{ composite}}$ and $\Delta C_{p \text{ polymer}}$ are heat capacity changes of composite elastomers and a filler-free polymer (in this case PMEO₂MA), respectively. The black line with slope -1 is the fraction of silica particles that are not affected by thermal relaxation, and the area below this line represents the fraction of the polymer contributing to the glass transition in the composite elastomer. Polymer chains constrained on the silica surface in IL are considered to be rigid amorphous polymers with restrained α -relaxation at the glass transition. The fraction of constrained polymers in the composite material can

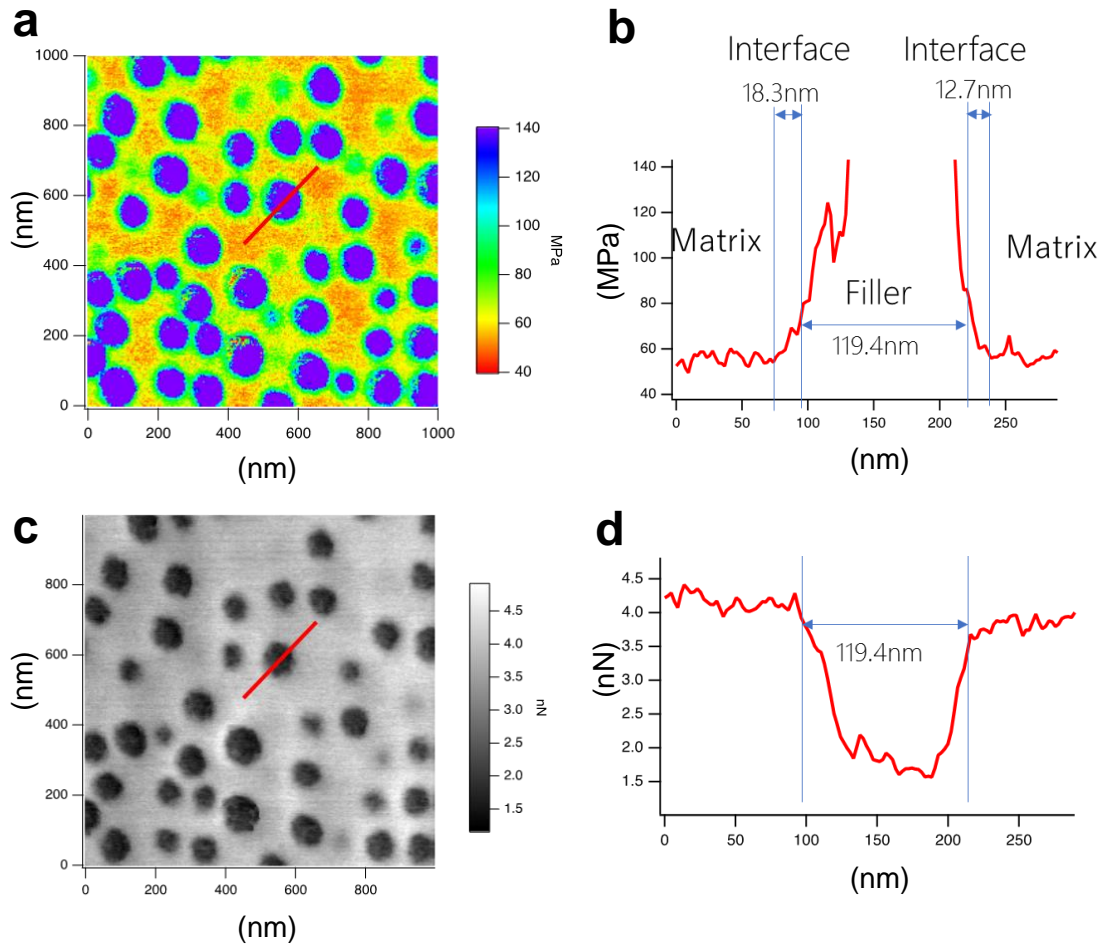


Figure 2-15. Analysis of the interface layer near the silica particles by using AFM. (a) Young's modulus map for S40. (b) The Young's modulus curve obtained from the red line in part a. (c) The work of adhesion map for S40. (d) The work of adhesion curve obtained from the red line in part c.

be denoted as the rigid amorphous fraction (RAF) following eq. 5. [17–19]

$$\text{RAF} = 1 - \phi_f - \frac{\Delta C_{p \text{ composite}}}{\Delta C_{p \text{ polymer}}} \quad (5)$$

where ϕ_f is the weight fraction of filler.

$\Delta C_{p \text{ composite}} / \Delta C_{p \text{ polymer}}$ refer to the fraction of polymers involved in the calorimetric relaxation at the glass transition and is called mobile amorphous fraction (MAF). The $\Delta C_{p \text{ composite}} / \Delta C_{p \text{ polymer}}$ is lower than the black line, which means that there is RAF in composite elastomers. The $\Delta C_{p \text{ composite}} / \Delta C_{p \text{ polymer}}$ decreased with increasing amounts of silica particles, but the change was smaller from 40 vol%. Based on the AFM results, this silica particles fraction is expected to be the situation where the ILs are in contact, the overlap of ILs is considered to increase until silica particles reach the closed packing (74 vol%). As the overlap of ILs increases, the RAF decreases, which can be seen in the change of $\Delta C_{p \text{ composite}} / \Delta C_{p \text{ polymer}}$ above 40 vol%. For further discussion, the RAF in volume was plotted as a function of the particle surfaces distance (**Figure 2-16c**). The RAF shows a maximum at an approximately 30 nm and this result correlates with the fracture energy. It can be concluded that the significant reinforcing effect appears when the fraction of ILs supporting the toughness of composite elastomers is the highest.

From these result, it can be inferred that the IL plays a role in reinforcing the composite elastomer as follows (**Figure 2-16d**). When the amount of silica particles is less than 38.6 vol%, the polymer chains in the matrix polymer are entangled with the IL, and the stress concentration during deformation is considered to be caused at the inside of IL.^[20] As the amount of silica particles increases, the increase in IL fraction leads to an enhancement of fracture energy.

At 38.6 vol%, the ILs are just in contact, and it is inferred that a three-dimensional polymer network with a high Young's modulus is formed. This

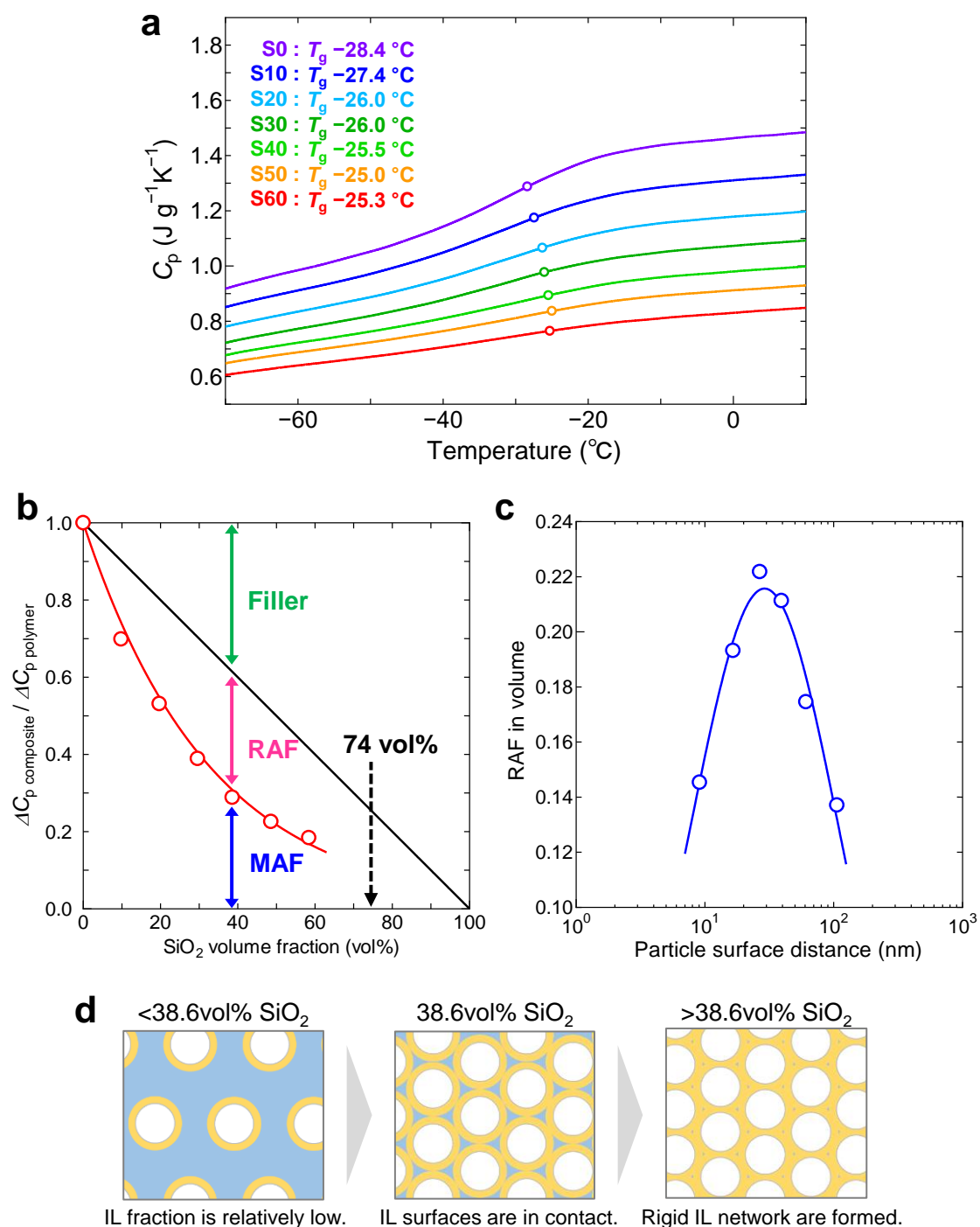


Figure 2-16. (a) Specific heat capacity of composite elastomers. Open symbols indicate the glass transition temperatures. (b) Calorimetric relaxation strength as a function of silica particles content. The vertical double arrows indicate the amount of filler, RAF and MAF for S40 (38.6 vol% SiO_2). (c) RAFs in volume at different particles surface distances of silica particles. (d) A conceptual diagram for predicting the particle morphology at different silica particle amounts.

interconnected IL network is expected to support the large stress concentration around silica particles. During deformation, "molecular slippage"^[20,21] might occur at the silica-polymer interface in the network created by IL. Homogenization of the bridging segments by repeated adsorption and detachment of the polymer chains onto the silica surface might alleviate the local stress concentration. This continuous stress relaxation and the highest IL fraction are thought to lead to a significant increase in fracture energy.

At concentrations above 38.6 vol%, the IL fraction reduces due to its overlap, and the polymer chains in the IL are strongly adsorbed by two silica particles. In other words, local stress concentration due to strong entanglement takes precedence over molecular slippage. Then, it is presumed that the breakage of the stretched molecular chains and the detachment of the polymer from the silica surface reduce the ductility of the composite elastomer. This result is thought to provide new insights into the reinforcing phenomenon by using a composite elastomer in which spherical silica particles with a uniform size are dispersed without aggregation. The adsorption of the polymer chains on the silica surface is considered to be important in the formation of the IL and the reinforcing effect.^[22–24]

Here, to verify the factors of the interaction between PMEO₂MA and silica particles, the Hansen solubility parameter (HSP)^[25] was considered. HSP can be useful to predict the solubility of a substance and is based on the idea that two substances with similar intermolecular interactions are easily soluble in each other. HSP is expressed using eq. 6

$$\delta_T^2 = \delta_D^2 + \delta_P^2 + \delta_H^2 \quad (6)$$

δ_T , δ_D , δ_P , and δ_H are the total parameter, dispersion, polar, hydrogen-bonding, respectively. These three parameters can be regarded as coordinates in three-dimensional

space (Hansen space). When HSPs of two substances are placed in Hansen space, it is shown that the closer the distance between the two points, the easier it is to dissolve each other. By using HSP, the dispersibility of particles in a medium can also be predicted. The contribution of these three parameters is predicted by the following method when a certain particle is dispersed in a certain solvent. First, the HSP of the silica particle was determined by evaluating the dispersibility of silica particles in HSP-known solvents (20 solvents) based on the results of particle size distribution measurements (**Figure 2-17a** and **Table 2-3**). A Hansen sphere (green mesh sphere in **Figure 2-17a**) with all the “good” solvents on the inside and all the “poor” solvents on the outside was created, and the center of the sphere was the HSP of the silica particle. Here, the radius of the sphere (R_0) defines the limit of a “good” solvent to disperse the silica particle. For PMEO₂MA, the HSP of the MEO₂MA monomer was calculated for simplicity according to the calculation method reported by Stefanis et al. (**Table 2-4**).^[26] Then, the HSP distance (R_a) and the relative energy difference (RED) between the silica particle and MEO₂MA are expressed by eq. 7 and 8,

$$R_a^2 = 4(\delta_{D1} - \delta_{D2})^2 + (\delta_{P1} - \delta_{P2})^2 + (\delta_{H1} - \delta_{H2})^2 \quad (7)$$

$$RED = \frac{R_a}{R_0} \quad (8)$$

To obtain the value of R_a using eq. 6, the value of the difference between the parameters of substance 1 and substance 2 is required. That is, the values of the respective parameters of the silica particles and MEO₂MA (**Figure 2-17b**). RED is the indicator of the affinity between two substances. If the RED is less than 1, HSP is inside the Hansen sphere and is a “good” solvent.

The R_a and RED between the silica particles and MEO₂MA were calculated as 3.4 MPa^{1/2} and 0.36, respectively. The RED value indicates that the dispersibility of the

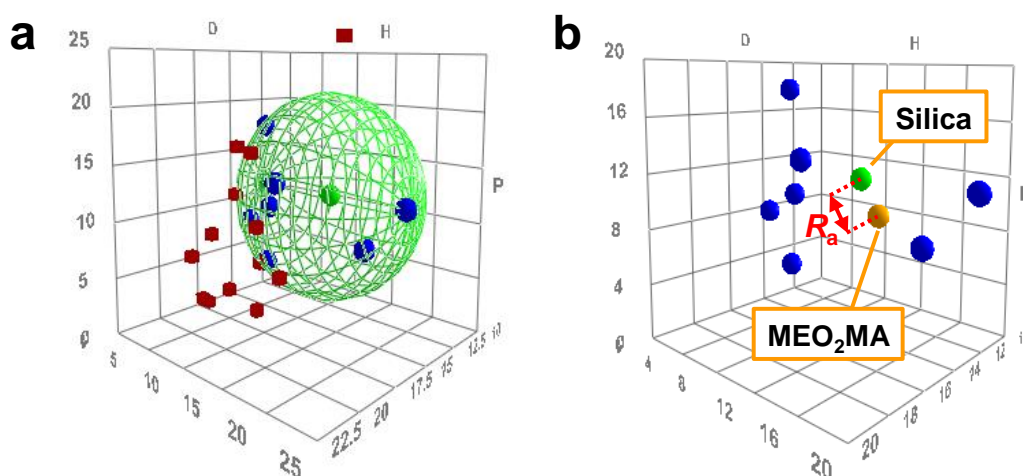


Figure 2-17. (a) Hansen sphere of the silica particle. The blue circles and red squares denote the good and poor solvents for dispersion, respectively. The center of the sphere is defined as the HSP of the silica particles. (b) The HSP of the silica particle and MEO₂MA in Hansen space. The Hansen distance R_a is the value of the difference between these.

Table 2-3. Good and poor solvents for silica particles in the determination of HSP

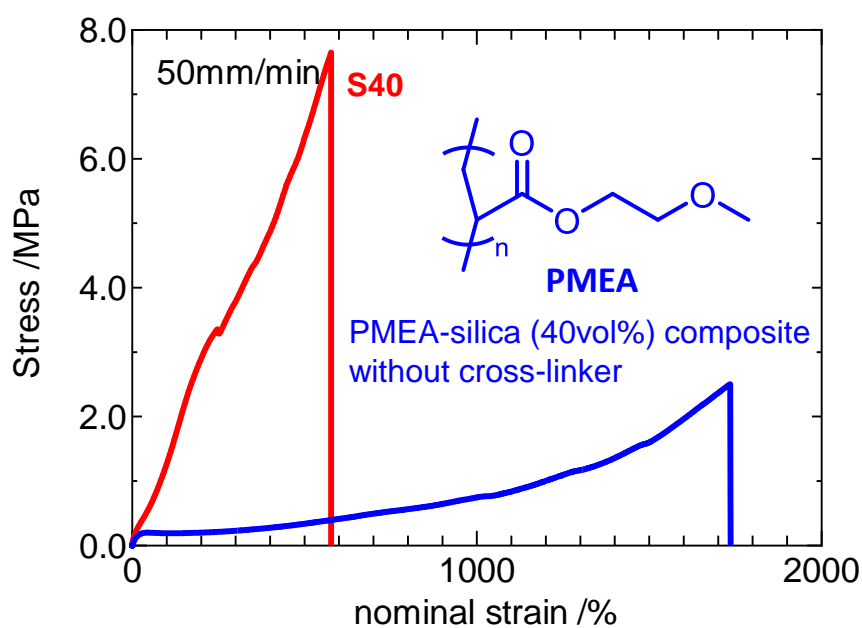
| Solvent | δ_D [(MPa) ^{1/2}] | δ_P [(MPa) ^{1/2}] | δ_H [(MPa) ^{1/2}] | Z-Ave ^{a)} [nm] | PDI ^{b)} | Dispersibility ^{c)} |
|--------------------------------|---------------------------------------|---------------------------------------|---------------------------------------|-----------------------------|-------------------|------------------------------|
| Ethyl acetate | 15.8 | 5.3 | 7.2 | 163.5 | 0.01 | Good |
| Ethanol | 15.8 | 8.8 | 19.4 | 136.2 | 0.02 | Good |
| 2-Butanone (MEK) | 16.0 | 9.0 | 5.1 | 151.5 | 0.03 | Good |
| Acetone | 15.5 | 10.4 | 7.0 | 162.5 | 0.05 | Good |
| Methanol | 14.7 | 12.3 | 22.3 | 133.7 | 0.07 | Good |
| Acetonitrile | 15.3 | 18.0 | 6.1 | 148.0 | 0.07 | Good |
| <i>N,N</i> -Dimethylformamide | 17.4 | 13.7 | 11.3 | 152.0 | 0.07 | Good |
| Benzyl alcohol | 18.4 | 6.3 | 13.7 | 128.1 | 0.09 | Poor |
| Dimethyl sulfoxide | 18.4 | 16.4 | 10.2 | 144.0 | 0.14 | Poor |
| 1,4-Dioxane | 17.5 | 1.8 | 9.0 | 165.2 | 0.18 | Poor |
| Salicylaldehyde | 19.0 | 10.5 | 12.0 | 112.2 | 0.18 | Poor |
| γ -Butyrolactone | 18.0 | 16.6 | 7.4 | 147.6 | 0.18 | Poor |
| <i>o</i> -Dichlorobenzene | 19.2 | 6.3 | 3.3 | 170.6 | 0.25 | Poor |
| <i>N</i> -Methyl-2-pyrrolidone | 18.0 | 12.3 | 7.2 | 243.2 | 0.25 | Poor |
| Formamide | 17.2 | 26.2 | 19.0 | 148.6 | 0.28 | Poor |
| Cyclohexane | 16.8 | 0.0 | 0.2 | 306.7 | 0.33 | Poor |
| Tetrahydrofuran | 16.8 | 5.7 | 8.0 | 173.5 | 0.35 | Poor |
| Pyridine | 17.9 | 6.5 | 7.4 | 164.3 | 0.60 | Poor |
| Trichloro methane | 17.8 | 3.1 | 5.7 | 2078.0 | 0.73 | Poor |
| Toluene | 18.0 | 1.4 | 2.0 | 3301.0 | 1.00 | Poor |

^{a)} Z-Average ^{b)} Polydispersity index ^{c)} Solvents with $PDI \leq 0.07$ were classified as good, and other solvents were classified as poor.

silica particles to MEO₂MA is very good. It is consistent with the previous test results. Furthermore, from the positions of fine silica particles and MEO₂MA in this Hansen space, the respective HSP values can be obtained. The δ_H of 2-methoxyethyl acrylate (MEA), the monomer of the PMEAs-silica composite elastomer^[12] is calculated to be 7.2. This value is lower than that of MEO₂MA (14.9), which is affected by the difference in the length of the side chains. In addition, the RED between MEA and the silica particles was 0.81, which means that MEO₂MA is a better “good” solvent than MEA. This suggests that the hydrogen-bonding strength of MEO₂MA to the silica surface is higher than that of MEA. While the stress-strain curve of the PMEAs-silica composite elastomer showed a small rise in stress below 500% nominal strain, the stress rose from low strain in S40 consisting of MEO₂MA (**Figure 2-18**). If covalent bonds between silica particles and polymer chains form during the polymerization process and act as crosslinking points, then the stress in PMEAs should rise at low strain. It can be assumed that PMEO₂MA, which has the same functional groups as PMEAs, also does not form covalent bonds with silica particles. In the uniaxial cyclic tensile test of S40, the residual strain up to 100% strain was small, and the shape recovery was good, even though no cross-linking agent was used (**Figure 2-19**). The presence of hysteresis loops, referred to as the Mullins effect, can be attributed to the buckling of extended or oriented polymer bundles.^[20] This phenomenon suggests the presence of strong cross-linking effected physically between polymer chains and silica particles. In the PMEO₂MA-silica composite elastomer, the interaction between polymer chains and the silica surface due to hydrogen bonding, as shown in **Figure 2-20**, might act as pseudo-cross-linking points. The surface charge density measurement results implied ionization of the silanol group on the silica surface, supporting the existence of that chemical structure.

Table 2-4. Hansen solubility parameters of silica particles and MEO₂MA

| Substance | δ_D [(MPa) ^{1/2}] | δ_P [(MPa) ^{1/2}] | δ_H [(MPa) ^{1/2}] | δ_T [(MPa) ^{1/2}] | R_0 [(MPa) ^{1/2}] |
|---------------------|---------------------------------------|---------------------------------------|---------------------------------------|---------------------------------------|----------------------------------|
| Silica | 14.3 | 12.0 | 13.0 | 22.7 | 9.4 |
| MEO ₂ MA | 15.2 | 9.9 | 14.9 | 23.5 | - |

**Figure 2-18.** Stress-strain curves of S40 and the PMEA-silica composite elastomer without cross-linker.

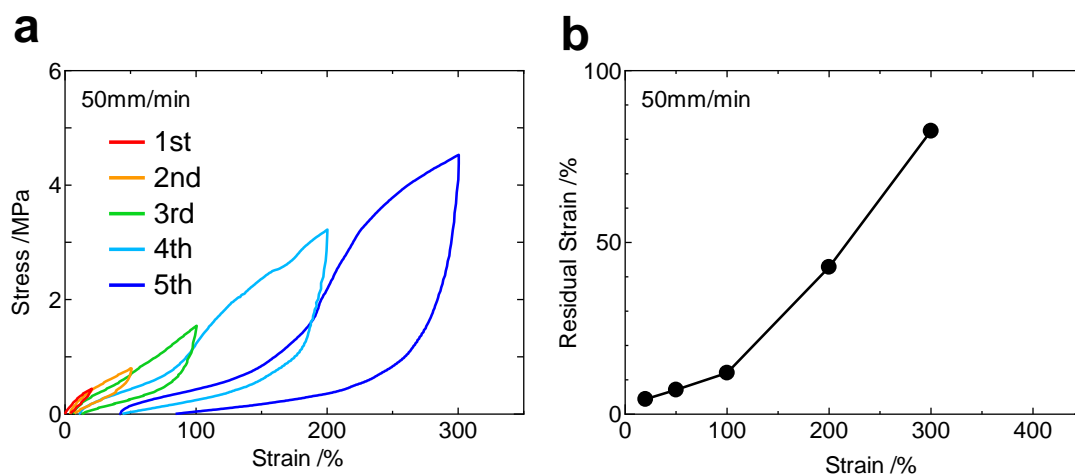


Figure 2-19. Hysteresis property of S40. The composite elastomer was deformed to a predetermined strain and then recovered until the stress reached zero. A series of cycles at each predetermined strain (20, 50, 100, 200 and 300% at 50 mm/min) was performed sequentially, and the results were measured up to when the specimens broke. (a) Stress-strain curve of S40 from the hysteresis measurement. (b) Dependence of the residual strain on the predetermined strain.

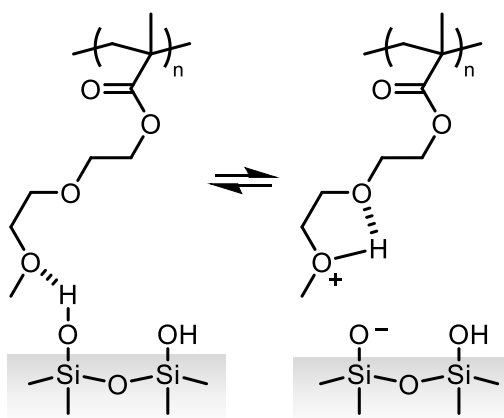


Figure 2-20. Schematic for predicting the side chain structure forming the hydrogen bond.

2-3-5. Vibration-Damping Property of the Composite Elastomer,

Finally, to demonstrate the potential applications of the composite elastomer, the vibration-damping property was evaluated. The vibration-damping performance is said to be the effect of friction between the filler and the matrix polymer, which dissipates the deformation energy as thermal energy.^[27–29] In the composite elastomer filled with silica particles at intervals of a few nanometers, thermal energy dissipation due to shear strain among the particles and friction at the particle-polymer interface is expected. Therefore, an unconstrained composite beam was fabricated by attaching a composite elastomer to a steel beam (**Figure 2-21**), and the loss factor obtained from the frequency response function when the center of this specimen was vibrated was compared.^[30] The loss factor was obtained from eq. 9 using the peak position f of the antiresonance point of the frequency response function and the half-width Δf at the position 3 dB down from the peak maximum value (**Figure 2-22**).^[31,32]

$$\eta = \frac{\Delta f}{f} \quad (9)$$

The measurements were taken at -20, -10, 0, 10, 20, 30 and 40 °C, and the antiresonance peaks from the second to the seventh order were used for analysis (**Figure 2-23**). The loss factors of the composite beams obtained at each temperature were converted to a nomogram based on the time–temperature superposition principle (**Figure 2-24**). The William–Landel–Ferry shift factor α_T was obtained from eq. 10.^[33]

$$\log(\alpha_T) = \frac{-C_1(T - T_r)}{C_2 + (T - T_r)} \quad (10)$$

where T is the measurement temperature and C_1 , C_2 , and T_r were used at 8.86, 101.6, and 5 °C, respectively. The loss factor of S40, which has the highest fracture energy, is much higher than that of S0, indicating that it is a transparent material with good vibration-

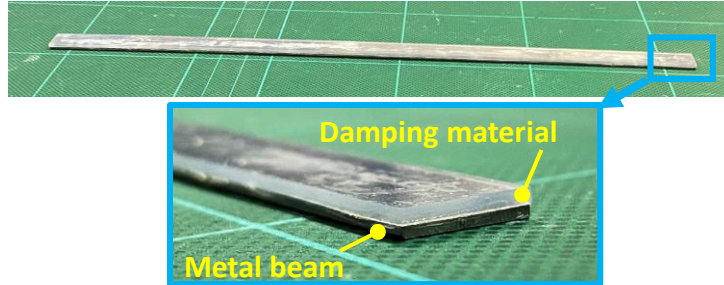


Figure 2-21. A conceptual diagram for indicating the measurement procedure of the loss factor.

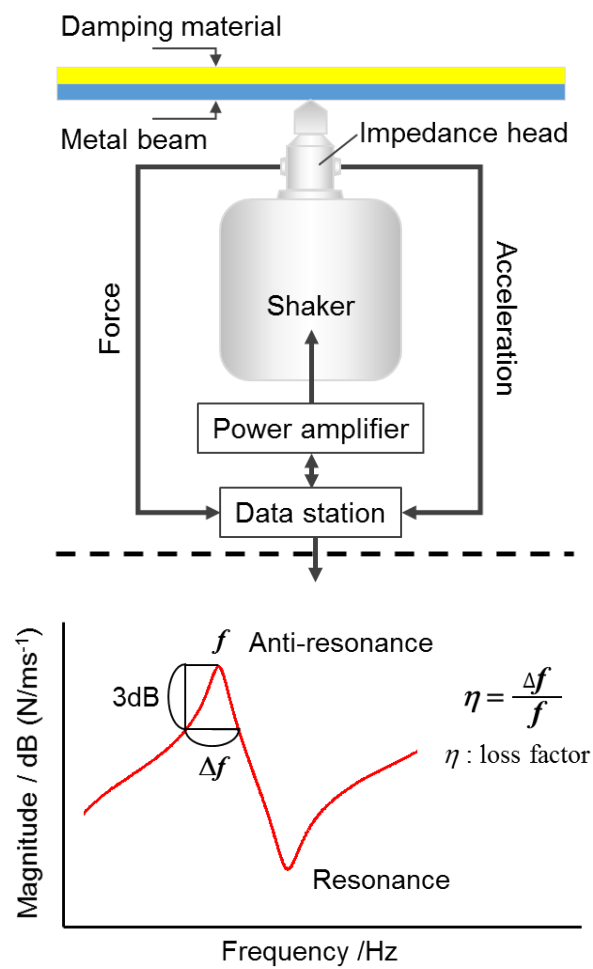


Figure 2-22. Image showing the specimen of the unconstrained composite beam with the composite elastomer.

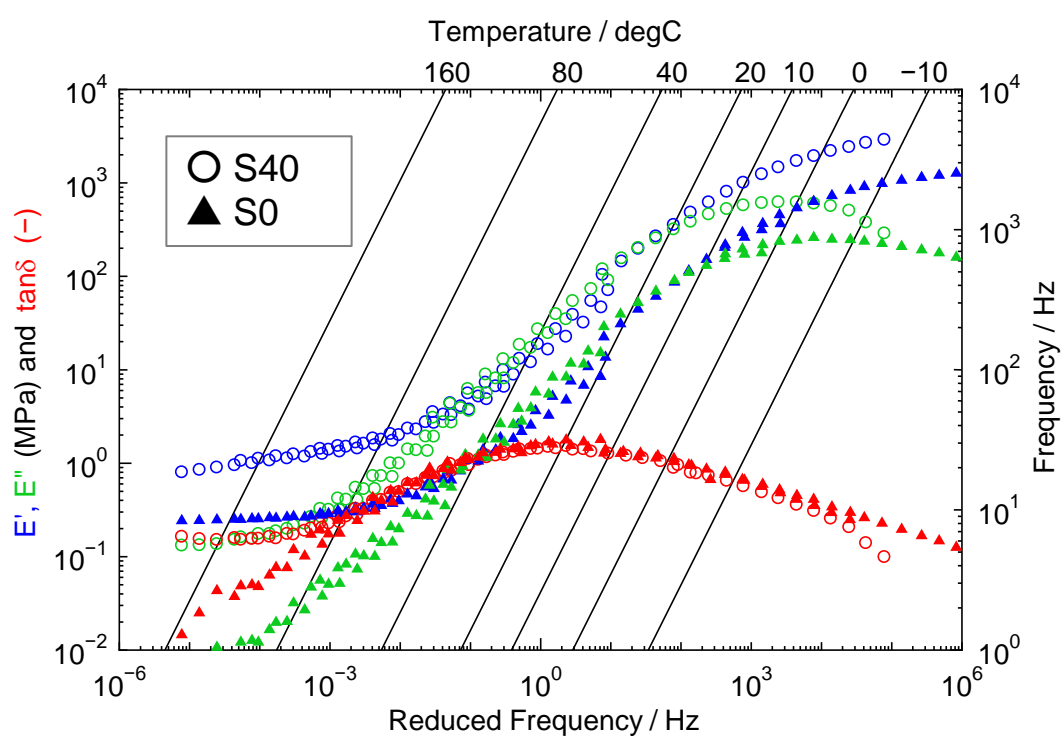


Figure 2-26. The mater curves of the composite elastomer.

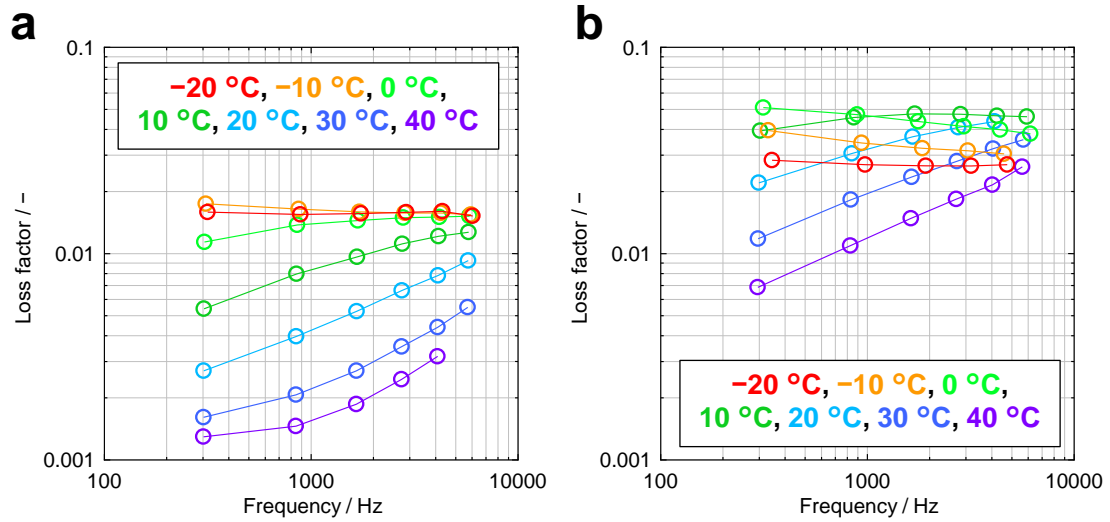


Figure 2-24. The loss factor of the unconstrained composite beam with the composite elastomer. (a) The loss factor of the unconstrained composite beam with S0. (b) The loss factor of the unconstrained composite beam with S40.

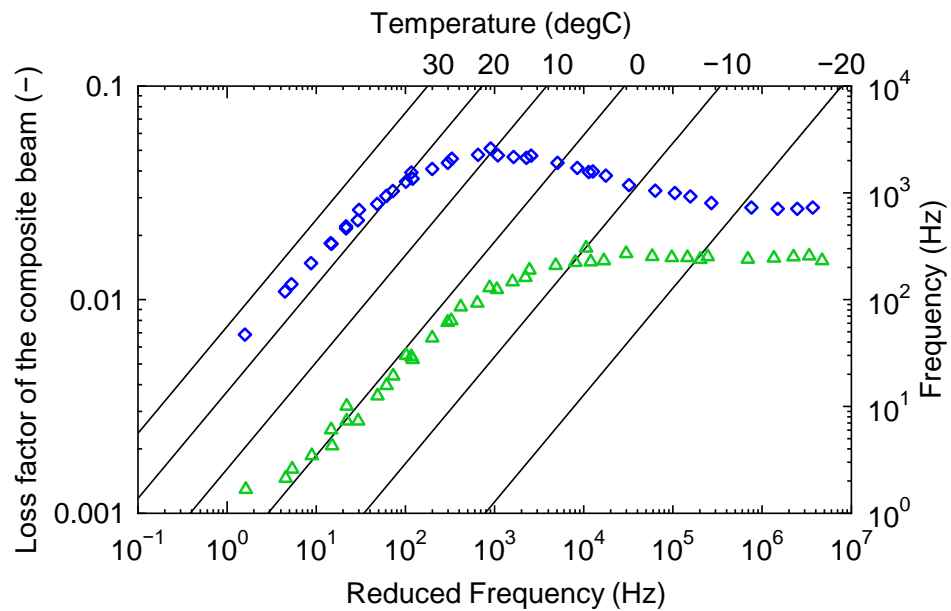


Figure 2-25. The loss factor nomogram of S0 and S40.

damping performance. The $\tan\delta$ of polymer materials in dynamic viscoelasticity is often used to compare the dissipation ability of deformation energy. The dynamic viscoelasticity measurements of S0 and S40 revealed little difference in $\tan\delta$ between them, but the storage and loss modulus were increased by silica filling (**Figure 2-25**).

Generally, damping materials are used in contact with a source of vibration such as metal or glass, and it is thought that the elastic modulus must be sufficient to suppress the deformation of the base material to exhibit vibration-damping properties. The composite elastomer has a higher storage modulus due to the reinforcing effect of the silica particles and a higher loss modulus due to the increased friction between the particles and the polymer matrices, which probably contributes to the improvement of vibration-damping properties. Most filler-filled polymer materials with vibration-damping properties are opaque, but the composite elastomer in this study is expected to be applied as a new highly transparent vibration damping material.

The loss factor of the composite beam with the composite elastomer was high in the range of 1–2 kHz. In recent years, the shift to hybrid electric vehicles (HEVs) and electric vehicles (EVs) has been promoted, and it has been reported that the noise in the 1–2 kHz band is higher in HEVs than in automobiles with conventional engines.^[34] With the need to address global environmental issues, the electrification of automobiles is an important issue that cannot be avoided, and composite elastomers with high transparency and vibration-damping properties are expected to be applied as materials for next-generation vehicles.

2-4. Conclusions

The transparent composite elastomer with greatly improved mechanical

properties was prepared by filling PMEO₂MA with a high concentration of monodispersed spherical silica particles without an organic cross-linker. The stress and strain at break of the composite elastomer increased with increasing amounts of silica particles, and the fracture energy of S40 was 25 times higher than that of S0. Nanoscale mapping of the composite elastomer using AFM showed the presence of an IL of approximately 15 nm thickness with a high elastic modulus near the silica particles. The fracture energy of the composite elastomer was considered to be maximum when the ILs of the silica particles were just in contact (the particle surface distance was approximately 30 nm). We succeeded in obtaining real-space information on a bound polymer, which could not be obtained by previous methods using solvents^[35–40] or by observing the bulk^[23,41–47], which is susceptible to segmental structures. The results of the surface charge density measurement and HSP comparison suggested that the polymer chains were adsorbed on the silica surface due to the ionization of silanol groups and hydrogen-bonding interactions. In the vibration-damping evaluation, a significant improvement in the loss factor was observed by filling the silica particles, indicating the potential of the composite elastomer to be applied as an interlayer film for laminated glass in automotive and architectural applications. We believe that the results revealed by using the material with a simple composition in this study will greatly contribute to the elucidation of the reinforcement mechanism of composite elastomers, which is influenced by complex factors, and the development of novel materials that support new lifestyles.

References

- [1] H. Gotoh, C. Liu, A. Bin Imran, M. Hara, T. Seki, K. Mayumi, K. Ito, Y. Takeoka, *Sci. Adv.* **2018**, *4*, eaat7629.

- [2] S. Bauer, S. Bauer-Gogonea, I. Graz, M. Kaltenbrunner, C. Keplinger, R. Schwödiauer, *Adv. Mater.* **2014**, 26, 149.
- [3] M. L. Hammock, A. Chortos, B. C. K. Tee, J. B. H. Tok, Z. Bao, *Adv. Mater.* **2013**, 25, 5997.
- [4] T. Kajita, A. Noro, Y. Matsushita, *Polymer (Guildf)*. **2017**, 128, 297.
- [5] S. S. Sheiko, A. V. Dobrynin, *Macromolecules* **2019**, 52, 7531.
- [6] Z. Wang, C. Xiang, X. Yao, P. Le Floch, J. Mendez, Z. Suo, *Proc. Natl. Acad. Sci. U. S. A.* **2019**, 116, 5967.
- [7] K. Watanabe, E. Miwa, F. Asai, T. Seki, K. Urayama, T. Nakatani, S. Fujinami, T. Hoshino, M. Takata, C. Liu, K. Mayumi, K. Ito, Y. Takeoka, *ACS Mater. Lett.* **2020**, 2, 325.
- [8] K. L. Johnson, K. Kendall, A. D. Roberts, *Proc. R. Soc. Lond. A. Math. Phys. Sci.* **1971**, 324, 301.
- [9] V. . Shilov, Y. . Borkovskaja, A. . Dukhin, *J. Colloid Interface Sci.* **2004**, 277, 347.
- [10] P. N. Pusey, W. Van Megen, *Nature* **1986**, 320, 340.
- [11] W. K. Kegel, A. van Blaaderen, *Science (80-.)*. **2000**, 287, 290.
- [12] F. Asai, T. Seki, A. Sugawara-Narutaki, K. Sato, J. Odent, O. Coulembier, J.-M. Raquez, Y. Takeoka, *ACS Appl. Mater. Interfaces* **2020**, 12, 46621.
- [13] R. Ishige, G. A. Williams, Y. Higaki, N. Ohta, M. Sato, A. Takahara, Z. Guan, *IUCrJ* **2016**, 3, 211.
- [14] E. Guth, *J. Appl. Phys.* **1945**, 16, 20.
- [15] Y. Fukahori, A. A. Hon, V. Jha, J. J. C. Busfield, *Rubber Chem. Technol.* **2013**, 86, 218.

- [16] K. Nakajima, M. Ito, H. K. Nguyen, X. Liang, *Rubber Chem. Technol.* **2017**, 90, 272.
- [17] A. Sargsyan, A. Tonoyan, S. Davtyan, C. Schick, *Eur. Polym. J.* **2007**, 43, 3113.
- [18] Y. S. Lipatov, V. P. Privalko, *Polym. Sci. U.S.S.R.* **1972**, 14, 1843.
- [19] V. P. Privalko, Y. S. Lipatov, Y. Y. Kercha, *Polym. Sci. U.S.S.R.* **1970**, 12, 1520.
- [20] Y. Fukahori, *J. Appl. Polym. Sci.* **2005**, 95, 60.
- [21] J.-B. Donnet, E. Custodero, in *Sci. Technol. Rubber*, Elsevier, **2013**, pp. 383–416.
- [22] S. Cheng, B. Carroll, V. Bocharova, J.-M. Carrillo, B. G. Sumpter, A. P. Sokolov, *J. Chem. Phys.* **2017**, 146, 203201.
- [23] E. J. Bailey, K. I. Winey, *Prog. Polym. Sci.* **2020**, 105, 101242.
- [24] S. Napolitano, *Soft Matter* **2020**, 16, 5348.
- [25] C. M. Hansen, A. L. Smith, *Carbon N. Y.* **2004**, 42, 1591.
- [26] E. Stefanis, C. Panayiotou, *Int. J. Thermophys.* **2008**, 29, 568.
- [27] S. Praveen, J. Bahadur, R. Yadav, S. Billa, T. Umasankar Patro, S. K. Rath, D. Ratna, M. Patri, *Appl. Acoust.* **2020**, 170, 107535.
- [28] X. Q. Zhou, D. Y. Yu, X. Y. Shao, S. Q. Zhang, S. Wang, *Compos. Struct.* **2016**, 136, 460.
- [29] B. C. Nakra, *J. Sound Vib.* **1998**, 211, 449.
- [30] S. TAKADA, K. SUZUKI, *Trans. Japan Soc. Mech. Eng. Ser. C* **2001**, 67, 2113.
- [31] P. P. Hujare, A. D. Sahasrabudhe, *Procedia Mater. Sci.* **2014**, 5, 726.
- [32] E. ADACHI, J. SATOH, *JSME Int. journal. Ser. 3, Vib. Control Eng. Eng. Ind.* **1992**, 35, 343.
- [33] M. L. Williams, R. F. Landel, J. D. Ferry, *J. Am. Chem. Soc.* **1955**, 77, 3701.
- [34] L. Liao, Y. Zuo, H. Meng, X. Liao, *Adv. Mech. Eng.* **2018**, 10,

168781401876691.

- [35] S. Napolitano, M. Wübbenhorst, *Nat. Commun.* **2011**, 2, 1.
- [36] P. Gin, N. Jiang, C. Liang, T. Taniguchi, B. Akgun, S. K. Satija, M. K. Endoh, T. Koga, *Phys. Rev. Lett.* **2012**, 109, 265501.
- [37] N. Jouault, J. F. Moll, D. Meng, K. Windsor, S. Ramcharan, C. Kearney, S. K. Kumar, *ACS Macro Lett.* **2013**, 2, 371.
- [38] E. Senses, P. Akcora, *RSC Adv.* **2014**, 4, 49628.
- [39] N. Jouault, D. Zhao, S. K. Kumar, *Macromolecules* **2014**, 47, 5246.
- [40] N. Jiang, M. K. Endoh, T. Koga, T. Masui, H. Kishimoto, M. Nagao, S. K. Satija, T. Taniguchi, *ACS Macro Lett.* **2015**, 4, 838.
- [41] A. P. Holt, P. J. Griffin, V. Bocharova, A. L. Agapov, A. E. Imel, M. D. Dadmun, J. R. Sangoro, A. P. Sokolov, *Macromolecules* **2014**, 47, 1837.
- [42] A. C. Genix, V. Bocharova, A. Kisliuk, B. Carroll, S. Zhao, J. Oberdisse, A. P. Sokolov, *ACS Appl. Mater. Interfaces* **2018**, 10, 33601.
- [43] A. C. Genix, V. Bocharova, B. Carroll, M. Lehmann, T. Saito, S. Krueger, L. He, P. Dieudonné-George, A. P. Sokolov, J. Oberdisse, *ACS Appl. Mater. Interfaces* **2019**, 11, 17863.
- [44] E. J. Bailey, P. J. Griffin, R. J. Composto, K. I. Winey, *Macromolecules* **2019**, 52, 2181.
- [45] A. M. Jimenez, D. Zhao, K. Misquitta, J. Jestin, S. K. Kumar, *ACS Macro Lett.* **2019**, 8, 166.
- [46] E. J. Bailey, P. J. Griffin, R. J. Composto, K. I. Winey, *Macromolecules* **2020**, 53, 2744.
- [47] W. You, W. Cui, W. Yu, *Polymer (Guildf)*. **2021**, 213, 123323.

Chapter III

Functional Polymethacrylate Composite Elastomer Filled with Multilayer Graphene and Silica Particles

3-1. Introduction

The discovery of graphene, which has distinctive characteristics among carbon materials, has opened new horizons for the development of novel composite materials.^[1-3] A single layer of graphene is a two-dimensional sheet formed by a honeycomb structure of sp^2 -bonded carbons and consists of one atomic thickness. This structure provides a high tensile strength,^[4] negligible gas permeability,^[5,6] excellent electrical conductivity and thermal conductivity.^[7-12] Much interest in academic research is not limited to single-layer graphene but extends to chemically modified graphene oxide (GO), reduced graphene oxide (RGO), and multilayer graphene (MLG).^[13-18] The high-aspect-ratio two-dimensional structure of these fillers gives the matrix material a specific function. To date, many studies have been reported on thermally conductive materials,^[11,12,19] sensors,^[20-23] reinforced elastomers,^[15,17,18,24] and electromagnetic interference materials.^[25-28] Single-layer graphene can be expected to have extremely high functionality, so applied research is mainly carried out on electronic devices that require high performance, but the associated production process is sophisticated and costly. Therefore, it is not practical to use this material as a component for polymer composite materials.^[9,13,15]

Among the aforementioned graphene families, the use of MLG, with its lower price, is the most realistic choice for the creation of practical functional materials. When focusing on electrical conductivity or thermal conductivity, especially in composites with insulating matrices, filler fillings with volume fractions above the percolation threshold

are effective. Therefore, improving filler dispersion and its control might be key techniques for commercial success.

Chakraborty et al. obtained MLG-silica-PS composites by dropping a mixture of dispersions of multilayer graphene and silica particles in a large amount of dimethylformamide (DMF) and a DMF solution of polystyrene (PS) into methanol, a poor solvent for PS.^[29] This composite achieves a massive enhancement of electrical conductivity with a smaller amount of MLG than the composite without silica particles because the silica particles inhibit the reaggregation of graphene sheets due to van der Waals forces after the dispersion process. The creation of such techniques to improve the dispersibility of MLG and enhance the functionality of composites is expected to provide new guidelines for applied research.

Based on the past reports, the addition of MLG into the MEO₂MA-silica composite elastomer could lead to a functional elastomer in which the reaggregation of graphene sheets is suppressed by silica particles. While most of the polymer composites based on GO, RGO, and MLG use a preparation method with a large amount of solvent for filler dispersion, the composite elastomers we demonstrated can be fabricated by a mild, solvent-free process.

In this chapter, the dispersibility of MLG and silica particles in MEO₂MA, which is a liquid monomer at room temperature, is first confirmed and the structure of the composite elastomer prepared from this dispersion is analyzed. A uniaxial tensile test of the composite elastomer was then performed to confirm the relationship between MLG filling and mechanical properties. Then, the evaluation of dielectric measurements revealed that the filling of MLG and silica particles allows for an increase in the dielectric constant while suppressing the increase in the dielectric loss tangent. In addition, silica

particle filling allowed for more MLG filling and improved the thermal conductivity of the composite elastomer. The vibration damping loss factor measurement using unconstrained composite beams of composite elastomers showed that MLG filling improves the value of the loss factor over a wider frequency range, indicating its potential application as a damping material.

3-2. Experimental Section

3-2-1. Materials

MEO₂MA 95% (1.02 g cm⁻³, 188.22 g mol⁻¹, Sigma-Aldrich) was used as a monomer without purification. The initiator *N,N*-azobisisobutyronitrile (AIBN) (1.1 g cm⁻³, 164.21 g mol⁻¹, Kanto Kagaku) was used without purification. A monodispersed fine silica powder with a particle size of 110 nm (2.221 g cm⁻³, Silibol®110, Fuji Chemical) and multilayer graphene with 25 μm lateral dimensions and 6-8 nm thickness (1.801 g cm⁻³, Tokyo Chemical Industry) were used as the filler to prepare the composite elastomers.

3-2-2. Analytical Techniques

Density measurements were performed with a Micromeritics Instrument Corporation AccuPyc 1330 pycnometer (helium gas, 25 °C). Wide angle X-ray diffraction (WAXD) measurements were taken by an FR-E X-ray diffractometer equipped with a two-dimensional detector R-axis IV (Rigaku) involving an imaging plate (Fujifilm). A beam of 0.3-mm collimated Cu Kα radiation ($\lambda = 0.154$ nm) was used as an X-ray, and the camera length was set at 165 mm. Dielectric property measurements were performed

on a Keysight Technologies E4991B impedance analyzer with 16453A Dielectric Material Test Fixture equipment. The size of the composite elastomer was tailored to $20 \times 20 \times 1 \text{ mm}^3$.

3-2-3. Cross-Sectional Observations

Scanning electron microscopy (SEM) images were obtained with a Hitachi High-Technologies FE-SEM SU8020. To prepare cross-section samples for SEM observation, the composite elastomers underwent an ion polishing treatment using a Gatan Model 693 Precision Ion Polishing System (-160°C , 4 keV, 6 h), and the cross-section samples were sputter-coated with platinum.

3-2-4. Mechanical Properties

The uniaxial tensile tests were carried out using a Shimadzu EZ test (50 mm min^{-1}). The ISO37-4 dumbbell-type test pieces used for the test were prepared by punching the 1 mm thick composite elastomer sheet using a Super Dumbbell Cutter (SDMP-1000-D, DUMBELL).

3-2-5. Electrical Conductivity

The electrical conductivity σ was obtained by the following equation:

$$\sigma = \frac{L}{RS}$$

Here, L , R , and S are the length between electrodes, the volume resistance, and the cross-sectional area of the specimen, respectively. For the specimen of the volume resistance measurement, the composite elastomers were cut into stripes with dimensions of $40 \times 13 \times 1 \text{ mm}^3$. The surfaces of both ends of the short side of the specimen were coated with

silver paste to reduce contact resistance. The volume resistance of the composite elastomer was measured by a Keithley Instruments 2612B under a constant voltage of 10 V.

3-2-6. Thermal Conductivity

The thermal conductivity at 25 °C was obtained by the following equation:

$$\lambda = \alpha \times \rho \times C_p$$

Here, λ , α , ρ , and C_p are the thermal conductivity, thermal diffusivity, density, and specific heat capacity, respectively. The value of α was measured using a NETZSCH LFA-447 by the laser flash method. The ρ measurement was performed with a Micromeritics Instrument Corporation AccuPyc 1330 pycnometer (helium gas, 25 °C). C_p of the composite elastomer was obtained using a NETZSCH DSC 214 Polyma.

3-2-7. Dynamic Mechanical Analysis

Dynamic mechanical analysis (DMA) was conducted on an RSA-G2 solid analyzer (TA instruments) in the rectangular tension geometry. Rectangular samples of 1 mm × 5 mm cross section and approximately 35 mm length were tested at 0.5% strain. Frequency sweep tests (0.01-100 Hz) were conducted from −20 to 60 °C. The master curve was created by shifting the result of frequency sweep tests obtained from different temperatures based on the time–temperature superposition principle.

3-2-8. Vibration Damping Loss Factor Measurement

The damping loss factor was measured according to the central excitation method of JIS K7391 (−20, −10, 0, 10, 20, 30, 40 °C, ~6.4 kHz) and analyzed by using

Brüel & Kjær PULS LabShop. The unconstrained composite beam specimens were prepared by bonding a SPCC steel beam ($250 \times 10 \times 1$ mm) and the elastomer sheets (1 mm thick) using adhesive.

3-3. Results and Discussion

3-3-1. Dispersibility of MLG into MEO₂MA

In this study, three-component suspensions were prepared by adding 0, 1, 3, 6, 12, 18, and 36 vol% silica particles with an average particle size of 110 nm and 0, 1.3, 2.5, 3.8, 5.0, 6.3, and 7.6 vol% MLG to MEO₂MA, which is a liquid monomer, at room temperature. **Figure 3-1a** shows the fluidity of the suspensions after sonication (4 kJ cm⁻³) using an ultrasonic homogenizer. These suspensions were dropped onto a tilted glass plate, and the fluidity of suspensions was evaluated as “Fluid” if it ran in the same manner as the suspension containing only silica particles, “Paste” if it ran slowly, and “Gels” if it did not. The MEO₂MA suspension containing 2.5 vol% MLG was a fluid suspension, but above 3.8 vol%, the fluidity decreased, and the suspension changed to a paste or gel. On the other hand, it was found that the three-component suspension containing the silica particles maintained its fluid state even when a large amount of MLG was added. In particular, the suspensions containing 3~12 vol% silica particles maintained high fluidity even when containing 5.0 vol% MLG (**Figure 3-1b**). After the sonication treatment, MLG in the MEO₂MA settled quickly, whereas the MLG in the three-component suspension containing the silica particles remained dispersed (**Figure 3-1c**). As the amount of silica particles was further increased, the viscosity of the suspension increased, and the suspension gelled with a smaller amount of MLG. In the absence of silica particles, as the amount of MLG in MEO₂MA increased, a network

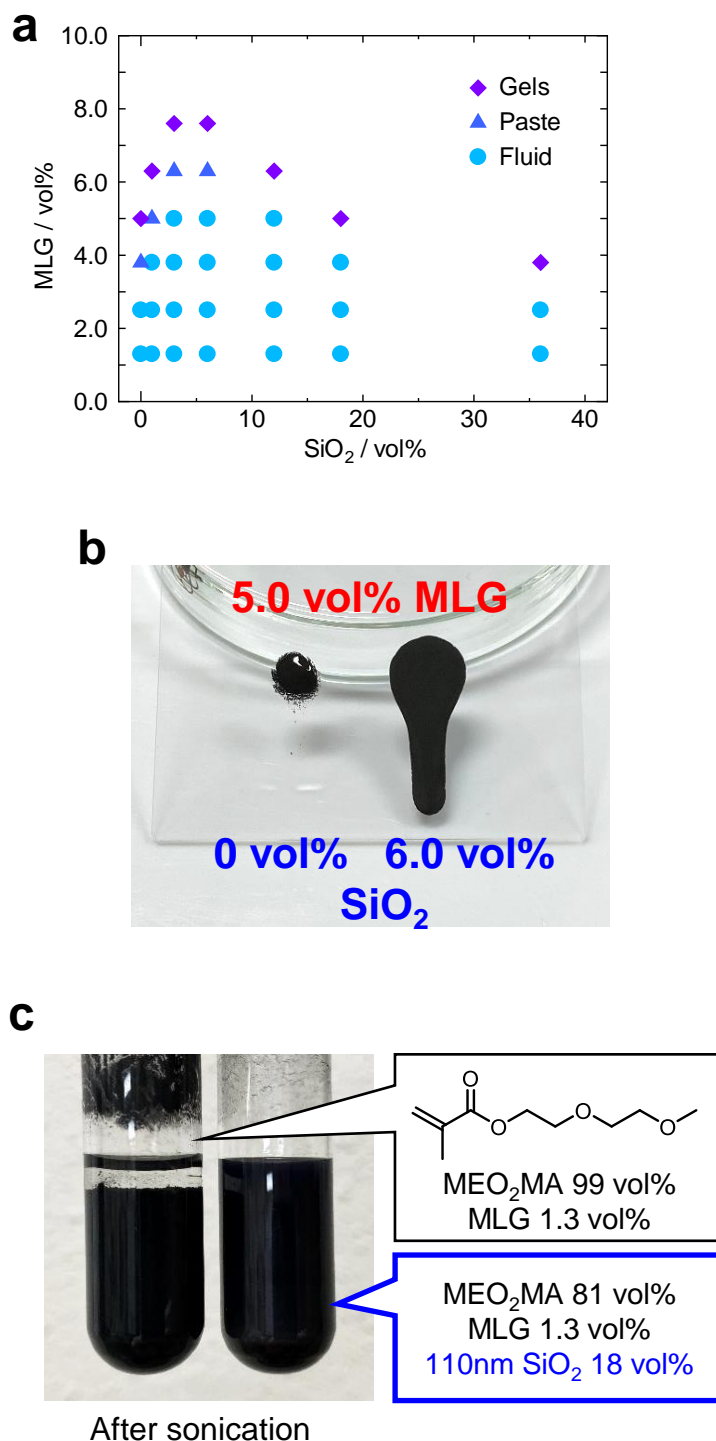


Figure 3-1. Dispersibility of MLG into MEO2MA. (a) State of the three-component suspensions at different amounts of silica particles and MLG. (b) Photograph of the 5.0 vol% MLG suspension and the 6.0 vol% SiO₂ - 5.0 vol% MLG suspension dropped on a tilted glass plate. (c) Photograph of the suspensions containing 1.3 vol% MLG after the sonication treatment.

structure due to aggregation of MLG was expected to form, resulting in reduced fluidity and gelation. In contrast, the presence of silica particles indicates that some effect improved the dispersibility of MLG in MEO₂MA. It should be noted that the total amount of fillers in the suspension was increased, while the fluidity was maintained even with the increased amount of MLG.

3-3-2. Preparation of the Composite Elastomer.

The three-component composite elastomer composed of silica particles, MLG and PMEO₂MA was obtained by adding 0.15 mol% AIBN to MEO₂MA, pouring the suspension into a mold, and undergoing polymerization at 70 °C for 15 hours (**Figure 3-2a**). At this time, the density of PMEO₂MA without the filler was 1.18 g cm⁻³, and the volume shrinkage due to polymerization was calculated to be 13.8%. The volume fractions of the silica particles and those of MLG in each composite elastomer were estimated by assuming that the volume shrinkage of PMEO₂MA was similar in the filler-containing elastomers. The composite elastomers thus obtained showed flexibility and stretchability (**Figure 3-2b**).

To confirm the state of MLG and the silica particles embedded in the composite elastomer, a cross-section of each composite elastomer was prepared by ion polishing and observed by SEM. **Figure 3-3a**, b and c shows cross-sectional SEM images of the composite elastomers with approximately 3 vol% MLG. On these images, the linear shapes are considered to be MLG, and the dots are silica particles. The image of the composite elastomer with 7 vol% silica particles shows that the silica particles are located close to the MLG (**Figure 3-3b**). In the composite elastomer containing 40 vol% silica particles, MLG was fixed in the matrix containing a high concentration of silica particles

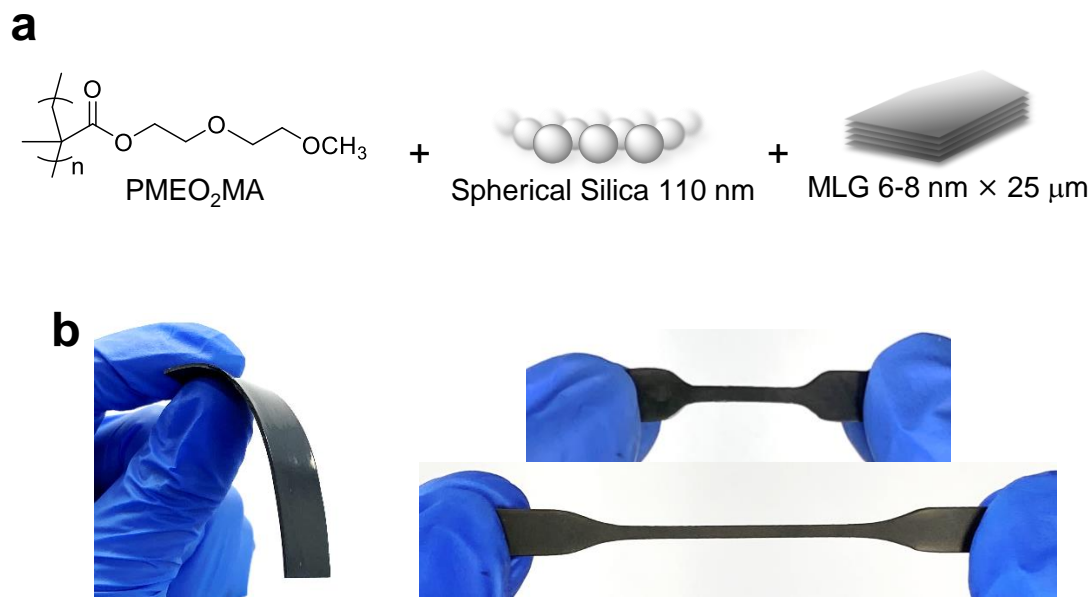


Figure 3-2. Silica particles and MLG embedded in the composite elastomer. (a) Schematic of the material composition. (b) Photograph of the sheet and the dumbbell of the composite elastomer.

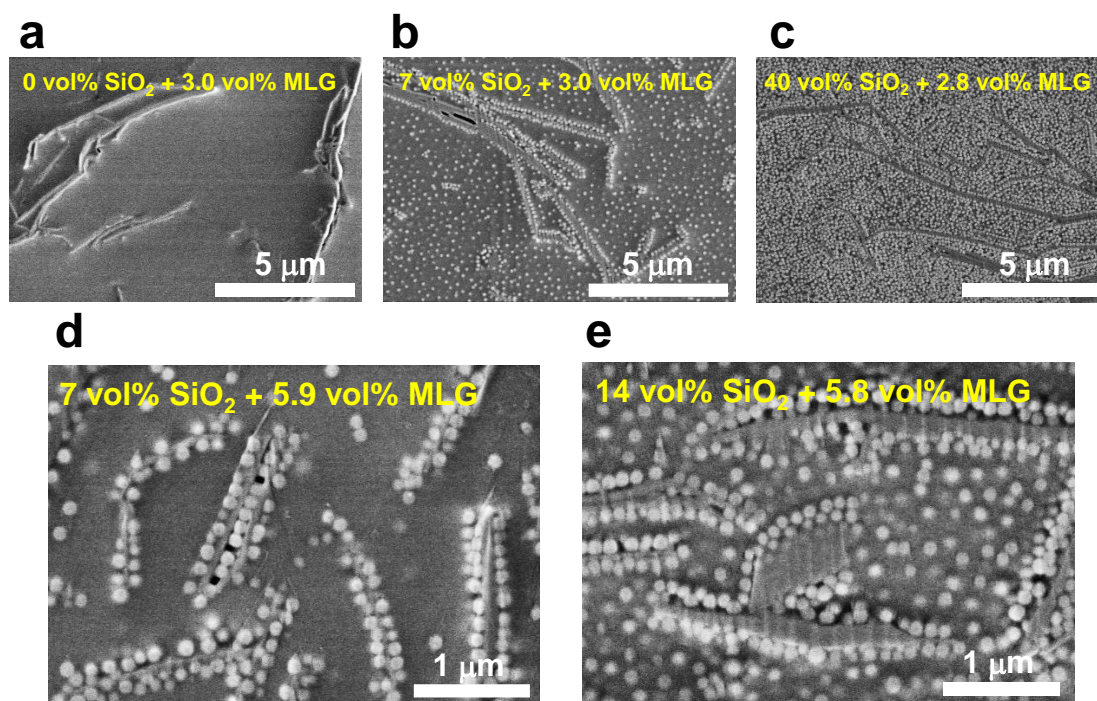


Figure 3-3. (a-e) Cross-sectional SEM images of composite elastomers with different amounts of silica particles and MLG.

(**Figure 3-3c**). High-magnification SEM images of the composite elastomers containing 5.9 and 5.8 vol% MLG revealed that the silica particles not only covered the MLG surface but also intercalated into it (**Figure 3-3d**). In the case of 14 vol% silica particles, more silica particles were gathered on the surface of MLG (**Figure 3-3e**). These images suggested that in MEO₂MA, the silica particles were adsorbed on the surface of MLG with almost no clearance. The reason for the improved dispersibility of MLG in MEO₂MA is thought to be due to the silica particles covering the MLG surface and suppressing its aggregation. As we previously reported, we assume that the silica particles in MEO₂MA are dispersed and stabilized by electrostatic repulsive forces on the particle surface.^[30] Although it is not clear what causes the selective adsorption of silica particles on the MLG surface, it is thought that the electrostatic repulsive force of silica particles contributes to the suppression of aggregation of MLGs and stabilization of dispersion.

Since the intercalation of silica particles between MLG layers was confirmed in the SEM images, the relation between the amount of silica particles and the MLG size was confirmed by WAXD analysis. It is well known that the diffraction of the (002) plane, which originates from the layered structure of MLG, appears at 26.5°.^[9] This peak for the composite elastomer containing approximately 3 vol% MLG decreased as the amount of silica particles increased (**Figure 3-4**). This result suggests that the more silica particles are present, the more uniformly dispersed the MLG is with increasing exfoliation of the layers. When the suspension was sonicated, some of the MLG layers became exfoliated, but they reaggregated due to the strong π – π stacking interaction and van der Waals forces between the two-dimensional sheets. The silica particles were inserted between the layers that were temporarily exfoliated after sonication and are thought to prevent the exfoliated MLGs from approaching each other (**Figure 3-5**). In most of the studies on MLG-based

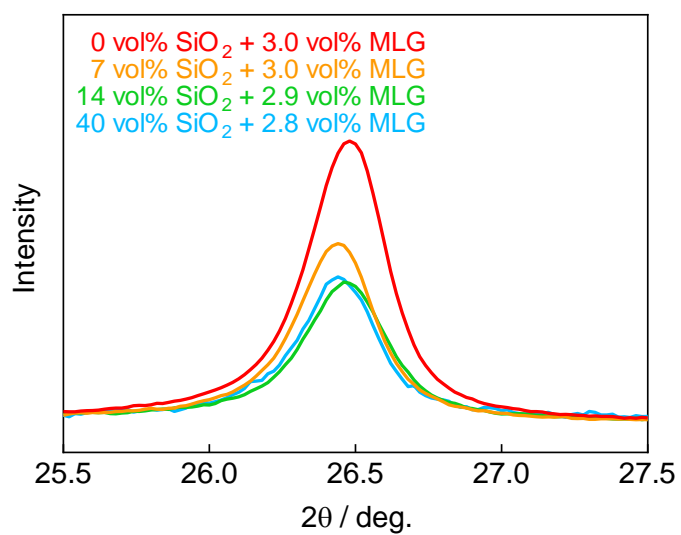


Figure 3-4. WAXD patterns of the composite elastomers containing approximately 3 vol% MLG with different amounts of silica particles.

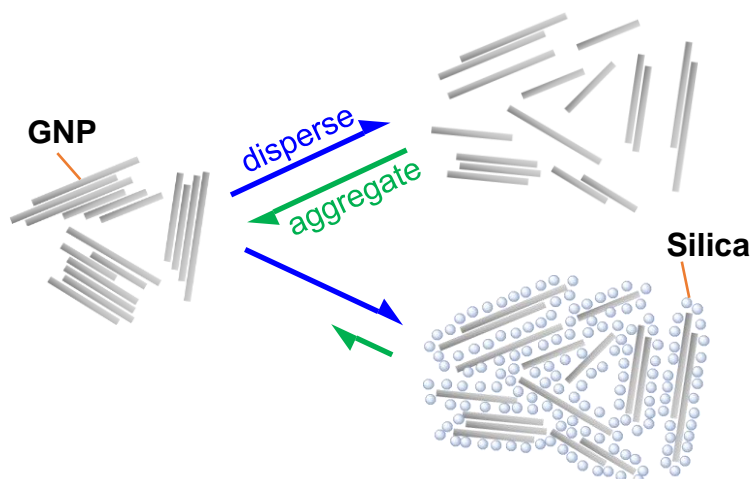


Figure 3-5. Schematic of the dispersibility of MLG with or without silica particles.

composite materials, MLG is dispersed by using large amounts of solvents to prepare these suspensions or by using GOs with better dispersibility. The achievement of layer exfoliation and good dispersibility of MLG without using solvents is noteworthy as a key process for the application of MLG composites in industrial products.

3-3-3. Mechanical Property of the Composite Elastomers.

To verify the effect of MLG filling in composite elastomers, uniaxial tensile tests were conducted. In the uniaxial tensile testing of composite elastomers, the dispersion state of the particles has a significant effect on the mechanical properties, and differences in the dispersion state lead to variations in mechanical property values. To avoid variations in mechanical properties due to changes in the dispersion state of the silica particles and MLG, 40 vol% SiO₂ - 1.5 vol% MLG composite elastomers prepared by varying the sonication energy in advance were evaluated. From these results, it was confirmed that the mechanical properties of the composite elastomers were generally the same after sonication at 4000 J cm⁻³ or higher (**Figure 3-6**). **Figure 3-7** shows the results of uniaxial tensile tests of the composite elastomers containing 0, 7, 14, 21 and 40 vol% silica particles with different amounts of MLG (**Figure 3-8** and **Table 3-1**). The Young's moduli of the composite elastomers without MLG were well correlated with the predictions of the Guth-Gold relation (**Figure 3-7a**). The Young's moduli of elastomers with different amounts of filler can be quantitatively expressed by the Guth-Gold relation based on Einstein's viscosity equation. Assuming that the Young's modulus of filler-filled elastomer is E , the Young's modulus of unfilled elastomer is E_0 , and the volume fraction of filler is ϕ , the Guth-Gold relation is expressed by eq. 1.

$$E = (1 + 2.5\phi + 14.1\phi^2)E_0 \quad (1)$$

It is known that the Young's moduli of many filler-filled elastomers show higher values than the relation shown by the Guth-Gold equation as the amount of filler increases. This is because Einstein's viscosity equation, which is the basis of the Guth-Gold equation, assumes the behavior of monodisperse and agglomerate-free spherical particles in a dispersant. In many filler-filled elastomers, the Young's moduli are usually higher than the theoretical predictions due to the existence of an agglomerative network structure of particles. That is, the aforementioned correlation between the Young's moduli and the Guth-Gold relation suggests that silica particles were almost monodispersed in the composite elastomers. On the other hand, the Young's moduli of the composite elastomers containing MLG were higher than predicted by the Guth-Gold relation as the amount of MLG increased. Fukahori et al. explained that the Young's moduli of reinforced rubbers become higher than predicted by the Guth-Gold relation when there is a filler aggregation network parallel to the elongation direction and proposed a modified Guth-Gold equation that takes into account the anisotropy of the fillers.^[31] The drastic increase in Young's modulus with increasing MLG might be attributed to the partial aggregation of MLG and the nonspherical filler shape with a high aspect ratio.

The fracture energy, an index of toughness of the composite elastomer, increased with increasing amounts of silica particles (**Figure 3-7b**). Up to 14 vol% silica particles, the fracture energy tended to increase with increasing MLG content. On the other hand, the fracture energy of the samples with more than 21 vol% silica particles either did not change much or decreased with increasing MLG content. The stress and strain at break of the composite elastomer with a large amount of silica particles tend to decrease significantly with increasing MLG, resulting in lower fracture energy values (**Figure 3-7c** and **Figure 3-7d**). As the total amount of filler increases, the resistance and frictional

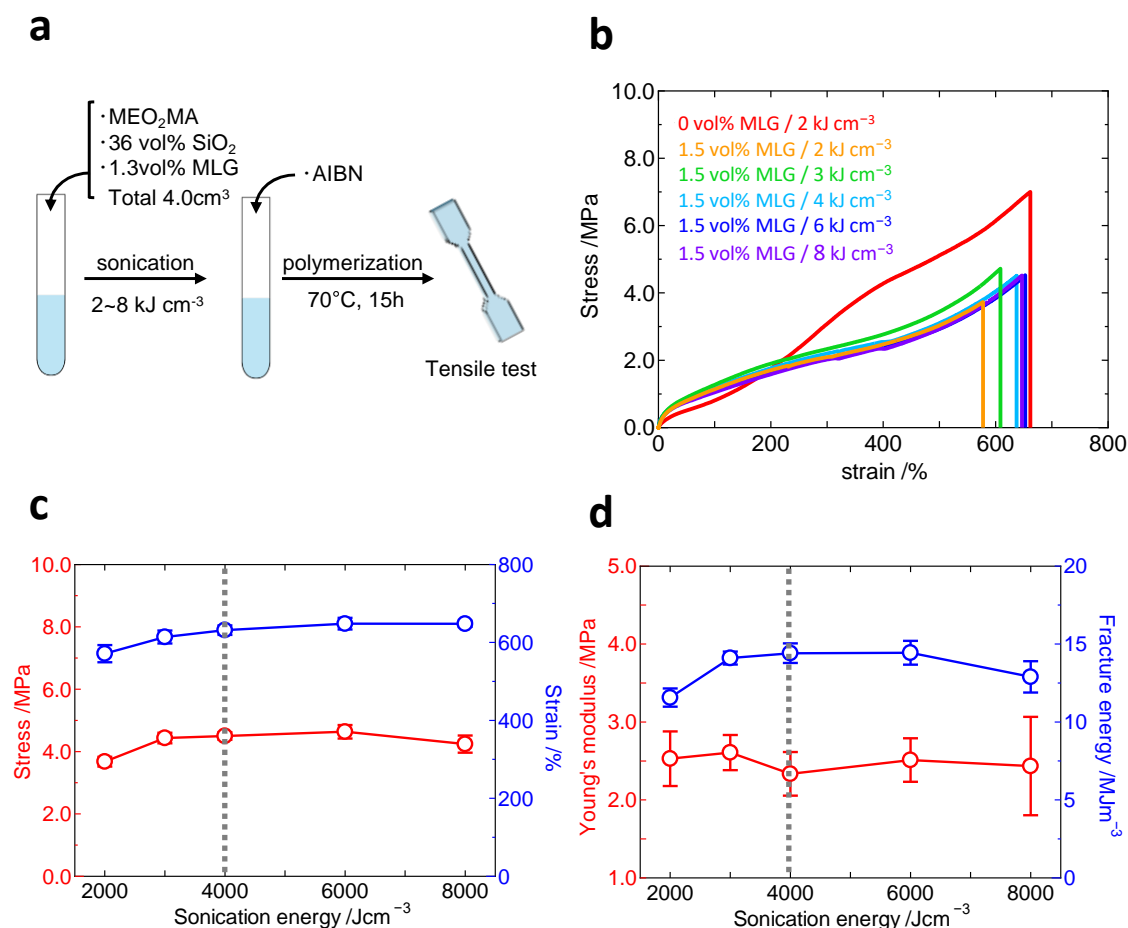


Figure 3-6. Examination of sonication processing energy for dispersing fillers (a) Schematic illustration of the examination procedure. (b) Strain-stress curves of the composite elastomers to which different values of processing energy were applied. (c) Stress and strain at break at different values of processing energy. (d) Young's modulus and fracture energy at different values of processing energy.

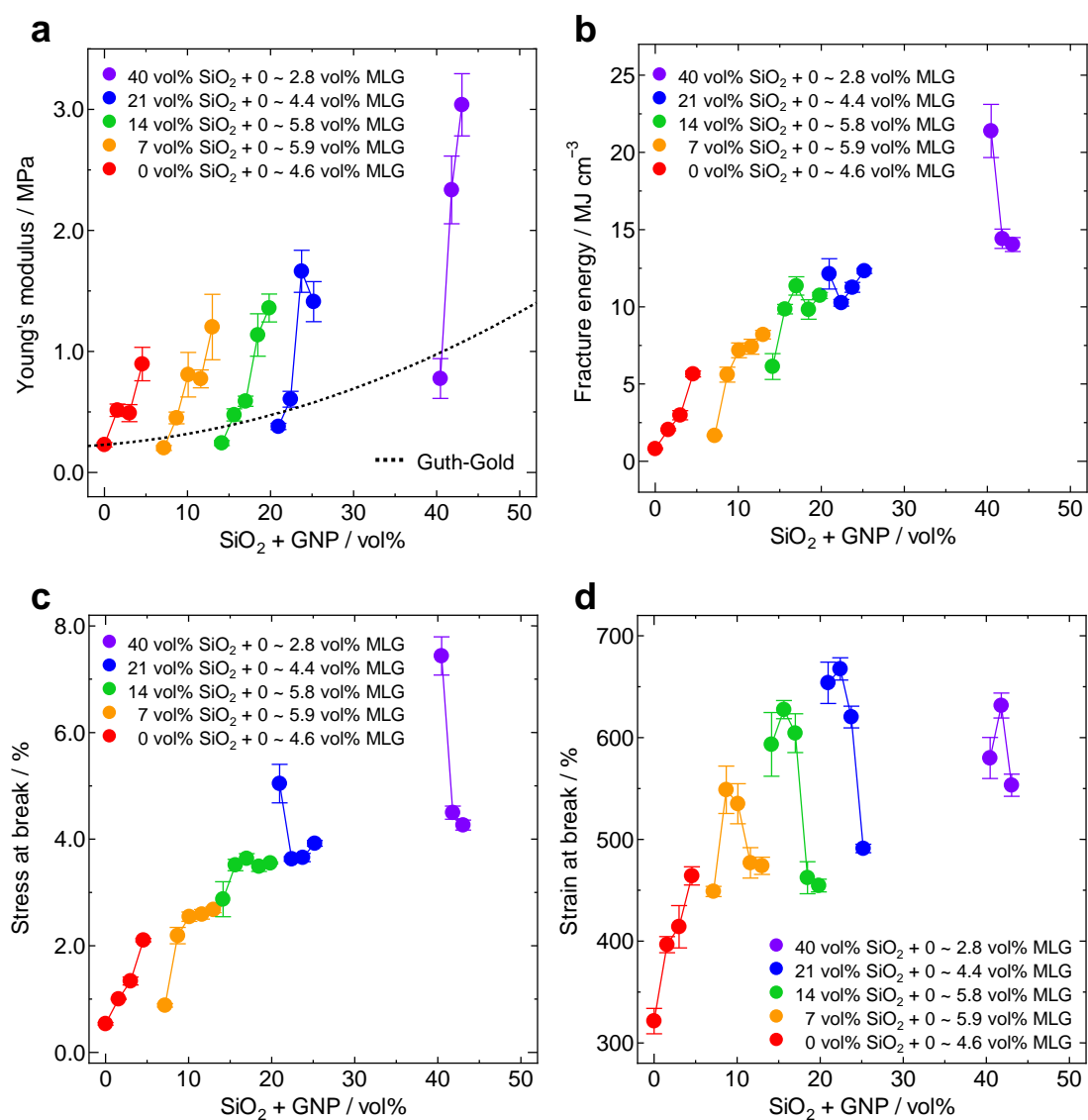


Figure 3-7. Mechanical properties of the composite elastomers containing various amounts of silica particles and MLG. (a) Young's moduli at different filler amounts. The dotted line shows the correlation between Young's moduli and filler amounts expected from the Guth-Gold relation. (b) Fracture energy at different filler amounts. (c) Stress at break at different filler amounts. (d) Strain at break at different filler amounts.

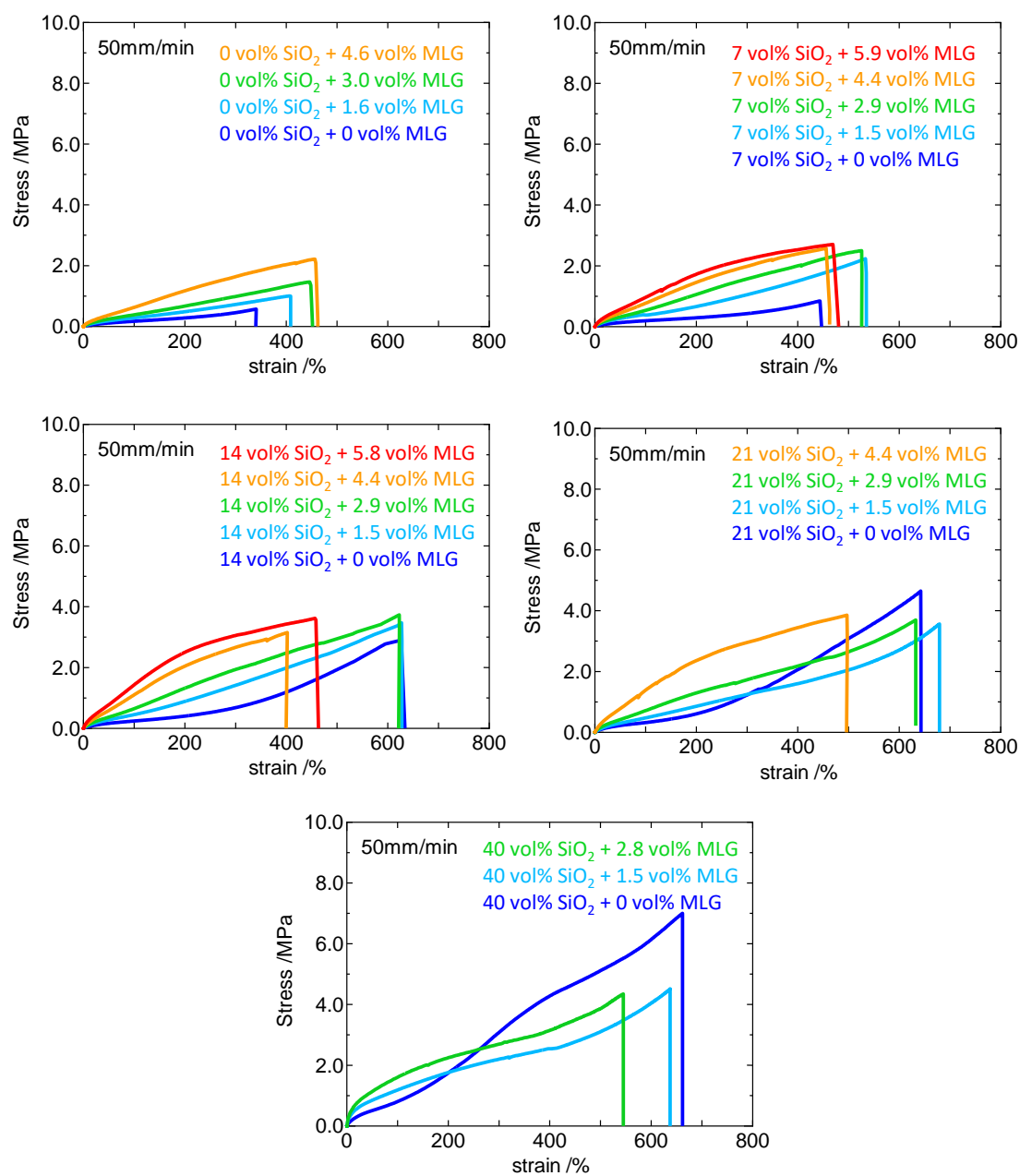


Figure 3-8. Stress-strain curves of the composite elastomers

Table 3-1. The mechanical properties of the composite elastomers.

| ϕ_S [vol%] | ϕ_G [vol%] | E [MPa] | σ_f [MPa] | ε_f [%] | Γ [MJ m ⁻³] |
|--------------------|--------------------|--------------|---------------------|------------------------|-----------------------------------|
| 0 | 0.0 | 0.23 ± 0.02 | 0.54 ± 0.03 | 321 ± 12 | 0.8 ± 0.1 |
| 0 | 1.6 | 0.51 ± 0.05 | 1.00 ± 0.01 | 397 ± 8 | 2.0 ± 0.1 |
| 0 | 3.0 | 0.49 ± 0.07 | 1.34 ± 0.07 | 414 ± 21 | 3.0 ± 0.3 |
| 0 | 4.6 | 0.90 ± 0.14 | 2.11 ± 0.03 | 464 ± 9 | 5.7 ± 0.2 |
| 7 | 0.0 | 0.20 ± 0.02 | 0.88 ± 0.03 | 449 ± 5 | 1.7 ± 0.0 |
| 7 | 1.5 | 0.45 ± 0.05 | 2.19 ± 0.15 | 549 ± 23 | 5.6 ± 0.5 |
| 7 | 3.0 | 0.81 ± 0.18 | 2.55 ± 0.09 | 535 ± 20 | 7.2 ± 0.5 |
| 7 | 4.5 | 0.77 ± 0.07 | 2.59 ± 0.09 | 477 ± 15 | 7.4 ± 0.5 |
| 7 | 5.9 | 1.20 ± 0.27 | 2.68 ± 0.05 | 474 ± 8 | 8.2 ± 0.3 |
| 14 | 0.0 | 0.24 ± 0.02 | 2.87 ± 0.33 | 593 ± 31 | 6.1 ± 0.8 |
| 14 | 1.5 | 0.48 ± 0.05 | 3.52 ± 0.11 | 628 ± 9 | 9.9 ± 0.3 |
| 14 | 2.9 | 0.59 ± 0.04 | 3.64 ± 0.09 | 604 ± 19 | 11.4 ± 0.6 |
| 14 | 4.4 | 1.14 ± 0.18 | 3.49 ± 0.09 | 462 ± 16 | 9.8 ± 0.6 |
| 14 | 5.8 | 1.36 ± 0.12 | 3.55 ± 0.02 | 455 ± 6 | 10.7 ± 0.2 |
| 21 | 0.0 | 0.38 ± 0.03 | 5.04 ± 0.36 | 654 ± 20 | 12.1 ± 1.0 |
| 21 | 1.5 | 0.61 ± 0.07 | 3.63 ± 0.04 | 667 ± 11 | 10.3 ± 0.2 |
| 21 | 2.9 | 1.66 ± 0.17 | 3.66 ± 0.08 | 620 ± 11 | 11.3 ± 0.3 |
| 21 | 4.4 | 1.41 ± 0.17 | 3.92 ± 0.05 | 491 ± 4 | 12.3 ± 0.2 |
| 40 | 0.0 | 0.78 ± 0.16 | 7.44 ± 0.36 | 580 ± 20 | 21.4 ± 1.7 |
| 40 | 1.5 | 2.33 ± 0.28 | 4.50 ± 0.12 | 632 ± 12 | 14.4 ± 0.6 |
| 40 | 2.8 | 3.04 ± 0.26 | 4.26 ± 0.09 | 553 ± 11 | 14.0 ± 0.5 |

ϕ_S :SiO₂ fraction in the composite elastomer, ϕ_G :MLG fraction in the composite elastomer, E :Young's modulus, σ_f :Stress at break, ε_f :Strain at break, Γ :Fracture energy

forces generated when the MLG rotates its orientation with respect to the matrix deformation increase, and the stress concentration near the MLG is considered to be the trigger of the fracture.

3-3-4. Electrical Properties of the Composite Elastomer

Graphene has been one of the key components in recent research on conductive composite materials due to its extremely high electrical conductivity ($\sim 6,000 \text{ S m}^{-1}$).^[13] Several conductive MLG composite materials have been reported, and conductive soft materials are attracting attention as materials with potential for practical applications such as sensing.^[20,22] We expected that the composite elastomer containing MLG in this study would also exhibit a significant improvement in electrical conductivity.

The results of electrical conductivity measurements for the composite elastomers with different amounts of silica particles and MLG are shown in **Figure 3-9a**. For the composite elastomer without silica particles, a sharp increase in electrical conductivity was observed with the increase in MLG. The suspension before undergoing polymerization of the 0 vol% SiO₂ - 4.6 vol% MLG composite elastomer had low fluidity, as shown in **Figure 3-1a**. The increase in electrical conductivity of the composite elastomer and the decrease in the fluidity of the suspension suggest that this MLG amount was near the percolation threshold. Then, the electrical conductivity of the composite elastomers containing silica particles was measured, but the electrical conductivity decreased as the amount of silica particles increased. Since we confirmed that the addition of silica particles improves the dispersibility of MLG, we expected to lower the percolation threshold and increase the electrical conductivity due to the improved dispersibility. This completely opposite result to the expectation suggests that the

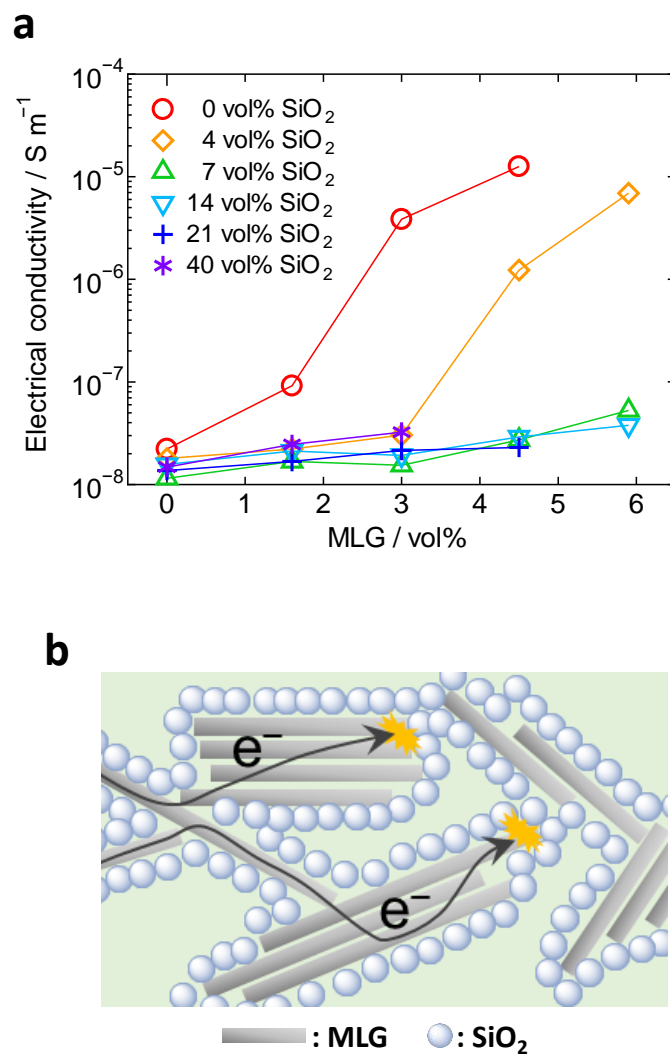


Figure 3-9. Electrical characteristics of the composite elastomers. (a) Electrical conductivity of the composite elastomers at different filler amounts. (b) Schematic of the interrupted conductive path at the silica particles absorbed on MLG.

insulating silica particles almost completely covered the MLG surface. In other words, the conductive path that should have been formed by MLGs might be interrupted by the silica particles (**Figure 3-9b**).

Here, we predicted that the layered structure formed by insulators and conductors (in this case, silica particles and MLGs) would have some effect on the dielectric properties. Therefore, the relative dielectric constant (ϵ) and dielectric loss tangent ($\tan\delta$) of each composite elastomer were measured. For the composite elastomers without silica particles, both ϵ and $\tan\delta$ increased with increasing MLG content (**Figure 3-10a**). On the other hand, the $\tan\delta$ value of the composite elastomer containing silica particles did not change significantly, but the increase in ϵ was caused by increasing the amount of MLG (**Figure 3-10b, c and d**). **Figure 3-10e** shows ϵ and $\tan\delta$ of the composite elastomers at 10 MHz. For the composite elastomer without silica particles, both ϵ and $\tan\delta$ increased significantly, whereas for the composite elastomer with silica particles, the change in $\tan\delta$ was very small compared to the increase in ϵ . When silica particles were 14 vol% or more, the increase in $\tan\delta$ with respect to MLG addition was smaller, and the ϵ and $\tan\delta$ values of the 14 vol% SiO₂ - 5.8 vol% MLG composite elastomer at 10 MHz were 12.6 and 0.045, respectively. This is expected because the MLG is covered with silica particles, which greatly suppresses the dielectric loss caused by the polymer molecule at the MLG-polymer interface. The characteristic morphology formed by the silica particles and MLG in the composite elastomer shows that both high ϵ and low $\tan\delta$ can be achieved. Materials with both high ϵ and low $\tan\delta$ are required for the miniaturization and high performance of antennas, and the characteristics of this composite elastomer are expected to be applied to these applications.^[32]

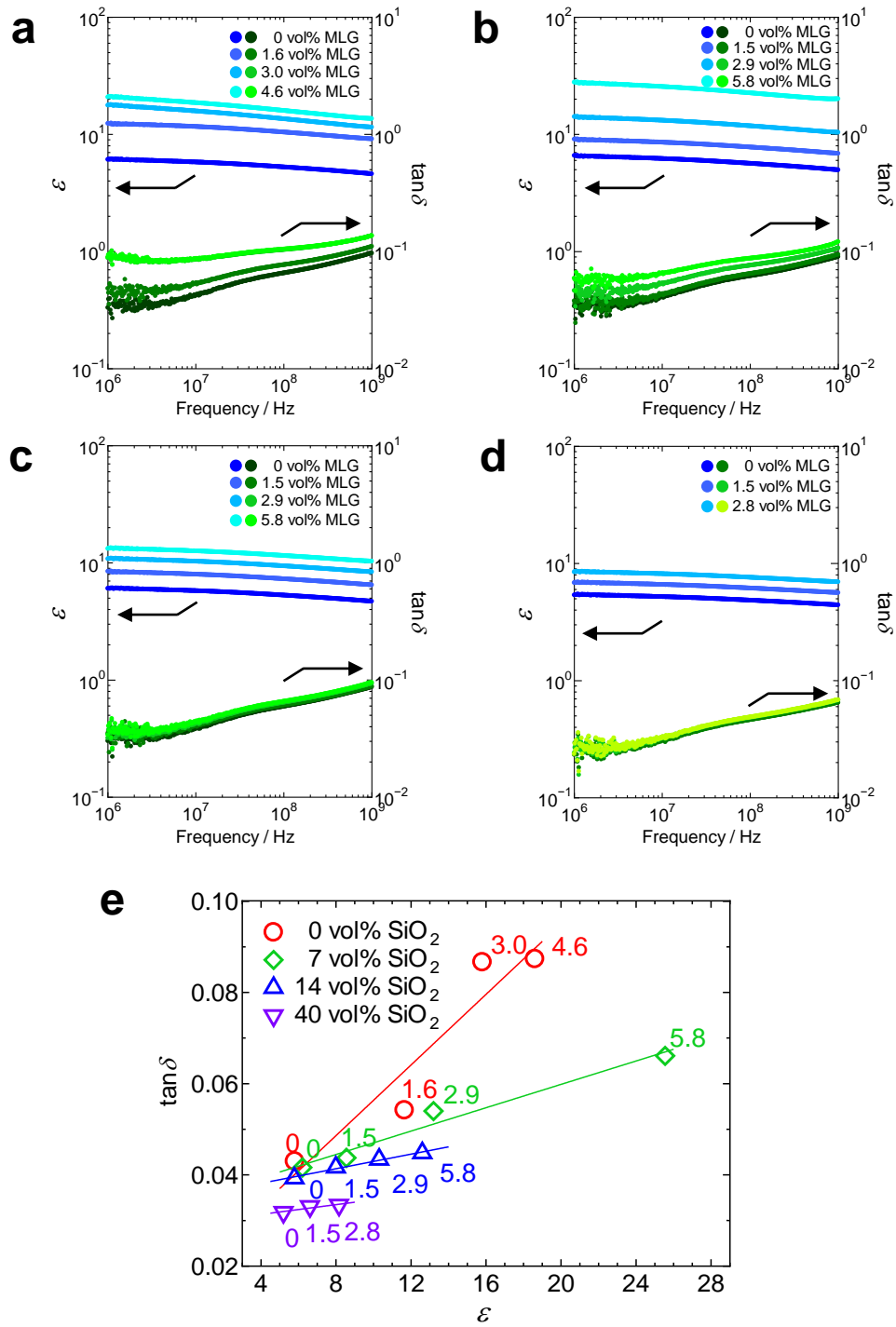


Figure 3-10. (a) The ϵ and $\tan \delta$ values of the composite elastomer without silica particles. (b) The ϵ and $\tan \delta$ values of the composite elastomer containing 7 vol% silica particles. (c) The ϵ and $\tan \delta$ values of the composite elastomer containing 14 vol% silica particles. (d) The ϵ and $\tan \delta$ values of the composite elastomer containing 40 vol% silica particles. (e) Relation between ϵ and $\tan \delta$ at 10 MHz. The values above each data point indicate the volume fraction of MLG in the composite elastomers.

3-3-5. Thermal Conductivity of the Composite Elastomer.

Graphene has outstanding thermal conductivity ($5,000 \text{ W m}^{-1} \text{ K}^{-1}$),^[13] and the development of thermally conductive composite materials based on this property was previously reported. In recent years, thermal management has become increasingly important due to the increasing heat generation caused by the high density and frequency of integrated circuits (ICs) and the rapid miniaturization of electronic devices.^[33–35] Thermal conductive materials based on polymer composites with easy formability have a very important role in thermal management in narrow spaces.

From this perspective, the thermal conductivity of the composite elastomers was evaluated. **Figure 3-11a** shows the thermal conductivity of an approximately 3 vol% MLG composite elastomer with different amounts of silica particles. A decrease in thermal conductivity was observed for the composite elastomer with 7 vol% silica particles, but a slight increase in the value was observed with increasing amounts of silica particles. The lattice vibration (phonon), which affects the thermal conductivity, is considered to correspond to conduction mainly through the MLG network. It is expected that the thermal conductivity decreased in the composite elastomer with 7 vol% silica particles because the presence of silica particles interferes with the excellent phonon conduction of MLG. Since the thermal conductivity of inorganic silica particles is lower than that of MLG but better than that of the matrix polymer, it is likely that the thermal conductivity increased with increasing amounts of silica particles. The thermal conductivity of the composite elastomer increased with increasing amounts of MLG (**Figure 3-11b**). The thermal conductivity of the composite elastomer with 14 vol% silica particles, which could be filled with the highest amount of MLG, showed a linear relation with the amount of MLG. The value of the 14 vol% SiO₂ - 5.8 vol% MLG composite

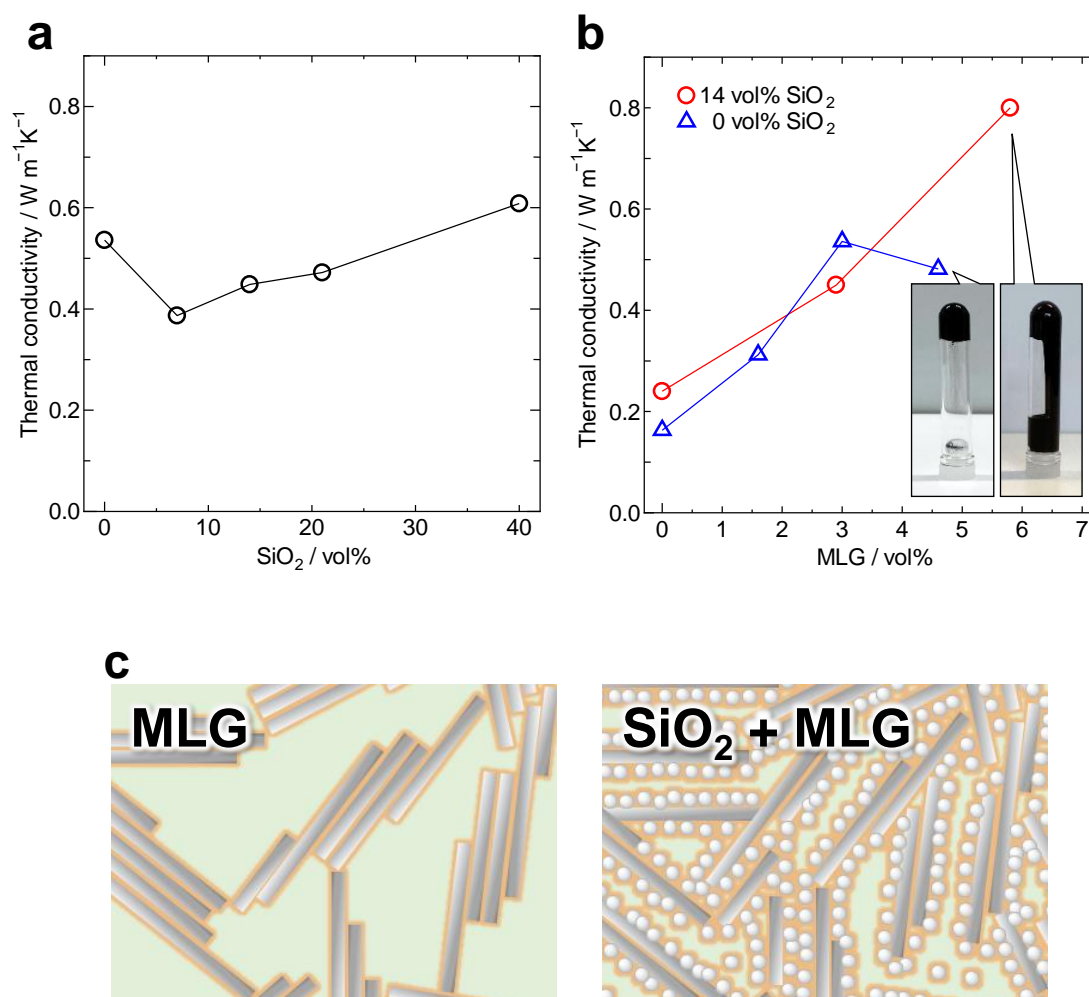


Figure3-11. Thermal conductivity of the composite elastomers. (a) Thermal conductivity of the composite elastomers containing approximately 3 vol% MLG with different amounts of silica particles. (b) Thermal conductivity of the 14 vol% SiO₂-MLG composite elastomer and the MLG composite elastomer without silica particles. The insets are photographs showing the fluidity of the suspensions before polymerization. (c) Schematic of the state of dispersed MLG in the composite elastomers (left) without silica particles and (right) with silica particles.

elastomer was $0.8 \text{ W m}^{-1} \text{ K}^{-1}$, and the suspension before polymerization showed good fluidity (see the inset of **Figure 3-11b**). On the other hand, the thermal conductivity of the composite elastomer without silica particles increased with increasing MLG amount, but the increase leveled off at 4.6 vol%. The suspension without silica particles before polymerization at this volume fraction of MLG was gel-like and had almost lost its fluidity. This suggests that the MLG in the MEO₂MA suspension started to form an aggregation network. In other words, the MLG aggregated as its amount increased, and it was inferred that phonon propagation became localized and the thermal conductivity of the bulk material decreased. The better dispersion of MLG in the presence of silica particles and the effect of phonon conduction through silica particles are considered to be responsible for the thermal conductivity (**Figure 3-11c**). The suspension containing these fillers with better fluidity can be polymerized by heating, which means that the suspension can be cured after filling or coating. This processing characteristic is suitable for applications such as potting agents for electronic device sealing and functional adhesives and is expected to be applied as new thermally conductive soft materials.^[36–38]

3-3-6. Dynamic mechanical properties of the Composite Elastomer

DMA measurements were performed to clarify the viscoelasticity of the MLG composite elastomer. Based on the DMA results of the frequency sweep test obtained at each temperature, a master curve was prepared according to the time-temperature superposition principle using the William-Landel-Ferry shift factor α_T obtained from eq. 2^[39]:

$$\log(\alpha_T) = \frac{-C_1(T - T_r)}{C_2 + (T - T_r)} \quad (2)$$

where T is the measurement temperature and C_1 , C_2 , and T_r were taken as 8.86, 101.6,

and 5 °C, respectively. For the composite elastomers with a small amount of silica particles (0 or 7 vol% silica particles), the change in storage modulus (E') and loss modulus (E'') due to MLG filling was slight (**Figure 3-12a, b, c and d**). In contrast, for the 40 vol% SiO₂ composite elastomers, E' and E'' sifted significantly with MLG filling (**Figure 3-12e and f**). The changes in E' and E'' due to filling the composite elastomer containing 40 vol% silica particles with 2.8 vol% MLG were comparable to those obtained when the amount of silica particles in PMEO₂MA was increased from 0 to 40 vol%. When the composite elastomer containing a high concentration of silica particles was deformed, a large resistance force caused by the plate-like MLG might affect the increase in E' , and a large friction force between the MLG surface and the silica particles was presumed to affect the increase in E'' .

The friction induced by fillers such as silica particles and MLG dissipates the deformation energy as thermal energy and gives the composite soft material vibration-damping properties.^[40–42] Then, the vibration-damping properties of the composite elastomer were evaluated. An unconstrained composite beam was fabricated by attaching the composite elastomer to a steel beam (**Figure 3-13a**), and the loss factor of the composite beam obtained from the frequency response function when the center of this specimen was vibrated was compared.^[43] The loss factor was obtained from eq. 3 using the peak position f of the anti-resonance point of the frequency response function and the half-width Δf at position 3 dB down from the peak maximum value.^[44,45]

$$\eta = \frac{\Delta f}{f} \quad (3)$$

The measurements were taken at -20, -10, 0, 10, 20, 30 and 40 °C, and the anti-resonance peaks from the second to the seventh order were used for analysis (**Figure 3-13b and c**). Based on the loss factor of the composite beams obtained at each temperature,

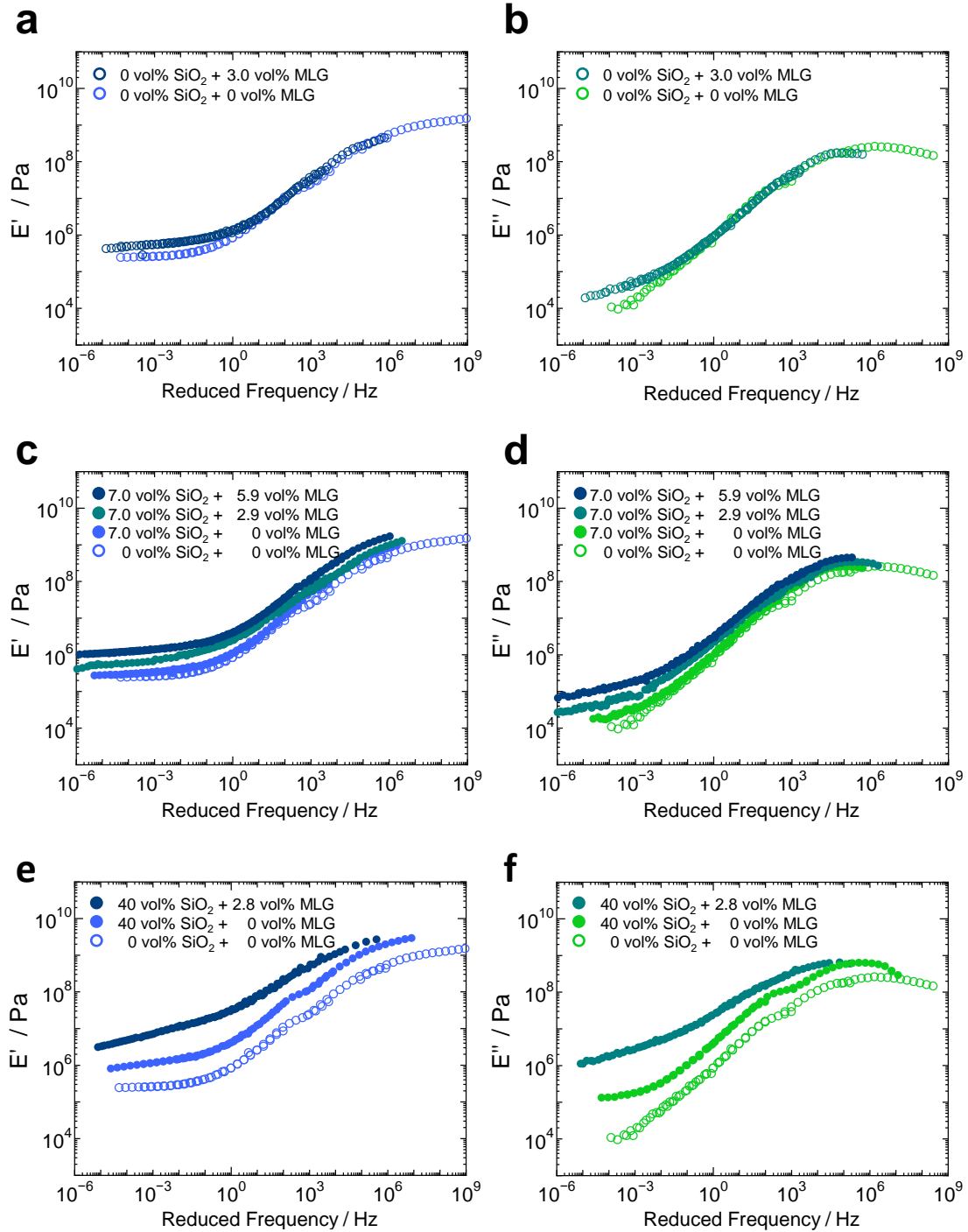


Figure 3-12. Viscoelasticity of the composite elastomers. (a and b) E' and E'' of the composite elastomers without silica particles. (c and d) E' and E'' of the composite elastomer containing 7 vol% silica particles. (e and f) E' and E'' of the composite elastomer containing 40 vol% silica particles.

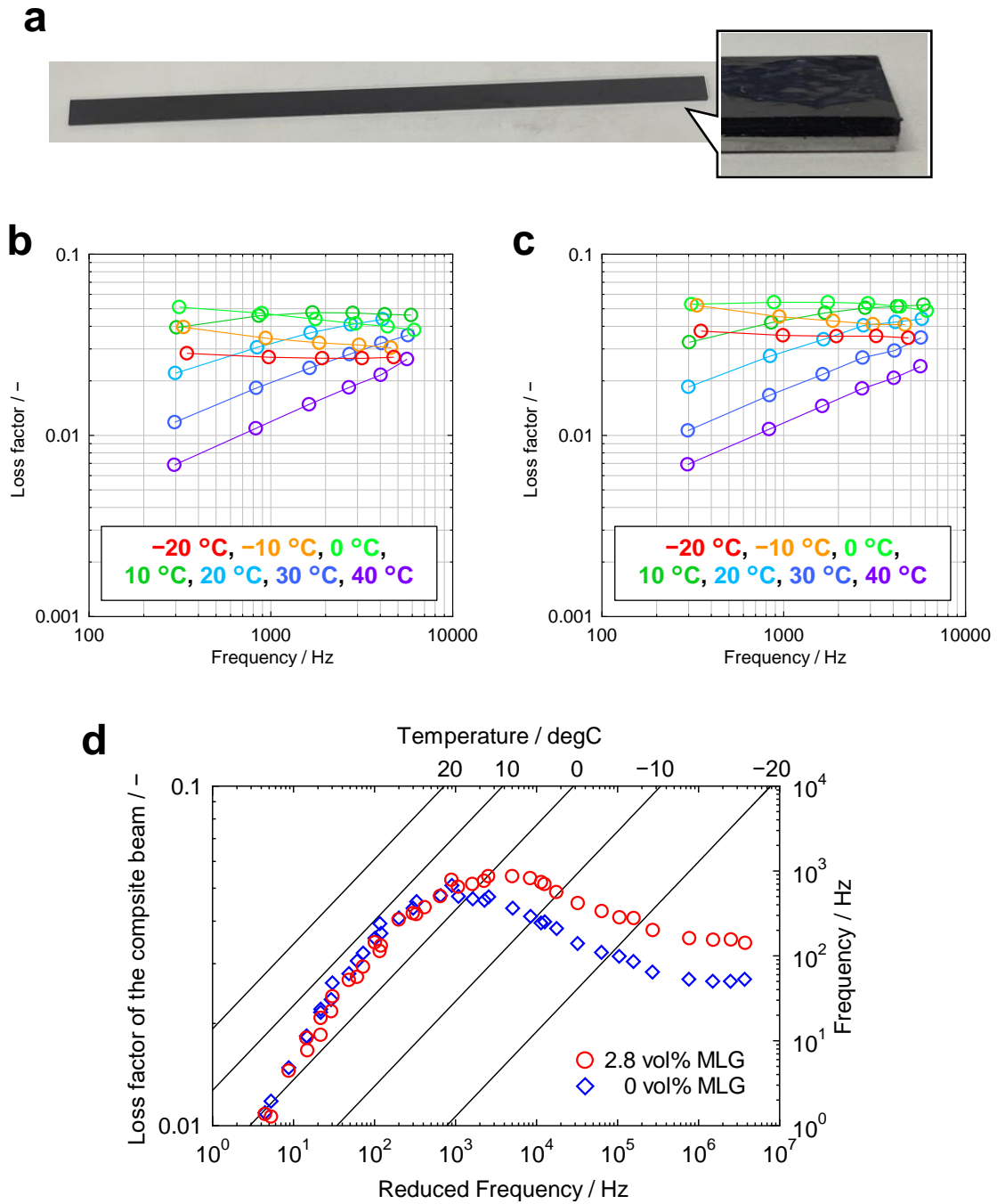


Figure 3-13. The loss factor of the unconstrained composite beam with the composite elastomer. (a) Photograph of the unconstrained composite beam with the composite elastomer for measuring the loss factor. (b) The loss factor of the unconstrained composite beam with the 40 vol% SiO₂ - 0 vol% MLG composite elastomer. (c) The loss factor of the unconstrained composite beam with the 40 vol% SiO₂ - 2.8 vol% MLG composite elastomer. (d) Nomogram prepared from the loss factor of the composite beam with the composite elastomers.

a nomogram was created using α_T obtained from eq. 2 (**Figure 3-13d**). The loss factor of the 40 vol% SiO₂ - 2.8 vol% MLG composite elastomer was higher in the high frequency region than that of the composite elastomer without MLG. The higher value of the loss factor and the broadening of the peak shape with respect to frequency indicate improved vibration damping performance over a wider range of frequencies (i.e., temperatures). The reason for the small difference in the loss factor at low frequencies in the presence of MLG might be that the elastic modulus of the matrix polymer decreases at low frequencies (i.e., high temperatures), and the frictional force between the filler and polymer decreases due to the lower viscosity. This result shows that a small amount of MLG filling can improve the vibration damping performance of the composite elastomers.

3-4. Conclusions

A three-component composite elastomer consisting of PMEO₂MA, silica particles and MLG was fabricated, and the various functions brought about by the characteristic morphology formed by the silica particles and MLG were evaluated. The silica particles significantly improved the dispersibility of MLG into MEO₂MA, allowing more MLG to be loaded. In addition, the suspensions filled with silica particles and MLG showed higher fluidity than the suspensions without silica particles, even when the amount of MLG was higher. Although the composite elastomer did not show the initially expected improvement in electrical conductivity, it was found that ε could be increased while suppressing the increase in $\tan\delta$. The composite elastomer showed higher thermal conductivity due to the presence of silica particles, which allowed for a higher volume fraction of MLG to be filled. The dynamic viscoelasticity analysis of the composite elastomers showed that the filling effect of MLG was more remarkable in the composite

elastomer containing 40 vol% silica particles. The results of the loss factor measurements showed that the 40 vol% - 2.8 vol% MLG composite elastomer maintained a higher value over a wider frequency range than that without MLG. These results, which showed a method to fabricate functional composite elastomers from lower-cost materials under mild, solvent-free conditions, are expected to contribute to the development of new soft materials for practical use.

References

- [1] K. S. Novoselov, A. K. Geim, S. V. Morozov, D. Jiang, Y. Zhang, S. V. Dubonos, I. V. Grigorieva, A. A. Firsov, *Science* (80-.). **2004**, 306, 666.
- [2] A. K. Geim, K. S. Novoselov, *Nat. Mater.* **2007**, 6, 183.
- [3] V. Singh, D. Joung, L. Zhai, S. Das, S. I. Khondaker, S. Seal, *Prog. Mater. Sci.* **2011**, 56, 1178.
- [4] C. Lee, X. Wei, J. W. Kysar, J. Hone, *Science* (80-.). **2008**, 321, 385.
- [5] J. S. Bunch, S. S. Verbridge, J. S. Alden, A. M. Van Der Zande, J. M. Parpia, H. G. Craighead, P. L. McEuen, *Nano Lett.* **2008**, 8, 2458.
- [6] V. Berry, *Carbon N. Y.* **2013**, 62, 1.
- [7] A. A. Balandin, S. Ghosh, W. Bao, I. Calizo, D. Teweldebrhan, F. Miao, C. N. Lau, *Nano Lett.* **2008**, 8, 902.
- [8] A. Yu, P. Ramesh, M. E. Itkis, E. Bekyarova, R. C. Haddon, *J. Phys. Chem. C* **2007**, 111, 7565.
- [9] S. Araby, Q. Meng, L. Zhang, H. Kang, P. Majewski, Y. Tang, J. Ma, *Polymer (Guildf)*. **2014**, 55, 201.
- [10] H. Liu, Y. Li, K. Dai, G. Zheng, C. Liu, C. Shen, X. Yan, J. Guo, Z. Guo, *J.*

- Mater. Chem. C* **2015**, *4*, 157.
- [11] J. Chen, B. Liu, X. Gao, *Results Phys.* **2020**, *16*, 102974.
- [12] A. Caradonna, G. Colucci, M. Giorcelli, A. Frache, C. Badini, *J. Appl. Polym. Sci.* **2017**, *134*, DOI 10.1002/app.44814.
- [13] H. Kim, A. A. Abdala, C. W. Macosko, *Macromolecules* **2010**, *43*, 6515.
- [14] A. Bianco, H. M. Cheng, T. Enoki, Y. Gogotsi, R. H. Hurt, N. Koratkar, T. Kyotani, M. Monthieux, C. R. Park, J. M. D. Tascon, J. Zhang, *Carbon N. Y.* **2013**, *65*, 1.
- [15] B. Mensah, K. C. Gupta, H. Kim, W. Wang, K. U. Jeong, C. Nah, *Polym. Test.* **2018**, *68*, 160.
- [16] D. R. Dreyer, S. Park, C. W. Bielawski, R. S. Ruoff, *Chem. Soc. Rev.* **2010**, *39*, 228.
- [17] D. Frasca, D. Schulze, V. Wachtendorf, C. Huth, B. Schartel, *Eur. Polym. J.* **2015**, *71*, 99.
- [18] D. G. Papageorgiou, I. A. Kinloch, R. J. Young, *Carbon N. Y.* **2015**, *95*, 460.
- [19] E. Aram, M. Ehsani, H. A. Khonakdar, S. Abdollahi, *J. Thermoplast. Compos. Mater.* **2019**, *32*, 1176.
- [20] M. Hébert, J. P. Huissoon, C. L. Ren, *Sensors Actuators, A Phys.* **2020**, *305*, 111917.
- [21] P. Costa, S. Gonçalves, H. Mora, S. A. C. Carabineiro, J. C. Viana, S. Lanceros-Mendez, *ACS Appl. Mater. Interfaces* **2019**, *11*, 46286.
- [22] K. Ke, M. McMaster, W. Christopherson, K. D. Singer, I. Manas-Zloczower, *Compos. Part A Appl. Sci. Manuf.* **2019**, *126*, 105614.
- [23] R. Yang, Y. Yao, Z. Duan, Z. Yuan, H. Tai, Y. Jiang, Y. Zheng, D. Wang,

- Langmuir* **2020**, *36*, 3029.
- [24] K. K. Sadasivuni, D. Ponnammma, S. Thomas, Y. Grohens, *Prog. Polym. Sci.* **2014**, *39*, 749.
- [25] A. G. D'Aloia, F. Marra, A. Tamburrano, G. De Bellis, M. S. Sarto, *Carbon N. Y.* **2014**, *73*, 175.
- [26] S. Maiti, B. B. Khatua, *Polym. Compos.* **2016**, *37*, 2058.
- [27] C. Chen, Y. Tan, X. Han, H. Luo, S. Zeng, S. Peng, H. Zhang, *J. Eur. Ceram. Soc.* **2018**, *38*, 5615.
- [28] M. Zahid, Y. Nawab, N. Gulzar, Z. A. Rehan, M. F. Shakir, A. Afzal, I. Abdul Rashid, A. Tariq, *J. Mater. Sci. Mater. Electron.* **2020**, *31*, 967.
- [29] I. Chakraborty, K. J. Bodurtha, N. J. Heeder, M. P. Godfrin, A. Tripathi, R. H. Hurt, A. Shukla, A. Bose, *ACS Appl. Mater. Interfaces* **2014**, *6*, 16472.
- [30] K. Watanabe, E. Miwa, F. Asai, T. Seki, K. Urayama, T. Nakatani, S. Fujinami, T. Hoshino, M. Takata, C. Liu, K. Mayumi, K. Ito, Y. Takeoka, *ACS Mater. Lett.* **2020**, *2*, 325.
- [31] Y. Fukahori, A. A. Hon, V. Jha, J. J. C. Busfield, *Rubber Chem. Technol.* **2013**, *86*, 218.
- [32] T. Inui, H. Koga, M. Nogi, N. Komoda, K. Suganuma, *Adv. Mater.* **2015**, *27*, 1112.
- [33] B. Ding, Z. H. Zhang, L. Gong, M. H. Xu, Z. Q. Huang, *Appl. Therm. Eng.* **2020**, *168*, 114832.
- [34] Z. Ling, Z. Zhang, G. Shi, X. Fang, L. Wang, X. Gao, Y. Fang, T. Xu, S. Wang, X. Liu, *Renew. Sustain. Energy Rev.* **2014**, *31*, 427.
- [35] Y. Fu, J. Hansson, Y. Liu, S. Chen, A. Zehri, M. K. Samani, N. Wang, Y. Ni, Y.

- Zhang, Z. Bin Zhang, Q. Wang, M. Li, H. Lu, M. Sledzinska, C. M. S. Torres, S. Volz, A. A. Balandin, X. Xu, J. Liu, *2D Mater.* **2020**, 7, 012001.
- [36] Y. Sun, S. Zhang, W. Yuan, Y. Tang, J. Li, K. Tang, *Appl. Therm. Eng.* **2019**, 149, 1370.
- [37] M. Shtein, R. Nadiv, M. Buzaglo, O. Regev, *ACS Appl. Mater. Interfaces* **2015**, 7, 23725.
- [38] J. Fu, L. Shi, D. Zhang, Q. Zhong, Y. Chen, *Polym. Eng. Sci.* **2010**, 50, 1809.
- [39] M. L. Williams, R. F. Landel, J. D. Ferry, *J. Am. Chem. Soc.* **1955**, 77, 3701.
- [40] S. Praveen, J. Bahadur, R. Yadav, S. Billa, T. Umasankar Patro, S. K. Rath, D. Ratna, M. Patri, *Appl. Acoust.* **2020**, 170, 107535.
- [41] X. Q. Zhou, D. Y. Yu, X. Y. Shao, S. Q. Zhang, S. Wang, *Compos. Struct.* **2016**, 136, 460.
- [42] B. C. Nakra, *J. Sound Vib.* **1998**, 211, 449.
- [43] S. TAKADA, K. SUZUKI, *Trans. Japan Soc. Mech. Eng. Ser. C* **2001**, 67, 2113.
- [44] P. P. Hujare, A. D. Sahasrabudhe, *Procedia Mater. Sci.* **2014**, 5, 726.
- [45] E. ADACHI, J. SATOH, *JSME Int. journal. Ser. 3, Vib. Control Eng. Eng. Ind.* **1992**, 35, 343.

Chapter IV

Tough and 3D-Printable Poly(2-methoxyethyl Acrylate)-Silica Composite Elastomer with Anti-Platelet Adhesion Property

4-1. Introduction

The biocompatibility of many polymer materials has been studied to date, and they have been put to practical use in medical devices and implant materials.^[1] Blood compatibility is an important property that determines the application of polymers as biocompatible materials; in particular, suppressing the adhesion of platelets to a material surface is necessary to avoid thrombus formation.^[2,3]

As a method for suppressing the adhesion of platelets, various studies have been conducted on the control of the microstructure of the material surface.^[4-7] Jiang et al. reported a polydimethylsiloxane film on the surface of which submicrometer ridges and nanoprotusions were formed by utilizing self-assembly, soft lithography and physical treatment processes.^[8] Cao et al. presented that materials with surfaces that contained microvalleys and were constructed by orienting long-chain branched poly(lactic acid) (b-PLA), exhibiting good mechanical properties and biocompatibility.^[9] These studies attempted to implement blood compatibility by controlling the flow of fluid near the ridges or the microvalleys that replicated the inner surface structure of blood-vessels; this approach appeared to make sense from the viewpoint of biomimicry. However, the process for forming these characteristic surface structures is complicated, and the macroscopic shape of the obtained material is limited. On the other hand, water-soluble polymers, such as poly(ethylene glycol) (PEG) and poly(methacryloyloxyethyl phosphorylcholine) (PMPC), are known to exhibit blood compatibility regardless of their

surface morphology.^[10–12] When these polymers contact blood, the local state of the water near the polymer interface affects the adhesion of proteins or cells which is important for bioinertness.^[13]

Poly(2-methoxyethyl acrylate) (PMEA), which is also blood compatible, is a next-generation bioinert polymer with low water solubility.^[14] Tanaka et al. classified the water existing near the surface of PMEA into three types (namely, nonfreezing water, intermediate water, and free water) by differential scanning calorimetry (DSC) measurements.^[15] They revealed that the intermediate water interacting with the methoxy side chain of PMEA plays an important role in blood compatibility (the intermediate water is also present in PEG and PMPC).^[16]

To date, PMEA is expected to be widely used as a blood-compatible material, but it is mainly used only as a coating agent in practical use (e.g., for artificial heart/lung fabrication). PMEA has a low glass transition temperature (T_g) and is a viscous liquid-like polymer, so its use is limited because it is not self-supporting. Suzuki et al. made a 1.2 mm thick film by casting a PMEA microsphere aqueous dispersion to obtain freestanding PMEA objects.^[17] Since PMEA microspheres could be obtained by emulsion polymerization in water, it was highlighting that this clean microsphere system offering new perspectives for application in medical devices. Tanaka et al. have shown that rubber-like hydrogen-bonded PMEA (H-PMEA) can be obtained by introducing multiple hydrogen bonding sites into the side chain of PMEA.^[18] Films of various thicknesses could be fabricated from H-PMEA by pressing the material at 60 °C and 5 MPa, or by solvent casting. Fracture stress of the aforementioned PMEA films were respectively 0.58 MPa and 1.1 MPa, which are low compared to general elastomers, and further toughening of PMEA films might be necessary for practical use. In addition, most of the reports are

limited to film objects, and there are no examples showing complex geometries. Although there are these issues to be solved, the studies on recent attempts to prepare freestanding objects from PMEA imply the great need for smart processes for medical apparatus manufacturing. Based on these studies it is predicted that PMEA, which has a structure similar to PMEO₂MA, can be reinforced by the filling of silica particles to obtain a self-supporting composite elastomer that is blood compatible.

This chapter focuses that preparing a composite elastomer mainly composed of PMEA and silica particles using additive manufacturing technology and investigate its mechanical properties and blood compatibility. Expectations for the practical application to medical devices include the ability to obtain desired 3D objects safely and quickly without using sophisticated processing techniques or expensive equipment.^[19] 3D printing of the composite elastomers herein represents a novel fabrication method to design blood-compatible soft materials into complex geometries with high resolution-features from readily available and safe substances for building medical device. These results also show new possibilities for solving potential problems with blood-compatible materials.

4-2. Experimental Section

4-2-1. Materials

2-methoxyethyl acrylate (MEA) 98% (1.01 g cm⁻³, 130.14 g mol⁻¹, Tokyo Chemical Industry) was used as a monomer without purification. Diethylene glycol diacrylate (DEGDA) (1.12 g cm⁻³, 214.22 g mol⁻¹, Tokyo Chemical Industry) was used as a crosslinking agent. Diphenyl (2,4,6-trimethylbenzoyl) phosphine oxide (TPO) (348.37 g mol⁻¹, Sigma-Aldrich) was used as a photoinitiator. The ion-exchanged water

was purified with a MILLIPORE MILLI-Q Labo system, and water with an electrical resistivity of 18.2 M Ω cm was used. A monodispersed fine silica powder with a particle size of 110 nm (2.221 g cm⁻³, Silibol®110, Fuji Chemical) was used as the filler to prepare the composite elastomers. PET film with a thickness of 50 μ m (EMBLET® S-50, UNITIKA) was used as a control for the platelet adhesion test.

4-2-2. Analytical Techniques

Thermogravimetric analysis (TGA) was performed using a Shimadzu DTG-60 with an aluminum pan under nitrogen gas conditions. A TGA sample from 10–15 mg was placed in the pan, and an aluminum lid was placed on it. The empty pan with the lid was used as the reference. The sample was increased up to 500 °C from 20 °C (20 °C min⁻¹) and then held for 1 h. The density measurements were performed with a Micromeritics Instrument Corporation AccuPyc 1330 pycnometer (Helium gas, 25 °C). The gel permeation chromatography (GPC) measurement was performed with a Shodex DS-4/UV-41/RI-101 connected with three GPC columns (Shodex KF-403, KF-404, and KF-405). THF was used as an eluent at a flow rate of 1.0 mL min⁻¹. The calibration of the molecular weight was achieved by using polystyrene standards (TSK standard polystyrene, Tosoh)

4-2-3. 3D printing

A suspension of MEA and DEGDA (200:1 molar ratio) containing 27 vol% of the silica particles was sonicated (1500 J cm⁻³) using an ultrasonic homogenizer (UP200St, Hielscher Ultrasonics). Subsequently, this suspension to which TPO (1.0 mol%) was added was used as the monomer suspension for 3D printing. By using an

MSLA 3D printer (iSUN3D, Shenzhen Esun Industrial), 3D printing of the composite elastomer was performed (405 nm, exposure time 7 s, 100 $\mu\text{m}/\text{Layer}$).

4-2-4. Cross-section observations.

To prepare cross-section samples for observation, the composite elastomers underwent an ion polishing treatment using a Gatan Model 693 Precision Ion Polishing System ($-160\text{ }^{\circ}\text{C}$, 4 keV, 6 h). The cross-section samples were sputter-coated with platinum and observed by using field emission scanning electron microscopy (FE-SEM) (SU8020, Hitachi High-Technologies).

4-2-5. Mechanical properties.

The uniaxial tensile tests were carried out using a Shimadzu EZ-Test (50 mm min^{-1}). The ISO37-4 dumbbell-type test pieces used for the test were prepared by punching the 1 mm thick composite elastomer sheet using a Super Dumbbell Cutter (SDMP-1000-D, DUMBELL).

4-2-6. Human Platelet Adhesion Test.

Human whole blood was added sodium citrate (3.2% aqueous solution) for use in this test. The platelet-rich plasma (PRP) was collected by centrifuging (200 g, 5 min) the blood suspension with a high-speed refrigerated centrifuge, and the platelet-poor plasma (PPP) was collected after further centrifugation (1500 g, 10 min). The number of platelets in the PRP and PPP was counted with an optical microscope, and the platelet suspension was prepared by adding PPP to the PRP so that the platelet density was $1.75 \times 10^7\text{ cells mL}^{-1}$. The PET film and composite elastomer sheets were cut into a square of 8 mm, and the

platelet suspension (200 μL) was placed on each sheet and incubated (37 $^{\circ}\text{C}$, 1 h). Each sheet was washed twice with phosphate buffered saline (PBS) and fixed with 1.0% glutaraldehyde in PBS (37 $^{\circ}\text{C}$, 2 h). These sheets were washed sequentially with PBS, a solution of PBS:water = 1:1 and water. After drying, the sheets were sputter coated with osmium tetroxide, and the number of platelets adhering to the surface was counted using FE-SEM (JSM-7500FA, JEOL). The platelets are classified into three types according to the number of pseudopodia: 0; Type 1, 1~2; Type 2, and more than 2; Type 3. The test was performed three times, and the average numbers of platelets that adhered to the surface in each of the five fields of view were calculated.

The ethical board of Nagoya University, Clinical Research Committee, approved the use of human biological samples (healthy human whole blood) (approval #2017-0534).

4-3. Results and Discussion

4-3-1. Preparation of the Composite Elastomer

In this study, various amounts of powdered silica particles were mixed in solutions that contained a mixture of MEA and DEGDA, a cross-linking agent, at a ratio of 200:1 (**Figure 4-1a**). Suspensions containing 0, 9, 18, 27 and 36 vol% silica particles with an average diameter of 110 nm were prepared. The suspension was sonicated (1500 J cm^{-3}) using an ultrasonic homogenizer, and TPO (0.1 mol%) was added. Then, the suspension was poured into a mold with a 1 mm thick silicon rubber spacer sandwiched between two glass plates and irradiated with ultraviolet light for photopolymerization (10 mW cm^{-2} , 120 seconds) (**Figure 4-1b**). The obtained PMEAs-silica composite elastomers were colorless, transparent and elastic (**Figure 4-1c**). These were named PMEAs-C, PMEAs-C10, PMEAs-C20, PMEAs-C30 and PMEAs-C40 based on the silica

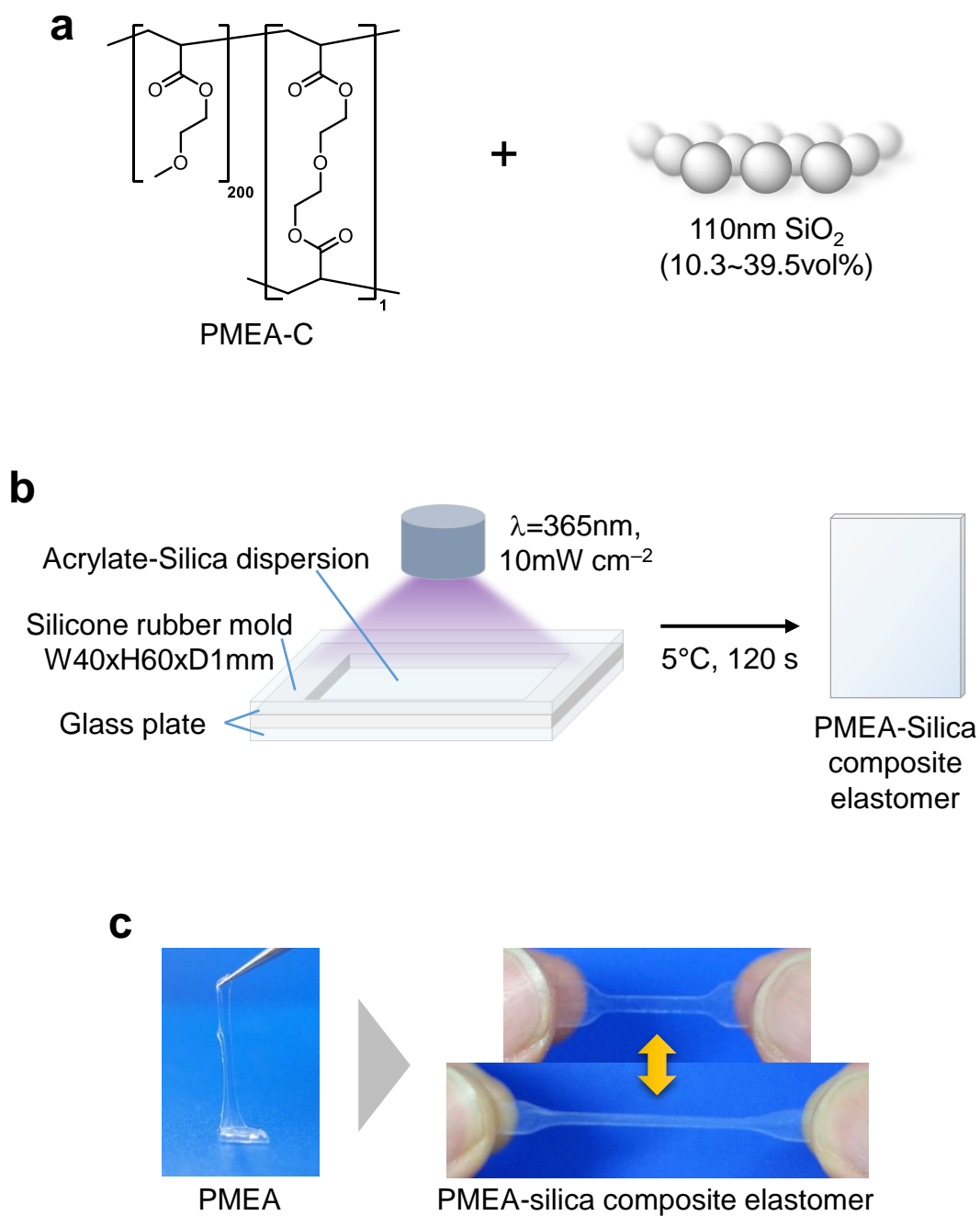


Figure 4-1. (a) Schematic of the material composition. (b) Preparation procedure for the composite elastomer. (c) Image showing the extensibility of the dumbbell-shaped composite elastomer.

particle content. The TGA results of the composite elastomers are shown in **Figure 4-2a**. As the weight loss of the PMEA and each composite elastomer started at approximately 350 °C, the silica filling had no effect on the thermal stability of the polymer. The volume fraction (ϕ) of the silica particles in the composite elastomer was calculated by eq 1:

$$\phi = \frac{(TG - 0.4) \times ED}{97.7 \times 2.221} \times 100 \quad (1)$$

The residue of the composite elastomer (*TG*: 17.8, 32.6, 45.4, and 54.6 wt%), the residue of PMEA (0.4 wt%), the residue of the silica particles (97.7 wt%), the density of silica particles (2.221 g cm⁻³) and the density of the elastomers (*ED*: 1.183, 1.284, 1.387, 1.489, and 1.582 g cm⁻³) were used. The calculated values of ϕ for the PMEA-C10, PMEA-C20, PMEA-C30 and PMEA-C40 were 10.3, 20.6, 30.9 and 39.5 vol%, respectively (**Table 4-1**). The density of the composite elastomers as measured by a gas pycnometer increased linearly with ϕ , indicating that the matrix polymers did not undergo a significant densification upon increasing the organic-inorganic interface (**Figure 4-2b**). The volume shrinkage of the PMEA and the matrix polymer in the composite elastomer determined from these results was approximately 14%.

4-3-2. 3D Printing of the Composite Elastomer

We carried out 3D printing of the composite elastomer by using commercial stereolithography (SLA) technology. In recent years, SLA have become increasingly popular, which are small and relatively inexpensive for general consumers. The potential of the composite elastomer for practical use is supported by the general use of this apparatus for fabricating objects with a variety of complex 3D geometries. Here, the suspension of MEA containing silica particles (27 vol%) was used to perform SLA 3D printing using a MSLA 3D printer (100 µm/layer). As shown in **Figure 4-3a**, it was

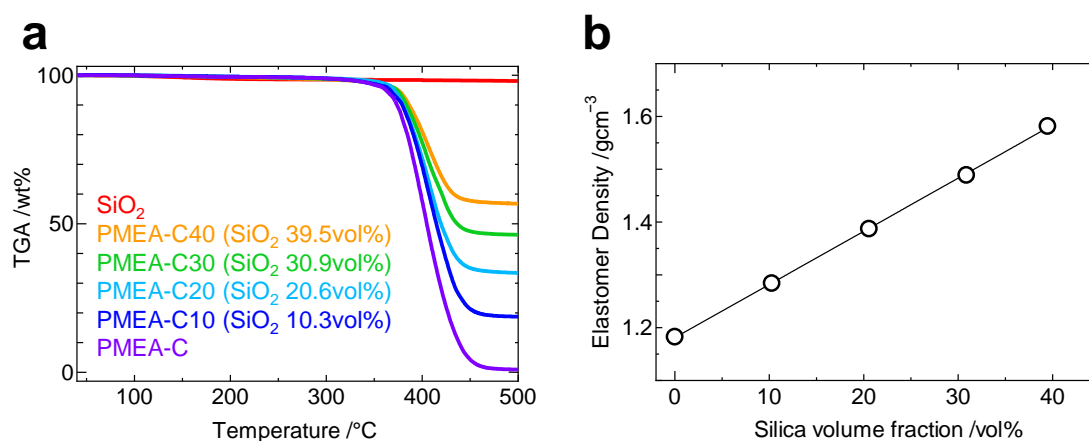


Figure 4-2. (a) TGA chart of silica particles and each composite elastomer. PMEAC, PMEAC10, PMEAC20, PMEAC30, and PMEAC40 represent composite elastomers containing 0, 10.3, 20.6, 30.9, and 39.5 vol % silica particles, respectively. (b) Dependence of the density of the composite elastomers on the amount of silica particles.

Table 4-1. Silica volume fraction of the composite elastomer.

| Composite Elastomer | ϕ_i [wt%] / [vol%] | TG [wt%] | ED [g cm ⁻³] | ϕ [vol%] |
|---------------------|----------------------------|-------------|-----------------------------|------------------|
| PMEA-C0 | 0.0 / 0.0 | 0.4 | 1.183 | 0.0 |
| PMEA-C10 | 17.6 / 9.0 | 17.8 | 1.284 | 10.3 |
| PMEA-C20 | 32.1 / 18.0 | 32.6 | 1.387 | 20.6 |
| PMEA-C30 | 44.6 / 27.0 | 45.4 | 1.489 | 30.9 |
| PMEA-C40 | 54.8 / 36.0 | 54.6 | 1.582 | 39.5 |

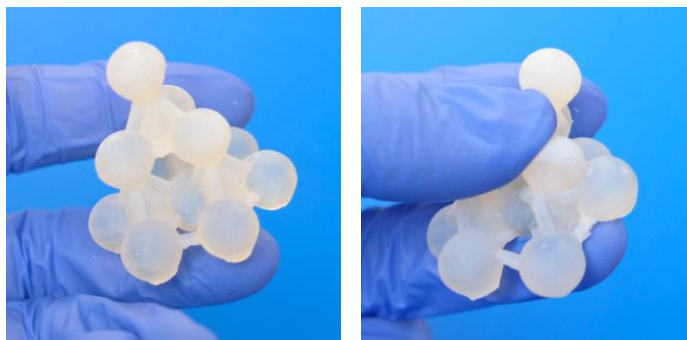
ϕ_i : SiO₂ fraction in the monomer suspension, TG: TGA residu, ED: Density of the composite elastomer, ϕ : SiO₂ fraction in the composite elastomer

possible to form a flexible solid object composed of a sphere and a tetrahedron with high precision. In additive manufacturing, each layer has a submillimeter difference, while the resolution is approximately 50 μm . Therefore, the surface is not smooth, and the object has a whitish appearance. To show the possibility of application to artificial blood vessels, tubes with diameters of less than 8 mm were fabricated (**Figure 4-3b**). Currently, popular artificial blood vessels are mainly made of PET or fluoropolymers, but they are limited to larger diameter products because occlusion by thrombus is inevitable at diameters less than 6 mm. If the composite elastomer can be used to produce thinner artificial blood vessels than the previous elastomer, then it should have useful medical applications.

4-3-3. Array of the Silica Particle in Composite Elastomers

To confirm the array of silica particles fixed in the composite elastomers, the cross sections of each composite elastomer were observed by scanning electron microscopy (SEM). The SEM images of the PMEA-C10 and PMEA-C20 show a halo pattern in the fast Fourier transform (FFT) image; hence, the particles in these samples had an isotropic alignment with short-range order (**Figure 4-4a and b**). In the section of PMEA-C30, multiple peaks can be observed in the FFT image, and it can be seen that the silica particles were aligned like in a colloidal crystal (**Figure 4-4c**). Furthermore, in PMEA-C40, where the volume fraction of silica increased to 39.5 vol%, the halo pattern was observed again in the FFT image, and the particles became isotropically oriented again (**Figure 4-4d**). As the filler amount increased, the particle arrays in the composite elastomers changed sequentially to having short-range order and forming colloidal crystals and colloidal amorphous structures. Megen et al. observed suspensions of polymethylmetacrylate (PMMA) particles (305 nm) modified with long alkyl chains and

a



b



Figure 4-3. 3D printing of the composite elastomer. (a) Image showing the flexibility of the 3D printed object. (b) Image showing 3D printed tubes with different diameters, which are 8, 6, 5, and 4 mm from the one next to the ballpoint pen.

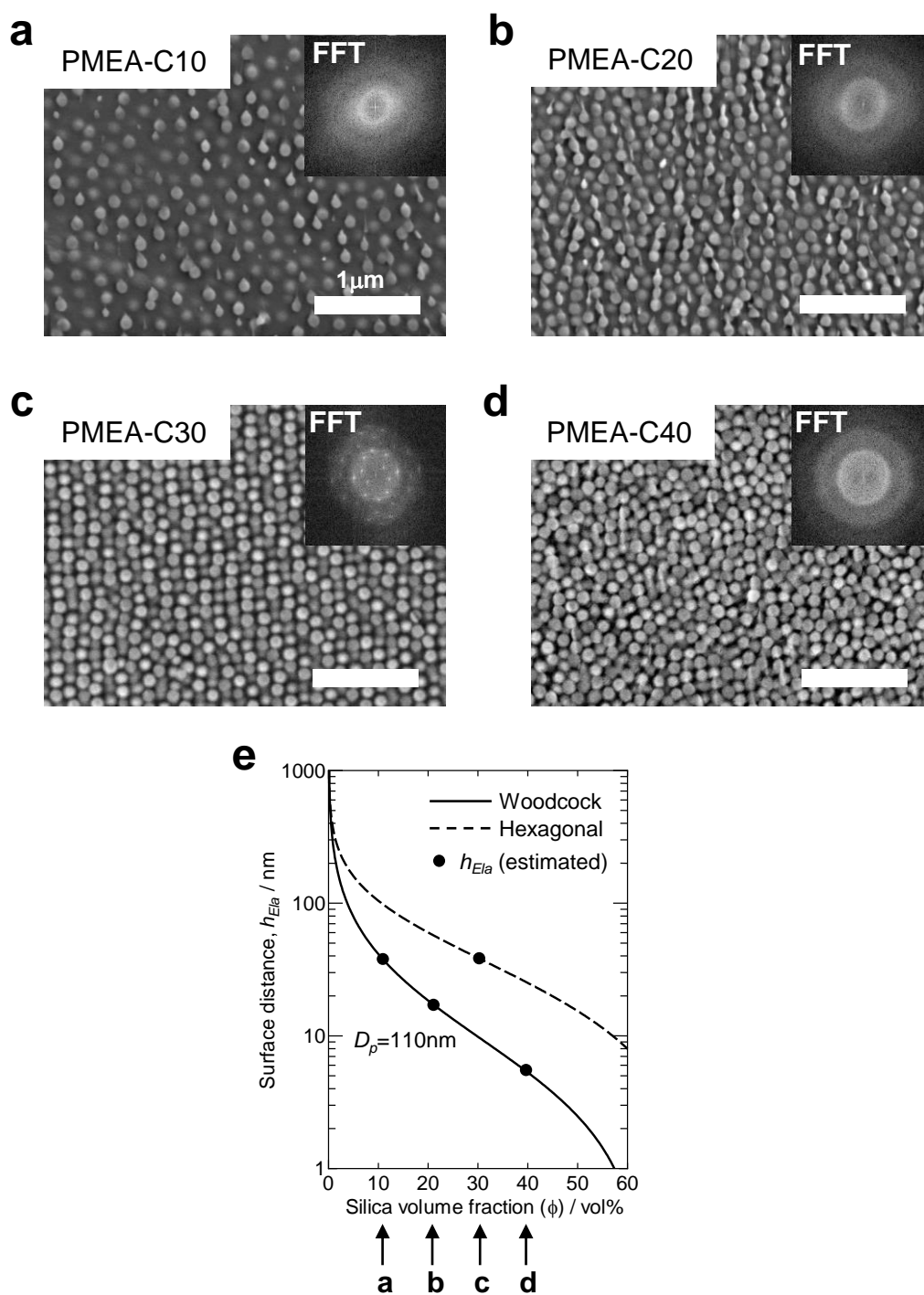


Figure 4-4. Array of the silica particle in composite elastomers. (a–d) Cross-sectional SEM images of the composite elastomers with different amounts of silica particles. The inset shows a FFT image of the SEM image. (e) Dependence of the volume fraction of silica particles on the expected distance between the particle surfaces. The arrows at the bottom of the graph correspond to the silica volume fractions in the composite elastomers observed by SEM.

found that the crystallization of particles by local freezing began at an effective volume fraction of 49.4 vol% of the hard spheres, and the crystalline state became thermodynamically stable above 54.5 vol%.^[20] However, if the volume fraction exceeded 57 vol%, crystallization became difficult due to suppression of particle diffusion, and a metastable amorphous phase was formed. Blaaderen et al., upon direct observation of the Brownian time in colloidal suspensions of PMMA-silica core-shell particles (450 nm), reported that particle diffusion did not proceed at all times above 57 vol%, and the pair correlation function showed the presence of crystalline arrays at 60 vol%.^[21] In the Woodcock equation for a system with fine dispersed particles, the average particle surface distance h_{Ela} is obtained by a function of the particle diameter and particle concentration, as given by eq 2:^[22]

$$h_{\text{Ela}} = D_p \left\{ \sqrt{\left(\frac{1}{3\pi\phi} + \frac{5}{6} \right)} - 1 \right\} \quad (2)$$

where ϕ is the particle volume fraction and D_p is the particle diameter. The h_{Ela} when the particle array is hexagonal close packed, which is referred to as a colloidal crystal, can be calculated from eq 3:^[23]

$$h_{\text{Ela}} = D_p \left\{ \left(\frac{\pi}{3\sqrt{2}\phi} \right)^{\frac{1}{3}} - 1 \right\} \quad (3)$$

In **Figure 4-4e**, the relationship between the silica volume fraction and h_{Ela} is shown, and the curves are described according to eqs 2 and 3. Under the condition where the amorphous phase forms, the h_{Ela} calculated from the result provided by Megen (305 nm and 57 vol%) was 3.0 nm according to eq 2. The h_{Ela} for PMEA-C40 with amorphous phase was 5.5 nm, which is in the same range of Megen's results. The particle morphology in the 30.9 vol% composite elastomer (PMEA-C30) was that of a colloidal crystal, and

the h_{Ela} of a colloidal crystal derived from eq 3 was 37.2 nm. Similarly, the h_{Ela} values calculated with reference to the conditions reported by Megen and Blaaderen where crystallization was confirmed were respectively 32.8 nm (305 nm and 54.5 vol%) and 32.7 nm (450 nm and 60 vol%), which are close to the value of PMEAC30. From the above results, sequential changes of the particle arrays in composite elastomers by filler amounts, which were seen in SEM images, correspond to the particle morphology in the reported colloidal suspension systems. It is considered that the particle arrangement changed from the crystalline state to the amorphous state due to the suppression of particle diffusion; this occurred because the distance between the surfaces of the silica particles in the MEA decreased. These facts are also supported by the fact that the MEA suspension containing 45 vol% silica particles became viscous and could not flow after sonication.

4-3-4. Toughening of the Composite Elastomers

The composite elastomers were toughened as a result of their increased strength and extensibility because of interfacial interactions between the PMEAC and the silica particles. **Figure 4-5a** shows the stress–strain curves obtained from uniaxial stretching of the composite elastomers prepared with various silica particle amounts. The Young's modulus and the fracture energy of PMEAC containing no silica particles were respectively 0.26 MPa and 0.4 MJ m^{-3} , which is consistent with a soft and brittle material. Surprisingly, both the stress and the strain at break were found to be improved significantly with increasing the amount of silica particles. When an elastomer, such as rubber, contains a filler, the stress is usually increased, but the extensibility is generally almost unchanged or decreased. Herein, the fracture energy of PMEAC40 was up to 15 times higher than that of PMEAC (**Figure 4-5b**). In addition, increasing the amount of

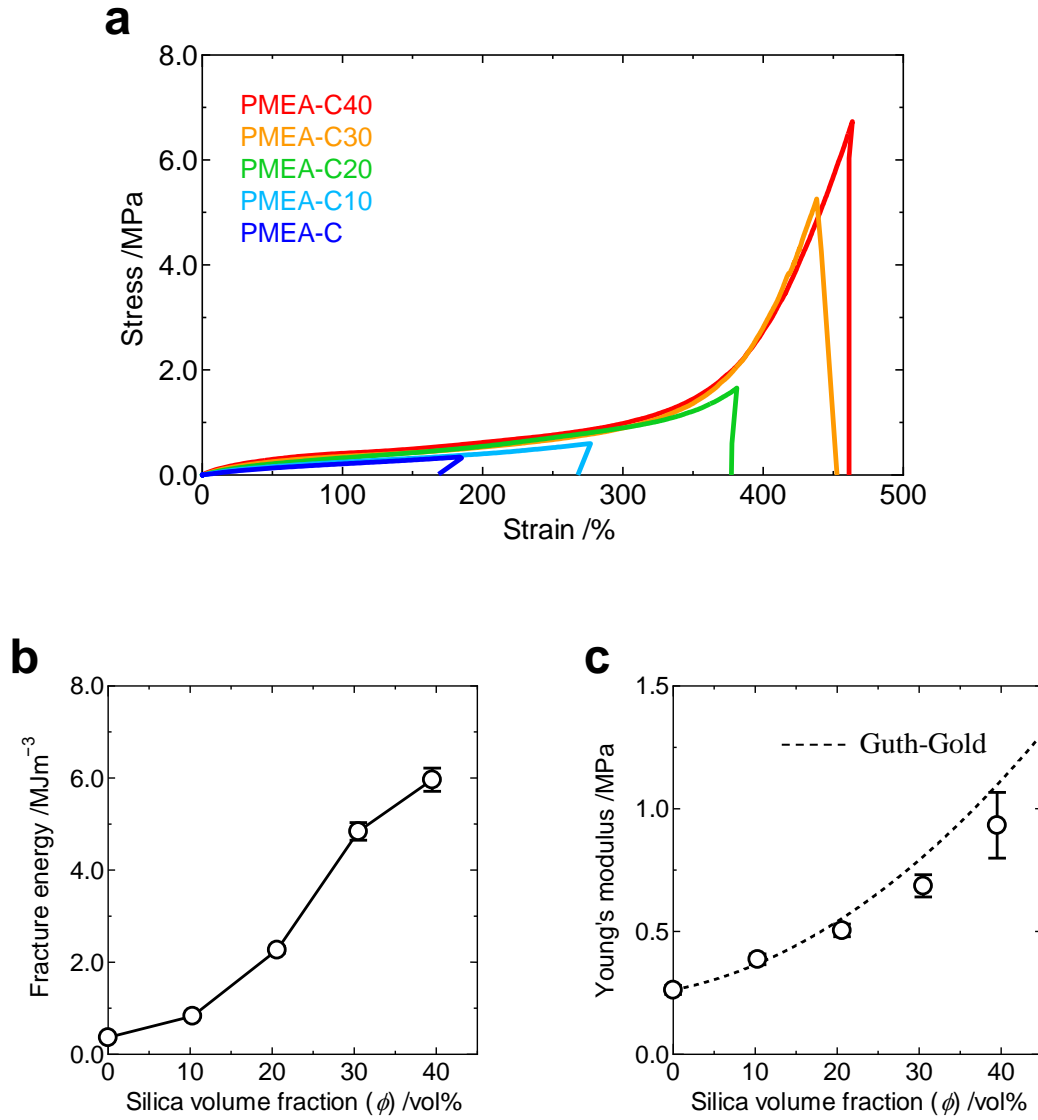


Figure 4-5. (a) Stress-strain curves of composite elastomers in which various amounts of 110 nm silica particles are dispersed. (b) Fracture energy at different silica particle amounts. (c) Young's modulus at different silica particle amounts. The dashed line shows the correlation between Young's modulus and filler amounts expected from the Guth-Gold relation.

silica particles resulted in little change of the stress-strain curve shape between 0 and 300% strain, showing excellent flexibility even when the composite elastomer reinforced. Notably, the absorbed water content of PMEAC40 was 2.2 wt% after water equilibrium, and there was only a slight change in the stress-strain curve (**Figure 4-6**). Therefore, the constant contact of the composite elastomer with blood would not significantly reduce the toughness of the composite elastomer. The mechanism of reinforcement caused by the dispersion of a filler in an elastomer is explained qualitatively by the Guth–Gold relation,^[24] which extends Einstein’s viscosity theory. Assuming that the Young’s modulus when no filler is incorporated is E_0 , the volume fraction of the filler is ϕ , and the Young’s modulus of the composite elastomer containing filler is E , the Guth–Gold relation is expressed by eq 4:

$$E = (1 + 2.5\phi + 14.1\phi^2)E_0 \quad (4)$$

The correlation between the Young's modulus of the composite elastomers and the volume fraction of the silica particle is similar to the curve obtained from the Guth-Gold relation (**Figure 4-5c**). It is well known that the Young's modulus of elastomers that contain fillers becomes higher than that of the Guth-Gold relation as the filler amount increases.^[25] Einstein’s viscosity theory, which is the basis of the Guth-Gold relation, assumes the behavior of a monodispersed system without aggregation in a dispersed medium, whereas in an actual elastomer that contains a filler, the fillers form a network of aggregates.^[26] The Young's modulus of the composite elastomer is applicable to the Guth-Gold relationship because there was almost no network of aggregated silica particles. In other words, the reason the composite elastomer was flexible at initial strains but able to withstand a high stress at high strains is that the silica particles were dispersed and there were no aggregate networks. Then, we discuss the possible reason why the toughness of

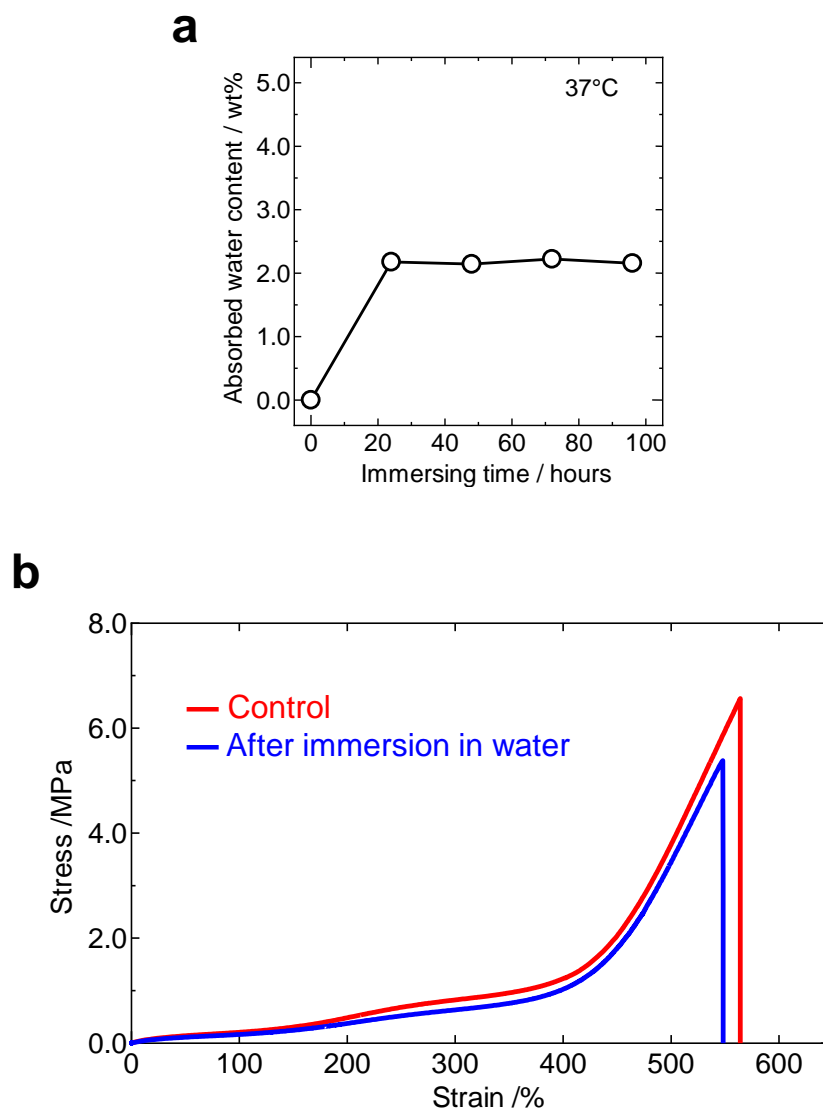


Figure 4-6. Mechanical property of the composite elastomer after water equilibrium. (a) Absorbed water content of the PMEA-C40 immersed in water at 37° C. (b) Stress-strain curve of the PMEA-C40 which immersed in water for 96 hours at 37°C.

the composite elastomer was significantly enhanced. The several results of MD simulations have mentioned that the entanglement of polymer chains is reduced in nanoparticles reinforced polymers.^[27–29] Thus, the extendibility of the composite elastomer would have increased because the entanglement, which is the point of fracture, would have decreased with increasing amounts of silica particles. In addition, the reduction of entanglements would have resulted in an increase in the number of fully extended chains under large deformations, resulting in a nonlinear elasticity. A nonlinearity of the stress-strain relation in which the stress rises significantly at large elongations is observed for soft biological tissues.^[30,31] This mechanical behavior that makes soft biological tissues less deformable as they elongate is known to help prevent catastrophe (such as a sudden large rupture). Although there are few artificial materials that exhibit such behavior, the composite elastomers in this study have the exact properties of soft biological tissues.

Next, the results of the hysteresis test of PMEA-C40 are shown in **Figure 4-7a**. In this test, the composite elastomer was deformed to a predetermined strain and then recovered until the stress reached zero. A series of cycles at each predetermined strain (20, 50, 100, 200, 300, 400 and 500% at 50 mm/min) were performed sequentially, and the results were measured up to when the specimens broke. There was no wait between each cycles. The stress-strain curve for each cycle shows a hysteresis loss, which is known as the Mullins effect.^[32] The residual strain increased linearly with increasing strain and was approximately 10% of each prescribed strain (**Figure 4-7b**). From the previous discussion of the Young's modulus and SEM images, it was predicted that there was almost no aggregate network comprising the silica particles in the composite elastomer. Hence, the presence of the hysteresis loss can be understood as the result of the dissipation of the

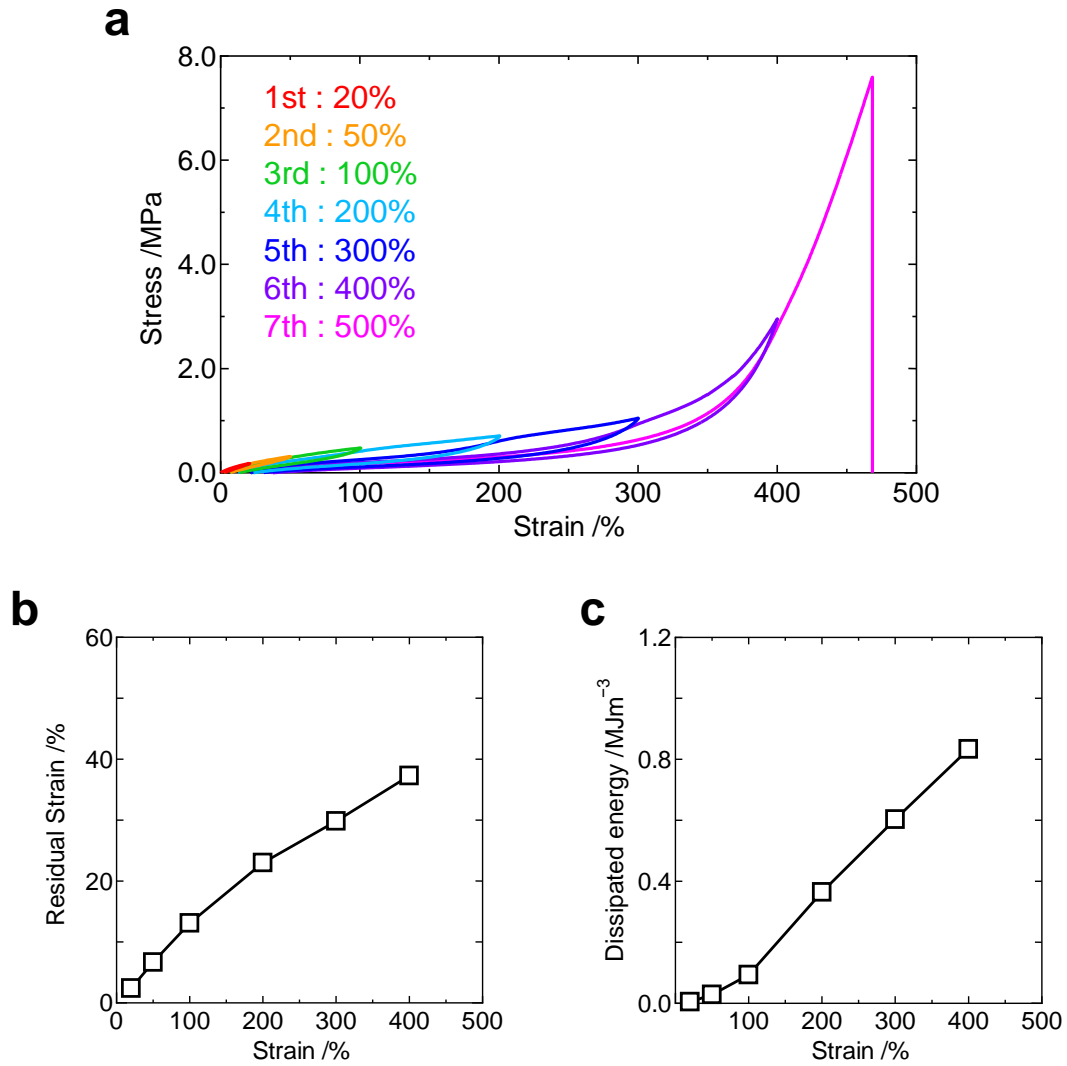


Figure 4-7. (a) Stress-strain curve of PMEA-C40 from the hysteresis measurement. (b) Dependence of the residual strain on the predetermined strain. (c) Dissipated energy at each cycle in the hysteresis measurement.

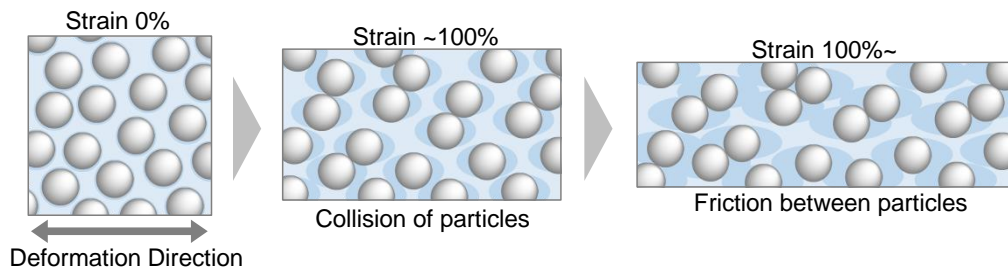


Figure 4-8. A conceptual diagram for predicting the particle morphology under the deformation of the composite elastomer.

energy of the interaction between the silica particles and the matrix polymer during deformation. The dissipated energy in each cycle increased significantly from 100% strain (**Figure 4-7c**). This rise in dissipated energy is expected to be caused by a change in the interaction of the polymer-silica interface and the energy dissipation due to the collision of silica particles and the friction between the particles under a large strain (**Figure 4-8**). In this composite elastomer, the organic-inorganic interface interaction and the interparticle interaction are at least two reinforcing effects that may be responsible for the toughening under deformation.

4-3-5. Platelet Adhesion Test with Human Blood

Platelet adhesion test is the most direct and popular evaluation method for confirming the blood compatibility of polymeric materials. Here, the platelet adhesion onto the surface of the composite elastomer was found to be suppressed, and the number of platelets that adhered to the surface was not significantly increased with increasing amounts of silica particles, although the surface was uneven. The results of the platelet adhesion test using human whole blood and the composite elastomer are shown in **Figure 4-9**. To confirm if the presence of cross-linkers affects the number of adhered platelets, the polymer of MEA with no cross-linker (PMEA) ($M_n = 200$ k and $M_w/M_n = 2.1$) was prepared with the same photopolymerization procedure as that for the composite elastomer. The solution of the polymer (20 wt% in THF) was applied on a PET film using a doctor blade, and the dried film was used as the PMEA sample. The blood compatibility of PMEA-C is slightly lower than that of PMEA but is significantly superior to that of PET. Tanaka reported that H-PMEA is slightly less blood compatible than PMEA.^[18] The PMEA led to a reduction in the intermediate water (IW) that is considered to suppress

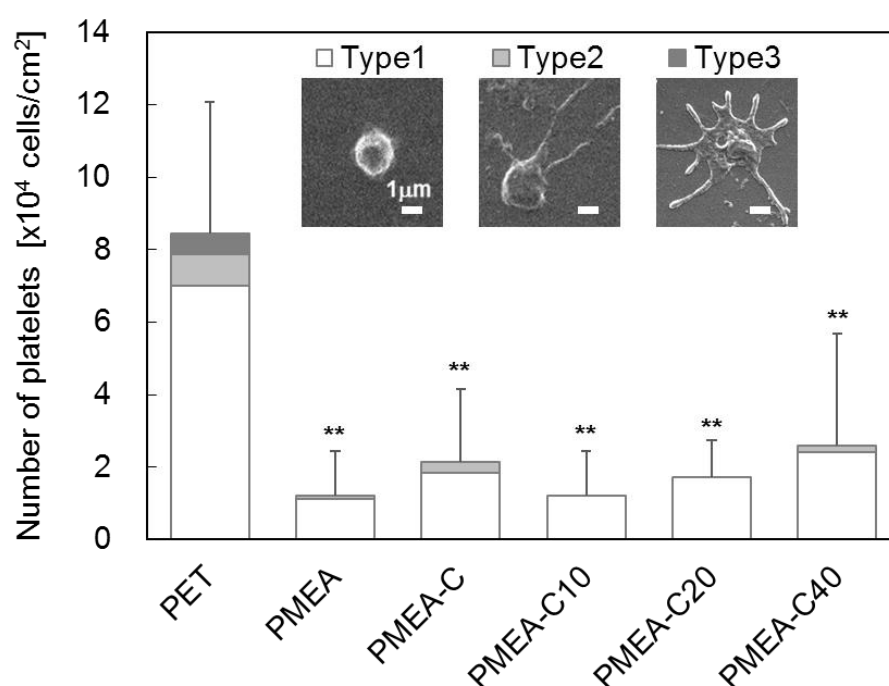


Figure 4-9. Blood compatibility of the composite elastomer. (a) Platelet adhesion test with human blood of the composite elastomer. A PET film was used as a control (the data represent mean value \pm s.d., $**P < 0.01$ vs PET). The number of platelets was classified into the following three types (shown in the inset) according to the activated state: (Type 1) spherical, (Type 2) hemispherical with several pseudopods, and (Type 3) spread-shaped with several pseudopods.

platelet adhesion, and cross-linking sites reduced both the molecular mobility and the free volume of the polymer chains. The numbers of platelets that adhered to each composite elastomer (PMEA-C10, PMEA-C20, and PMEA-C40) was almost comparable to that of PMEA-C. Multiple pseudopod-extended platelets were present in the PET but were absent in each composite elastomer (**Figure 4-10**). Remarkably, the increase in the amount of silica particles had little or no significant effect on the number of platelets. The SEM image of the composite elastomer surface shows the presence of unevenness due to the shape of the silica particles (**Figure 4-11**). The presence of a thin PMEA layer on silica particles can be confirmed from the edge image in **Figure 4-11**. The presence of a thin PMEA layer on the top surface may have inhibited the adhesion of platelets even at high silica content.

4-4. Conclusions

In summary, we demonstrated a PMEA-silica composite elastomer with nonlinear elasticity and blood compatibility that could be rapidly 3D-printed by using commercial SLA technology. The toughness of the composite elastomer improved with increasing silica particle amount, and the fracture energy of the 39.5 vol% system was 15 times higher than that of the system with no silica particles. The correlation between the Young's modulus of the composite elastomers and the Guth-Gold relation suggests that the silica particles were fixed in the polymer matrix with no network of aggregates. The mechanical behavior of the composite elastomers was similar to that of soft biological tissue, demonstrating its ability to prevent catastrophes. It has been reported that bottlebrush polymers provide materials with mechanical properties similar to those of biological tissue structures^[33,34] However, a multistep synthesis and purification step

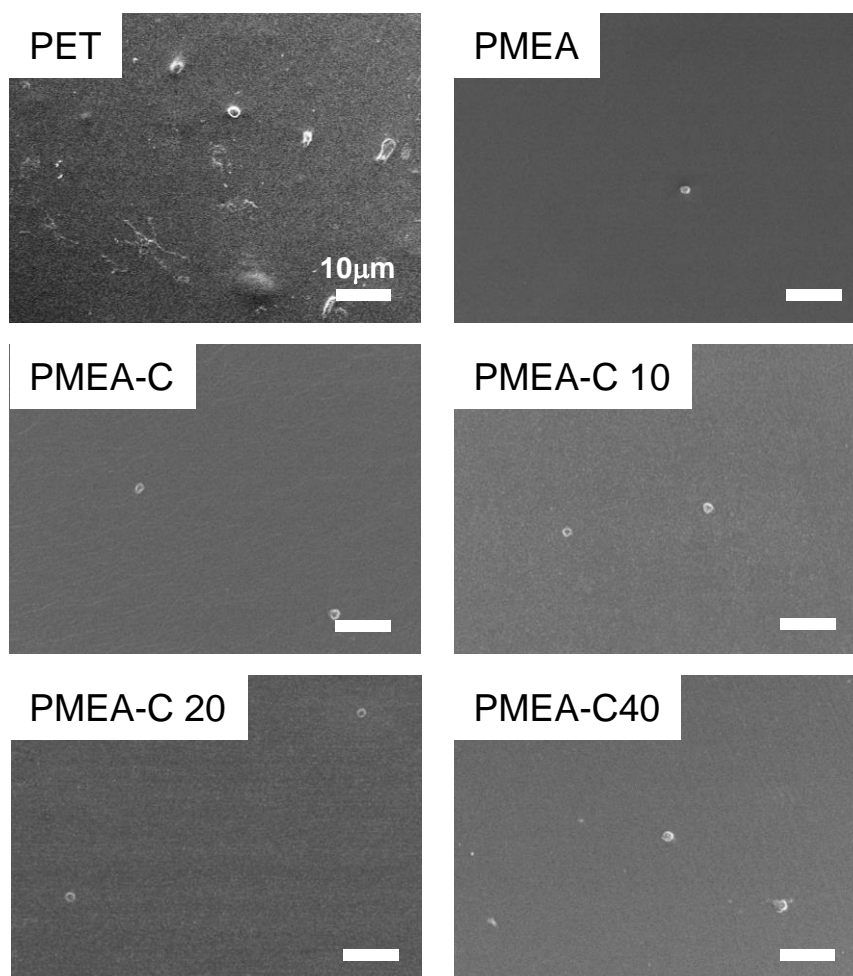


Figure 4-10. SEM images of platelets that adhered to the PET, PMEA, PMEA-C, PMEA-C10, PMEA-20 and PMCA-C40 surfaces.

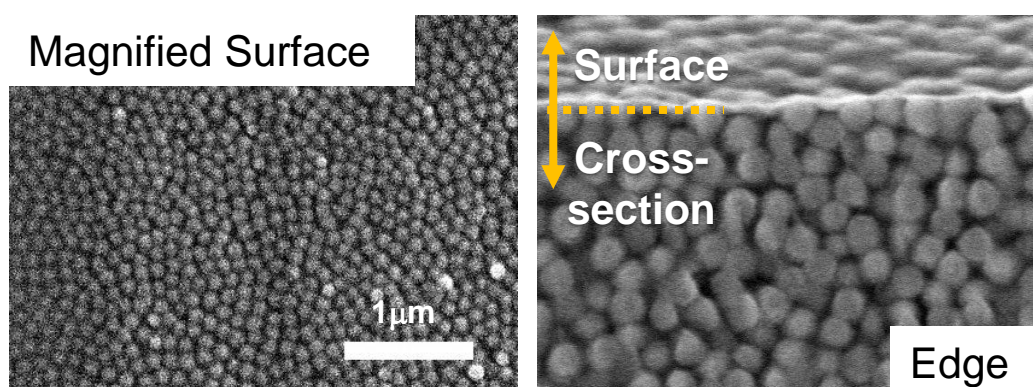


Figure 4-11. High-magnification SEM image of PMEA-C40, which focused on the surface and the edge of the cross section.

cannot be avoided to obtain the desired polymer. On the other hand, it is worth noting that the composite elastomer we developed herein can be prepared in a short time under mild conditions and from a safe material that is readily available. The platelet adhesion test showed that there was no significant increase in the number of platelets after filling PMEA with silica particles, and the composite elastomer was superior to PET in terms of the blood compatibility. We printed the composite elastomer using an MSLA 3D printer, showing its high potential for practical applications. Applying the composite elastomer to blood-compatible materials will require detailed biocompatibility assessments, the selection of safe initiators, and a reduction in residual compounds. We expect that the composite elastomer in this study could contribute to new medical devices and the advancement of medicine.

References

- [1] J. Jagur-Grodzinski, *Polym. Adv. Technol.* **2006**, *17*, 395.
- [2] X. Liu, L. Yuan, D. Li, Z. Tang, Y. Wang, G. Chen, H. Chen, J. L. Brash, *J. Mater. Chem. B* **2014**, *2*, 5718.
- [3] Q. Wei, T. Becherer, S. Angioletti-Uberti, J. Dzubiella, C. Wischke, A. T. Neffe, A. Lendlein, M. Ballauff, R. Haag, *Angew. Chemie Int. Ed.* **2014**, *53*, 8004.
- [4] L. B. Koh, I. Rodriguez, S. S. Venkatraman, *Biomaterials* **2010**, *31*, 1533.
- [5] T. Sun, H. Tan, D. Han, Q. Fu, L. Jiang, *Small* **2005**, *1*, 959.
- [6] L. Chen, M. Liu, H. Bai, P. Chen, F. Xia, D. Han, L. Jiang, *J. Am. Chem. Soc.* **2009**, *131*, 10467.

- [7] L. Chen, D. Han, L. Jiang, *Colloids Surfaces B Biointerfaces* **2011**, 85, 2.
- [8] H. Fan, P. Chen, R. Qi, J. Zhai, J. Wang, L. Chen, L. Chen, Q. Sun, Y. Song, D. Han, L. Jiang, *Small* **2009**, 5, 2144.
- [9] J. Li, Q. Chen, Q. Zhang, T. Fan, L. Gong, W. Ye, Z. Fan, L. Cao, *ACS Appl. Mater. Interfaces* **2020**, 12, 14365.
- [10] I. Banerjee, R. C. Pangule, R. S. Kane, *Adv. Mater.* **2011**, 23, 690.
- [11] Y. Xia, V. Adibnia, C. Shan, R. Huang, W. Qi, Z. He, G. Xie, M. Olszewski, G. De Crescenzo, K. Matyjaszewski, X. Banquy, R. Su, *Langmuir* **2019**, 35, 15535.
- [12] J. H. Seo, R. Matsuno, Y. Lee, T. Konno, M. Takai, K. Ishihara, *Acta Biomater.* **2011**, 7, 1477.
- [13] S. Chen, L. Li, C. Zhao, J. Zheng, *Polymer (Guildf)*. **2010**, 51, 5283.
- [14] M. Tanaka, T. Motomura, M. Kawada, T. Anzai, Yuu Kasori, T. Shiroya, K. Shimura, M. Onishi, Akira Mochizuki, *Biomaterials* **2000**, 21, 1471.
- [15] M. Tanaka, T. Hayashi, S. Morita, *Polym. J.* **2013**, 45, 701.
- [16] S. Morita, M. Tanaka, Y. Ozaki, *Langmuir* **2007**, 23, 3750.
- [17] T. Kureha, S. Hiroshige, S. Matsui, D. Suzuki, *Colloids Surfaces B Biointerfaces* **2017**, 155, 166.
- [18] K. Jankova, I. Javakhishvili, S. Kobayashi, R. Koguchi, D. Murakami, T. Sonoda, M. Tanaka, *ACS Appl. Bio Mater.* **2019**, 2, 4154.
- [19] J. Odent, T. J. Wallin, W. Pan, K. Kruemplestaedter, R. F. Shepherd, E. P. Giannelis, *Adv. Funct. Mater.* **2017**, 27, 1701807.
- [20] P. N. Pusey, W. Van Megen, *Nature* **1986**, 320, 340.
- [21] W. K. Kegel, A. van Blaaderen, *Science (80-.)*. **2000**, 287, 290.
- [22] L. V. Woodcock, in *Mol. Dyn. Relax. Phenom. Glas.*, Springer Berlin

- Heidelberg, Berlin, Heidelberg, **2008**, pp. 113–124.
- [23] H. Kamiya, Y. Otani, M. Fuji, M. Miyahara, in *Nanoparticle Technol. Handb.*, Elsevier, **2018**, pp. 109–168.
- [24] E. Guth, *J. Appl. Phys.* **1945**, *16*, 20.
- [25] J.-B. Donnet, E. Custodero, in *Sci. Technol. Rubber*, Elsevier, **2013**, pp. 383–416.
- [26] Y. Fukahori, A. A. Hon, V. Jha, J. J. C. Busfield, *Rubber Chem. Technol.* **2013**, *86*, 218.
- [27] R. A. Riggleman, G. Toepperwein, G. J. Papakonstantopoulos, J.-L. Barrat, J. J. de Pablo, *J. Chem. Phys.* **2009**, *130*, 244903.
- [28] G. J. Schneider, K. Nusser, L. Willner, P. Falus, D. Richter, *Macromolecules* **2011**, *44*, 5857.
- [29] Y. Li, M. Kröger, W. K. Liu, *Phys. Rev. Lett.* **2012**, *109*, 118001.
- [30] C. Storm, J. J. Pastore, F. C. MacKintosh, T. C. Lubensky, P. A. Janmey, *Nature* **2005**, *435*, 191.
- [31] S. S. Sheiko, A. V. Dobrynin, *Macromolecules* **2019**, *52*, 7531.
- [32] C. M. Roland, in *Sci. Technol. Rubber*, Elsevier Inc., **2013**, pp. 285–336.
- [33] C. Clair, A. Lallam, M. Rosenthal, M. Sztucki, M. Vatankhah-Varnosfaderani, A. N. Keith, Y. Cong, H. Liang, A. V. Dobrynin, S. S. Sheiko, D. A. Ivanov, *ACS Macro Lett.* **2019**, 530.
- [34] A. N. Keith, M. Vatankhah-Varnosfaderani, C. Clair, F. Fahimipour, E. Dashtimoghadam, A. Lallam, M. Sztucki, D. A. Ivanov, H. Liang, A. V. Dobrynin, S. S. Sheiko, *ACS Cent. Sci.* **2020**, *6*, 413.

Chapter V

Summary and Outlook

This theme presented the elucidation of the relation between the interface layer corresponding to the bound rubber and reinforcing effects in a system using a simple composite elastomer consisting of silica particles and acrylic polymer, eliminating the complexity of additives and filler aggregation structures that a typical filler-filled elastomer contains. Through various analyses, a part of the reinforcing mechanism has been clarified from the relationship between the mechanical properties and the nanostructure, and new functional soft materials were developed from the features derived from the characteristic morphology of this composite elastomer. The summaries of each chapter are described as follows.

In Chapter 2, AFM observation of the composite elastomer with high concentrations of spherical silica particles with a diameter of 110 nm in PMEO₂MA revealed that the fracture energy is maximum when the surface distance between the particles was approximately 30 nm, which is the distance where the interface layer of high elastic modulus with a thickness of approximately 15 nm near the silica particles just contacts each other. This result indicates a fact revealed by evaluating the composite elastomer filled with a high concentration of uniform spherical particles without an aggregated structure. Obtaining information on the interface layer in real space is expected to provide important insights for the development of composite elastomers in the future. Furthermore, vibration damping tests of the composite elastomer showed a significant improvement in the vibration damping loss factor due to silica filling, indicating its potential application as a transparent vibration damping material.

In Chapter 3, a functional soft material with a characteristic morphology was prepared by filling multilayer graphene (MLG) into a PMEO₂MA composite elastomer containing silica particles. The dispersibility of MLG in the MEO₂MA monomer was significantly improved when silica particles coexisted, and the composite elastomer obtained by polymerization of this suspension showed good thermal conductivity. The evaluation of dielectric measurements revealed that the filling of MLG and silica particles allows for an increase in the dielectric constant while suppressing the increase in the dielectric loss tangent. The loss factor measurement using unconstrained composite beams of composite elastomers showed that MLG filling improves the value of the loss factor over a wider frequency range, indicating its potential application as a damping material. These results, which showed a method to fabricate functional composite elastomers from lower-cost materials under mild, solvent-free conditions, are expected to contribute to the development of new soft materials for practical use.

In Chapter 4, a composite elastomer with greatly improved toughness was prepared by adding spherical silica particles to poly(2-methoxyethyl acrylate) (PMEA), a hydrophobic blood compatible material. This composite elastomer showed a J-shaped stress–strain curve, which is similar to the mechanical properties of biological soft tissues. The test result using platelets from human whole blood showed that the antiplatelet adhesion properties of PMEA-silica composite elastomers were comparable to those of PMEA. In addition, the success in 3D printing of the composite elastomer by using a stereolithography technology should lead to expanding the applications of PMEA, which has been limited to use as a coating. Applying the composite elastomer to blood-compatible materials will require detailed biocompatibility assessments, the selection of safe initiators, and a reduction in residual compounds. It is expected that the composite

elastomer in this study could contribute to new medical devices and the advancement of medicine.

As demonstrated in this thesis, the existence of the interface layer near silica which increases the toughness of the composite elastomer was revealed, and the potential applications of this composite elastomer as a practical soft material were suggested. Elucidation of the reinforcing mechanism of filler-filled elastomers is essential for the development of functional soft materials that sustain new lifestyles, and the application of new basic theories in various fields is eagerly awaited. In this context, the facts and functions revealed by the analysis of a simple compositional elastomer in this study are expected to contribute to the elucidation of the reinforcement mechanism of general filler composite elastomers dominated by complex factors and to the creation of new functional soft materials.

Publications

1. Fumio Asai, Takahiro Seki, Taiki Hoshino, Xiaobin Liang, Ken Nakajima, Yukikazu Takeoka, “Silica Nanoparticle Reinforced Composites as Transparent Elastomeric Damping Materials”, *ACS Appl. Nano Mater.* **2021**, 4 (4), 4140–4152.
2. Fumio Asai, Takahiro Seki, Yukikazu Takeoka, “Functional Polymethacrylate Composite Elastomer Filled with Multilayer Graphene and Silica Particles”, *Carbon Trends* **2021**, 4, 100064.
3. Fumio Asai, Takahiro Seki, Ayae Sugawara-Narutaki, Kazuhide Sato, Jérémy Odent, Olivier Coulembier, Jean-Marie Raquez, Yukikazu Takeoka, “Tough and Three-Dimensional-Printable Poly(2-Methoxyethyl Acrylate)–Silica Composite Elastomer with Antiplaetlet Adhesion Property”, *ACS Appl. Mater. Interfaces* **2020**, 12 (41), 46621–46628.

Other Related Publications

1. Kenta Watanabe, Eiji Miwa, Fumio Asai, Takahiro Seki, Kenji Urayama, Tomotaka Nakatani, So Fujinami, Taiki Hoshino, Masaki Takata, Chang Liu, Koichi Mayumi, Kohzo Ito, Yukikazu Takeoka, “Highly Transparent and Tough Filler Composite Elastomer Inspired by the Cornea” *ACS Mater. Lett.* **2020**, 2 (4), 325–330.
2. Eiji Miwa, Kenta Watanabe, Fumio Asai, Takahiro Seki, Kenji Urayama, Jérémy Odent, Jean-Marie Raquez, Yukikazu Takeoka, “Composite Elastomer Exhibiting a Stress-Dependent Color Change and High Toughness Prepared by Self-Assembly of Silica Particles in a Polymer Network”, *ACS Appl. Polym. Mater.* **2020**, 2 (9), 4078–4089.
3. Yukikazu Takeoka, Sizhe Liu, Fumio Asai, “Improvement of Mechanical Properties of Elastic Materials by Chemical Methods”, *Sci. Technol. Adv. Mater.* **2020**, 21, 817-832.

Presentations at International Conferences

1. Fumio Asai, Yukikazu Takeoka, Takahiro Seki, Tomotaka Nkatani, Taiki Hoshino, Xiaobin Liang, Ken Nakajima, “Physical properties and structure of a cornea-inspired poly-acrylate/nanosilica hybrid elastomer”, OKINAWA COLLOIDS 2019, Okinawa, Japan (2019)

Patents

1. 浅井 文雄, 関 隆広, 竹岡 敬和, “樹脂組成物および該樹脂組成物からなるエラストマー材料”, 特願2019-200134.
2. 浅井 文雄, 竹岡 敬和, 鳴瀧 彩絵, 佐藤 和秀, 関 隆広, “樹脂組成物および該樹脂組成物からなるエラストマー材料”, 特願2020-096690.
3. 浅井 文雄, 竹岡 敬和, 関 隆広, “樹脂組成物および該樹脂組成物からなるエラストマー材料”, 特願2021-026479.
4. 浅井 文雄, 竹岡 敬和, 関 隆広, “樹脂組成物および該樹脂組成物からなるエラストマー材料”, 特願2021-048814.
5. 浅井 文雄, 竹岡 敬和, 関 隆広, “樹脂組成物および該樹脂組成物からなるエラストマー材料”, 特願2021-064209.

Acknowledgements

This thesis is based on the studies under Prof. Takahiro Seki at the Department of Molecular and Macromolecular Chemistry, Graduate School of Engineering, Nagoya University. First of all, I would like to express my sincere gratitude to Prof. Takahiro Seki and Assoc. Prof. Yukikazu Takeoka for their kind guidance and encouragement throughout my doctoral course. I also deeply appreciate the laboratory staff, Prof. Shusaku Nagano (now at Rikkyo University, Faculty of Science and Engineering) and Assist. Prof. Mitsuo Hara, for their advice and assistance with my research and experimental works.

This thesis was also supported by leading researcher's helps in each field. Many thanks to Prof. Ken Nakajima, Assist. Prof. Xiaobin Liang (Department of Chemical Science and Engineering, Tokyo Institute of Technology), Dr. Taiki Hoshino (RIKEN SPring-8 Center), Prof. Ayae Sugawara-Narutaki (Department of Energy Engineering, Nagoya University), Assist. Prof. Kazuhide Sato (Respiratory Medicine, Nagoya University Graduate School of Medicine) and Assoc. Prof. J  r  my Odent (Laboratory of Polymeric and Composite Materials, University of Mons) for all the valuable discussions and productive collaborations. I could not have performed my research works without their supports.

I wish to express my special thanks to all members of the Seki laboratory for their generous supports. In particular, I would like to thank Dr. Issei Kitamura, Mr. Eiji Miwa, Mr. Yusuke Baba, Mr. Ikuya Ohashi, Mr. Tomoki Sakai, Mr. Sizhe Liu, Mr. Daiki Miyake and Ms. Mayu Yamada as my collaborators. I received various cooperation and warm encouragement in my laboratory life from Mrs. Yuko Ohiwa as administrative

assistant. I appreciate them sincerely.

I would like to express heartfelt gratitude to Dr. Masakazu Kitano, Mr. Munehiro Miyake of UNITIKA LTD. and Mr. Takao Okouchi of NIPPON ESTER CO., LTD. for their support and consideration in providing me with this opportunity.

Finally, I am grateful to my wife and my sons for their helpful support and heartfelt encouragement.

January 2022

Fumio Asai